Extracting *Cancer pagurus* stomatogastric ganglion pyloric rhythm frequency via voltage-sensitive dye imaging data using signal processing techniques

Filipa dos Santos

PhD Computer Science

October 2019

Keele University

Abstract

Voltage-sensitive dye imaging (VSDI) has been widely used in the past few decades in both vertebrates and invertebrates to study, *in vitro* and *in vivo*, the nervous systems. *Cancer pagurus* is a seawater crab whose nervous system has a ganglion, the stomatogastric ganglion (STG) that contains a relatively small number of neurons and two rhythm forming central pattern generators (CPGs). The pyloric rhythm is one such spontaneous rhythm that can be readily observed *in vitro*, which makes the STG an ideal ganglion to study using VSDI. However, a major impediment to the effectiveness of VSDI is that the optically recorded data is often noisy with poor signal-to-noise ratios (SNR), rendering it difficult to study and analyse.

This thesis describes the first-ever development of computational signal processing procedures that sought to extract the pyloric rhythm directly from the VSDI data, thus facilitating an accurate identification of the individual neurons in the pyloric circuit. Specifically, a multiresolution procedure based on the sequential Singular Spectrum Analysis (s-SSA) was first constructed to separate the pyloric rhythm from the noisy VSDI recording, enabling potential pyloric neurons to be detected by the presence of the pyloric frequency in the computed spectra of the respective cells. To facilitate identifying the pyloric neurons, the duty cycle (DC) was devised as a biometric, and the corresponding ratio of harmonics (RH) was determined in terms of the harmonic content of the spectrum computed for each cell/neuron as described above. Here, the instantaneous phase of the detected pyloric rhythm was also estimated, allowing it to be compared and aligned with the three distinctive pyloric phases (PD-, LP- and PY-timed) readily measured on the lateral ventricular nerve (lvn). As proof of concepts, finally, an automated method to determine the pyloric frequency directly from VSDI data was developed, over a range of SNRs, demonstrating the possibility to identify prospective pyloric neurons based on the estimated DCs and respective phase shifts measured against the analogue lvn recording.

Index

Acronyms

AB	Anterior burst neuron
$CaCl_2H_2O$	Calcium chloride hydrate
cm	Centimetre
CoG	Commissural ganglion
CPG	Central pattern generator
CWT	Continuous wavelet transform
dB	Decibel
DC	Duty cycle
DG	Dorsal gastric neuron
dvn	Dorsal ventricular nerve
g	Grams
Hz	Hertz
IC	Inferior cardiac neuron
ICA	Independent component analysis
Int_1	Interneuron
L	Window length
LG	Lateral gastric neuron
LP	Lateral pyloric neuron
LPG	Lateral posterior gastric neuron
lvn	Lateral ventricular nerve
MG	Medial gastric neuron
$MgCl_26H_2O$	Magnesium chloride hexahydrate
min	Minutes
mM	Millimolar
ms	Millisecond
MΩ	MegaOhm
mV	Millivolt
nA	Nanoampere
NaCl	Sodium chloride
OG	Eophageal Ganglion
PCA	Principal component analysis
PD	Pyloric dilator neuron
PSD	Power spectral density
PY	Pyloric neuron
RH	Ratio of harmonics
ROI	Region of interest
s	Second
SSA	Singular spectrum analysis
s-SSA	Sequential singular spectrum analysis
STG	Stomatogastric ganglion
stn	Stomatogastric nerve
STNS	Stomatogastric nervous system
SVD	Singular-value decomposition
VD	Ventricular dilator
K_2SO_4	Potassium sulphate

VSD	Voltage-sensitive dye
VSDI	Voltage-sensitive dye imaging
μl	Microliter
μsec	Microsecond

List of Figures

List of Tables

Acknowledgements

I firstly would like to thank Dr Gordon Rugg for helping me to make this possible, and Dr KP Lam for guiding me through the signal processing analysis and for providing the support (technical and moral) needed throughout.

Secondly, I would like to thank Professor Maria Heckl for important friendly support, particularly over the past year.

Thirdly, I would like to thank Dr Stephanie Jones and Deborah Adams for the technical support in the C.A.F.

I also would like to thank my mother, my sister Barbara and some friends that helped me emotionally especially during the final year of my PhD study. This thesis would not be possible without them.

Finally, I would like to thank Keele University for the scholarship and Professor Peter Andras for the use of his laboratory space.

1. Introduction

This thesis presents a three-part test of concept that combines computer sciences and neurosciences using signal processing techniques. It aims to develop a reliable method for neuron identification using data acquired by voltage-sensitive dye imaging (VSDI). The biological sample used in this research work was the stomatogastric nervous system (STNS); specifically, the stomatogastric ganglion (STG) of *Cancer pagurus*, which was stained, imaged and analysed.

Understanding the genesis of rhythmic motor patterns produced by a central pattern generator (CPG) has long been a fundamental goal in neuroscience. Practical applications include, for example, mechanisms governing the continuous rhythms such as respiration or cardiac contractions, or those rhythms produced intermittently such as locomotion, swimming or chewing (Katz, 1995; Marder and Calabrese, 1996; Ramirez, Tryba and Peña, 2004; Grillner, 2006; Selverston, 2010; 2018; Minassian *et al.*, 2017; Del Negro, Funk and Feldman, 2018).

Traditionally, intracellular recordings[1] capture in detail activities of individual neurons or a small population/network, allowing them to be studied either online or at a later stage. However, due to physical limitations in terms of space and execution time, intracellular recordings are not suitable for studying large-scale networks. This thesis concerns the development of reliable methods for neuron identification by means of optical imaging using voltage-sensitive dyes (VSDs), which overcome the physical space (and time) constraints by allowing the simultaneous recording of all neurons in the field of view in a relatively simple dye bath setting. The importance of a practical realisation of such methods of neuron identification is that it enables studies of the pyloric network, at the level of single cells and neuronal assembly (Fishell and Heintz, 2013; Zhu *et al.*, 2017). The use of this imaging technology for identification will be further described in later chapters, where advanced

[1] Intracellular recordings is a method used to measure voltage or current of the cell membrane. Normally it uses an electrode inserted in the cell and another outside the cell.

computational signal processing procedures developed to determine the triphasic pyloric rhythm associated with the individual neurons will be described. The current chapter provides an overview of the methodology to achieve this.

Technologically, VSDI is a technique that uses VSDs, and works as a fast-response molecular probe that operates by means of a change in their spectral/fluorescence properties, in responding to a change in the surrounding electric field (as measured voltage) at the cell membrane where the dye molecules are attached. High-speed cameras optically capture the resulting changes in fluorescence. As mentioned above, a principal advantage of VSDI is that its use has overcome space limitations when compared to the conventional method of intracellular recordings. The use of VSDI will be discussed further in section 2.1.5.

1.1. Background

Arthropods have been used to study the neural network for over 60 years (Wiersma, 1953; Maynard, 1955; Kao, 1960); they played an essential role in neural network studies for a number of reasons. In particular, they are relatively easy to maintain for *in vitro* studies; namely, (i) have anatomically distributed nervous systems (as opposed to the highly centralized systems found in vertebrates); (ii) possess large neurons that are easily recorded from and contain structures that are repeatedly identifiable in different animals of the same or analogous species (Hooper and DiCaprio, 2004; Marder and Bucher, 2007), and (iii) currently do not require ethical approval to experiment on them *in vivo*. Additionally, the fresh/live crabs were acquired from a food source, so its parts were consumed after the experiments.

Understanding the basic neuronal functions of the arthropod STNS is an important step for the understanding of more complex systems, including structure, functionality and organisation of the human brain or the central nervous system. The study of invertebrates is beneficial for this understanding as they are less complex and neurons show similar levels of complexity in intrinsic

properties and synaptic plasticity as vertebrates (Harris-Warrick and Marder, 1991; Marder and Calabrese, 1996; Nusbaum and Beenhakker, 2002).

In particular, vertebrates regulate their internal organs primarily by the function of the autonomic nervous system (central and peripheral nerves), such as blood vessels, heart, smooth muscle, viscera and glands, while in crustaceans the nervous system controls the organs independently by different nerves. However, some neural structures in the subphylum Crustacea can be compared to the autonomic nervous system in vertebrates (Shuranova *et al.*, 2006). For example, the cardiac ganglion in decapod crustaceans is analogous to the AV node in vertebrate's heart, whilst the cardiac and respiratory functions in crustaceans are coordinated by neuromodulators and/or the endocrine systems like in vertebrates. More relevantly, the STG (located outside the gut) of decapod crustaceans controls the foregut (striated) muscles which is analogous to the enteric nervous system and the muscles in the digestive system in vertebrates.

In other studies, Belanger (2005) showed that the motor control (striated muscles in locomotion) in arthropods and vertebrates shares a high degree of similarity. Specifically, despite the relatively simple system in arthropods, due to its physical decentralisation, their motor control networks support a similar degree of complexity in functionality to that of the vertebrates, (thus) making arthropods a good choice/model for studying sensory processing, motor coordination and even higher brain functions in vertebrates. Likewise, Hartenstein (2006) presented a review in the neuroendocrine system of invertebrates with great emphasis on the degree of similarity between flies (*Drosophila*) and vertebrates.

Over the last few decades, the emergence of many powerful functional imaging techniques that cover broad spatial and temporal scales has enabled neuroscientists to explore connections and functions of neural circuits in/across different species in ways that were not previously feasible. Recently, Ahrens and Engert (2015) have shown the importance and achievements made by imaging small brains in order to understand and/or compare with larger brains. The study emphasized the benefits of small-scale imaging of complete networks, from which valuable insight were developed to

deepen our understanding of larger brains, with knowledge that is limited only by the behavioural functions not exhibited in these smaller networks.

In biology, neuromodulation is a physiological process by which a given neuron uses one or more chemicals, for example, dopamine, serotonin, acetylcholine or histamine, to regulate another neuron or a population of neurons. Neuromodulators are neurotransmitters which are dispersed through the neuronal tissue. They are known to have modulatory effects on neurons, thus affecting their behaviour such as spiking, its firing rate (Harris-Warrick *et al.*, 1995; Scheler and Fellous, 2001; Bucher, Thirumalai and Marder, 2003; Grashow, Brookings and Marder, 2009; Gutierrez, O'Leary and Marder, 2013; Martinez, Matveev and Nadim, 2016) and spike form/shape alternation during working memory[2] (Brunel, Sup and Wang, 2001; Procyk and Goldman-Rakic, 2006). In medicine, neuromodulation is known as the therapy that targets specific neurons to treat or improve conditions, by electrical stimulation or delivering chemical agents.

Functionally, using small systems to study neuromodulation is a significant step to recognise neuronal functional 'errors', which are essential to slow, stop or reverse neural malfunction in large-scale systems such as chronic pain, epilepsy, Parkinson or urinary incontinence (Nusbaum and Beenhakker, 2002; Williamson and Chrachri, 2004; Kristan, Calabrese and Friesen, 2005; Nogueira and Caputi, 2013). Indeed, the neuromodulation device industry worldwide is expected to grow from $8.4 billion in 2018 to $13.3 billion in 2022, according to Neurotech Reports (Neurotech, 2018). The Annual Report from Boston Scientific Corporation (Scientific, 2018) has reported an increase of 14.2% in neuromodulation products sales from 2016 to 2017, which was translated to an increase of US$79 million to a total sales of US$635million in 2017. Other projects have also been investing in the research of neuromodulation, neuroscience and neuroimaging such as the Blue Brain Project (Switzerland), Human Connectome Project (United States of America), the Human Brain Project

[2] Working memory is the process of retaining information and remembering it using the relevant information for the task in hand.

(European Commission), Brain/MINDS project (Japan), Brain Science Centre (Shanghai, China), among others.

1.2. The Animal Model – *Cancer pagurus*

As mentioned earlier this thesis used the nervous system of *C. pagurus*, a decapod crustacean, a seawater crab found in the North Atlantic Ocean, North Sea and in the Mediterranean Sea, seen in Figure 1, commonly known as edible or brown crab (Fisheries and Aquaculture Department, 2018; Ocean Biogeographic Information System, 2018). Its carapace length typically does not exceed 20cm, and the width 30cm, typically no more than 24cm. This crab lives on the sea bottom in depths between 2 to 55m, but most commonly up to 25-30m depth. Animal size and sea depth are related: the bigger the crab, the deeper it can live (Heraghty, 2013; BIOTIC - Biological Traits Information Catalogue, 2018).

Figure 1 – Schematic distribution map of Cancer pagurus. Adapted from Fisheries and Aquaculture Department (2018).

Decapod crustaceans (order Decapoda – Latreille, 1802) are all the animals with ten legs (ten-footed) in the family groups of the class Malacostraca, which include crayfish, crabs, lobsters, prawns and shrimp.

One of the main reasons for choosing the brown crab for this research is because the stomatogastric ganglion (STG) presents two stable and fully functional CPGs that generate the gastric mill and pyloric rhythm within a small network of 25-32 neurons. More importantly, it is relatively easy to obtain and maintain in the laboratory to facilitate studies *in vitro*. In particular, the pyloric rhythm is known to remain spontaneous *in vitro* for up to two weeks (Marder and Bucher, 2007). Furthermore, the STG presents a flat configuration, allowing its study with standard 2-D imaging methods. The above makes the brown crab a preferred model in comparison to other animal networks.

In passing, it should be noted that, throughout this work, the STNS and connectivity properties of *Cancer pagurus* occasionally used literature from *Cancer borealis,* since this relies on their degree of similarity (Heinzel, Weimann and Marder, 1993; Stein, Eberle and Hedrich, 2005; Stein *et al.*, 2006; Smarandache and Stein, 2007).

1.3. Aims and Objectives

In recent years, optical imaging methods using molecular probes such as voltage sensitive dyes (VSD), which convert neuronal physiological signals directly into optically detectable signals, has overcome many limitations of classical microelectrode-based electrophysiology. In particular, they facilitate parallel measurements of electrical activities of individual neurons and across populations of interconnected neurons in a variety of preparations *in vivo* and *in vitro* (Chemla and Chavane, 2010; Tsytsarev *et al.*, 2014). However, despite such remarkable capability to simultaneously capture in high spatial (20—50μm) and temporal resolution (sub-millisecond) the activity of many neurons, optical recording of neural activity with fast-response voltage sensitive dyes has, to date, been

largely under-utilised, being used mostly as a supplementary technique for studying the STG *in vitro*. A major impediment lies in the fact that the raw VSD signal obtained from the dye-stained sample, especially if bath-applied, is highly complex, with a noisy combination of several different components originating from physiological, mechanical, electrical, or optical/interference sources. Indeed, this explains why the indirect method of calcium imaging[3] is used more frequently than VSD to monitor neuronal electrical activity, as a practical compromise between what is needed and what is feasible (Peterka, Takahashi and Yuste, 2011). Here, the lack of computationally tractable signal processing tools/procedures that will (i) facilitate analysing/interpreting the inherent complexity of the recorded signal and, importantly, (ii) bridging the gap in knowledge and the (optimal) use of this imaging technology is apparent.

The principal aim of the research/work presented in this thesis is to fill the current void that exists in our understanding, or the lack of it, of the inherently complex and typically noisy VSDI signals recorded from the bath dyed preparations in general and, in particular, the STG sample (Hill, Bruno and Frost, 2014). More specifically, the goal is to develop computational signal processing procedures that can improve in knowledge and understanding of the VSDI signal, and thus facilitate a better understanding of the dynamic properties (as well as functions) of the individual neurons and their connections in the context of the pyloric circuit. In neuromodulation, for example, knowledge of the functions of all network components is vital to the understanding of circuit dynamics as the dynamic response of a neuron to a neuromodulator can have an impact on the circuit response to that modulator (Hartline, 1979; Hooper and Marder, 1987; Harris-Warrick *et al.*, 1992).

To achieve the above, a set of objectives are defined as follows:

- To develop an experimental protocol for the *in vitro* preparation of the STG in a dye bath setting, with the associated data collection procedure.

[3] Calcium imaging is a technique that uses dyes which bound to the calcium ions (Ca^{2+}) in the cell. Changes in calcium concentrations can be measured by fluorescent microscopy.

- The pyloric rhythm, if present, of the individually identified cells, needs to be extracted from the optical recordings. The neuropil, identifiable from each recording, has to be used as a reference of the pyloric rhythm whose fundamental frequency should be verified by the associated electrophysiological recordings obtained on the lateral ventricular nerve (lvn).
- The characteristics of the extracted pyloric rhythm need to be studied in terms of the harmonic content of the rhythm and, relevantly, their energy distributions, to facilitate performance evaluation of the extraction procedure as well as an estimation of the signal-to-noise ratio (SNR) of the VSDI data.
- The neuronal 'signatures' have to be elicited from the optical/VSDI recording, to facilitate their effective comparison with and mapping on the corresponding extracellular recording over the lvn. Here, the time lag between the two recordings has to be estimated accurately.
- An automated procedure to determine the pyloric frequency reliably from the VSDI data has to be constructed, with the performance analysed over a range of achievable SNRs.

1.4. Contributions

The main contributions of the research project presented in this thesis are:

1) Development of a multiresolution signal processing procedure to reliably extract pyloric rhythm from the optical recordings by means of a multiresolution algorithm based on the sequential Singular Spectrum Analysis (s-SSA) techniques. To facilitate determining the pyloric rhythm, the lvn was used to provide an initial estimation of the pyloric frequency to help elicit key operating parameters of the SSA. Here, the s-SSA was first applied to the neuropil from which the pyloric rhythm was extracted as a reference.
2) The first-ever successful identification of the pyloric neurons (PY) from the optical recording/data of the STG sample, by integrating such data with the

extracellular/electrophysiological recordings on the lvn. This entailed three main tasks. First, the demonstration of a computationally well-defined and biologically meaningful metric based on the notion of the duty cycle (DC). Second, the development of advanced signal processing procedures to deconstruct/reconstruct the triphasic pattern of the pyloric rhythm captured on the lvn. Third, the implementation of a phase tracking procedure based on Hilbert Transform, which enabled the instantaneous phases of the pyloric rhythm, if present, to be extracted from the optical recording, allowing them to be accurately mapped on the individual phases of the pyloric rhythm captured on the lvn (obtained in the second task).

3) The development of an automated procedure for determining the pyloric frequency from the optical/VSDI data, obviating the need for an initial manual study of the electrophysiological recording on the lvn. Additionally, the computational procedures developed in 1) and 2) were also validated.

1.5. Thesis Organisation

This thesis comprises six chapters. The first chapter contains this Introduction, which is followed by the literature reviews presented in chapter 2. The latter is divided into two main parts that focused respectively on the biology aspects (first part) and the signal processing methods (second part) described in this thesis. The third chapter refers to the first test of concept related to extracting the pyloric rhythm, with work and results which have been published in dos Santos, Andras and Lam, (2017a). Chapter 4 presents the work on the direct identification of pyloric neurons from the optical recordings produced using the VSDI technology, alongside the first validation of the results presented in chapter 3; see also publication by dos Santos, Andras and Lam, (2017b). Chapter 5 describes the work on the development of frequency estimators that would facilitate the determination of the pyloric frequency from the optical data/recording automatically. The methodology was discussed, with analysis on and comparisons with the latest work published in dos Santos *et al.* (2017). The sixth

and last chapter presents a brief summary of the work reported, including conclusions and future work.

2. Literature Reviews

This chapter has two main sub-sections; the first presents the biology context of this thesis, which describes the biological functions of the nervous system of the decapod crustaceans, alongside a technical introduction to the use of voltage-sensitive dyes (VSDs) in biological applications. The second describes and discusses a number of signal processing techniques, focusing primarily but not exclusively on the individual methods used in this work.

2.1. Biology

In this section, the stomatogastric nervous system (STNS) is introduced. This is followed by the technical description of the stomatogastric ganglion (STG) of the decapod crustacean, with discussions on how the central pattern generators (CPGs) are connected and, more relevantly, their functional relationships with the gastric mill and pyloric rhythm. The last section (2.1.5) describes voltage-sensitive dyes (VSDs) and their use in biological imaging applications, alongside a brief explanation on the elected dye (di-4-ANEPPS) for this thesis.

2.1.1. The Stomatogastric Nervous System (STNS)

The stomatogastric nervous system (STNS) is a neural network comprised of several ganglia. One of its primary duties is to control the motion of the gut and foregut across the phylum Arthropoda (Ayali 2009). In crustaceans, four compartments compose the foregut, which leads to four central pattern generators (CPGs): The oesophagus (esophageal rhythm), the cardiac sac, the gastric mill and the pylorus (Selverston *et al.*, 1998; Ayali, 2009). In decapod crustaceans the STNS consist of four interconnected ganglia: a pair of commissural ganglia (CoG) with several hundreds of neurons (Marder *et al.*, 1987; Kirby and Nusbaum, 2007; Follmann, Goldsmith and Stein, 2017), one

oesophageal ganglion (OG) with about 16 to 18 neurons (Marder and Weimann, 1992), and the stomatogastric ganglion (STG) with 25 to 32 neurons (Marder and Bucher, 2007)**.** The number of neurons depends on the species, cell type, and to some extent animal-to-animal variability (Selverston and Moulins, 1987; Kilman and Marder, 1996; Nusbaum and Beenhakker, 2002; Fénelon *et al.*, 2003; Bucher, Johnson and Marder, 2007; Watling and Thiel, 2012).

A general description of how the STNS is connected is as follows. The CoG and the OG are connected by a pair of inferior (ion) and superior (son) oesophageal nerves. The STG connects to the above via the stomatogastric nerve (stn); most of the motor neurons leave the STG via the dorsal ventricular nerve (dvn), which branches into two median ventricular nerves (mvn) and two lateral ventricular nerves (lvn). The latter is further divided into the dilator nerve (pdn) and pyloric nerve (pyn) (Selverston and Moulins, 1987). Figure 2 summarises the organisation of the STNS described here.

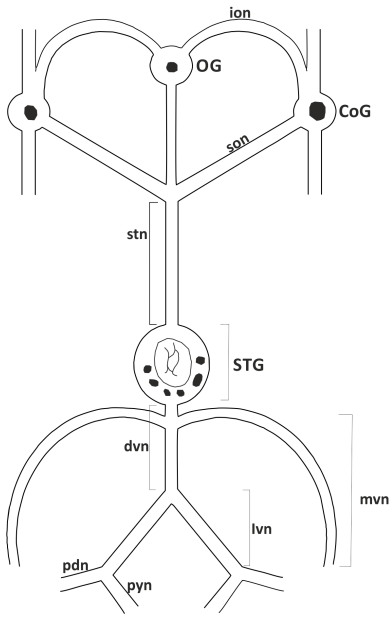

Figure 2 – A schematic view of the stomatogastric nervous system of decapod crustacean.

From a physiological viewpoint, the oesophageal rhythm allows the crustaceans to ingest the food; the cardiac rhythm controls the cardiac sac where the food is stored before passing through the gastric mill where food is chewed, enabling the food particles to be moved to the pyloric region for filtering (absorption or excretion). Each of these rhythms comprises a set of coordinated muscle

contractions, which arise from sets of synchronously or anti-phase firing neurons (Selverston and Moulins, 1987).

Importantly, when the STNS is isolated from an animal, and the basic leaving conditions are met (in a dish with a cold saline solution), some of the neuronal activity/rhythms are preserved as a result of its spontaneous activity remaining similar to those observed *in vivo*. The latter (pyloric rhythm) have been shown to last from several days up to two weeks (Rezer and Moulins, 1983; Heinzel and Selverston, 1988; Clemens, Combes, *et al.*, 1998; Clemens, Massabuau, *et al.*, 1998).

2.1.2. The Stomatogastric Ganglion (STG)

The STG is a ganglion unique to decapod crustaceans; it lies in the ophthalmic artery that carries the blood from the heart to the brain, on the dorsal surface of the foregut (Maynard and Dando, 1974; Selverston and Moulins, 1987; Stein, 2009). However, there are anatomical differences between species, however. In particular, the crab's stomach is in a horizontal position where the STG presents a more flat configuration, while in the lobsters the stomach is in an oblong position, implying that its STG has a 3D structure (Marder and Bucher, 2007). For example, see lobester's anatomy[4,5].

The STG is innervated by about 40 projection neurons, via the stn (stomatogastric nerve), from higher ganglia (CoG and OG). These ganglia have been found with modulatory input (neuromodulation) essential to activate the motor patterns as a result of the gastric and pyloric activity (Coleman *et al.*, 1992; Nusbaum and Beenhakker, 2002; Marder *et al.*, 2005; Marder and Bucher, 2007; Stein, 2009; Hedrich, Diehl and Stein, 2011). When this neuromodulation is interrupted (for example, a complete cut of the stn) both CPGs cease to function. However, the spontaneous activity of the pyloric rhythm is restored between 24-72 hours after the disturbance (Thoby-Brisson

[4] http://stg.rutgers.edu/images/STGfigures/Lobster_anatomy.jpg
[5] http://stg.rutgers.edu/images/STGfigures/SomaMapHomarus.jpg

and Simmers, 1998; Golowasch *et al.*, 1999; Golowasch, Abbott and Marder, 1999; Faumont *et al.*, 2005; Gansert, Golowasch and Nadim, 2007).

The STG contains 25 to 32 neurons including motor and interneurons (Marder and Bucher, 2007)**,** which collectively control 36 pairs of striated muscles. The latter drive the rhythmic movements of the foregut, with the so-called gastric mill and the pyloric rhythm, that represent two of the four CPGs of the STNS (Maynard and Dando, 1974; Selverston *et al.*, 1976; Stein, 2009; Hudson, Archila and Prinz, 2010; McGaw and Curtis, 2013a; Derby and Thiel, 2014), as described above in section 2.1.1.

The gastric mill controls the movement of the ossicles (calcified teeth), and the pyloric rhythm is responsible for the filtration of the food particles at the final step of digestion. Sections 2.1.3 and 2.1.4 below describe these two processes respectively in detail.

Cancer pagurus STG has 26 neurons, spread in a single layer. Each neuron is 25-120µm in diameter across the soma and ~20µm in the primary neurites and their branches are projecting to the centre of the STG, where the neuropil is shaped like a bundle of neurites in the centre of the ganglion (Baldwin and Graubard, 1995; Kilman and Marder, 1996; Nusbaum and Beenhakker, 2002; Marder *et al.*, 2005; Marder and Bucher, 2007). The cell bodies are displayed around the neuropil in the descending half of the STG, although the vast majority are congregated at the bottom part, as can be observed in Figure 3**.**

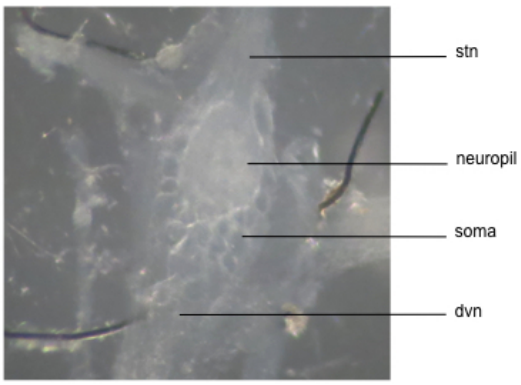

Figure 3 – Stomatogastric ganglion, view from dissection microscope, labelled with the primary structures: stn (stomatogastric nerve), neuropil, soma (individual cell body) and dvn (dorsal ventricular nerve).

Technically speaking, the neuropil (shown in Figure 3) is not a physical structure but a combination of neurites. Nevertheless, in electrophysiology this 'structure' is regarded as a 'cell', allowing recordings to be obtained directly (using sharp electrodes) or indirectly (with optical imaging). The signal emitted from this structure is mainly from LP (lateral pyloric) and PD (pyloric dilator) neurons since they present the larger and stronger neurites in comparison with the other neurons in the STG (Harris-Warrick *et al.*, 1992). As such, this enables the signal to be analysed, with the goal of studying the related frequency generated by these pyloric-timed neurons.

The circuit connections between the gastric mill and pyloric rhythm are shown in Figure 4. Here, it can be observed that there are two types of synapses in existence: electrical synapses (blue) that couple the membrane potentials of specific neurons, and inhibitory chemical synapses (red). The gastric mill network, described next in section 2.1.3, is composed of one lateral gastric (LG), one medial gastric (MG), four gastric mill (GM), one interneuron 1 (Int_1), and one dorsal gastric (DG) neuron. The pyloric network, described in section 2.1.4, is composed of one anterior burst (AB) interneuron, two PD, one LP, one inferior cardiac (IC), five pyloric (PY) and one ventricular dilator (VD) neurons; the two lateral posterior gastric (LPG) neurons are shared between both networks. The anterior medium (AM) neuron innervates the cardiac sac muscle, although it is usually included in the gastric mill. LPG neurons are usually part of the gastric mill, but it has been reported that they can switch to be a part of the pyloric rhythm (gastro-pyloric neurons) (Weimann, Meyrand and Marder, 1991; Norris, Coleman and Nusbaum, 1996).

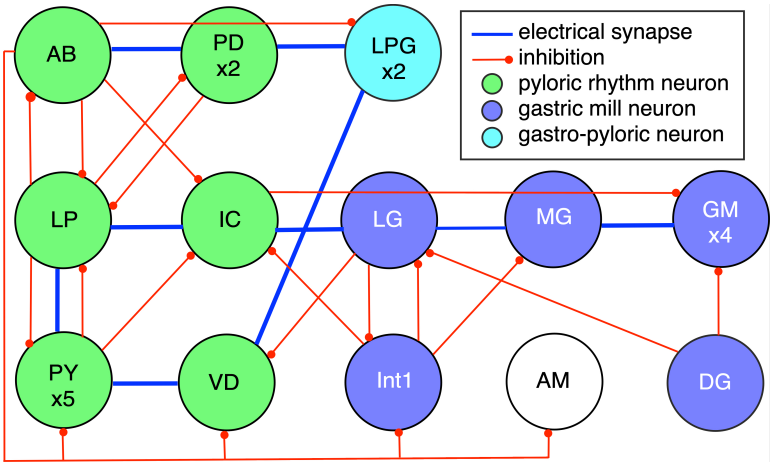

Figure 4 – Schematic representation of the STG system. In purple the neurons from the gastric mill, in green the neurons from pyloric rhythm and in blue the neurons that switch between networks.

2.1.3. The Gastric Mill

Huxley is the first person to use the term gastric mill to describe the chewing process in certain invertebrates (Huxley, 1880). In the STG the rhythm generated by the gastric mill is slower than the pyloric rhythm and intermittent; it usually switches on when the animal senses food. Once on, each cycle lasts from 5 to 10s, though it can go up to 20s (Wiese *et al.*, 1990; Marder and Bucher, 2007; Stein, 2009; Derby and Thiel, 2014).

The gastric mill produces different motor patterns which are not so well characterised; they are dependent on the need of effective mastication for a range of different foods (Harris-Warrick *et al.*, 1992; Heinzel, Weimann and Marder, 1993; Thuma *et al.*, 2003; Watling and Thiel, 2012; McGaw and Curtis, 2013b). So, neither *in vivo* nor *in vitro* the rhythm is continuously active or present at the same strength (Clemens, Combes, *et al.*, 1998; Clemens, Massabuau, *et al.*, 1998; Clemens, Meyrand and Simmers, 1998).

A pacemaker does not drive this rhythm. Instead, the driver is a reciprocal inhibition among the participating network neurons and interactions with ascending and descending projection neurons (Selverston and Moulins, 1987; Marder and Bucher, 2007; Blitz *et al.*, 2008; McGaw and Curtis, 2013a).

The gastric mill comprises 11 neurons: 10 motor neurons: AM, DG, LG, MG single neurons, two LPG and four GM neurons, and the interneuron 1 (Int_1). As explained previously in section 2.1.2, the two LPG neurons are shared by the respective circuits that generate the gastric mill and the pyloric rhythm.

The primary function of the gastric mill is to coordinate the movement between the three specialised ossicles: opening and closing of the two lateral teeth that move synchronously to grasp the food shreds, and the forward and downward movement of the medial tooth, that grate the food particles (Selverston and Moulins, 1987; Harris-Warrick *et al.*, 1992). This mastication process is known as the "cut and grind" movement (Hartline, 1979). The food enters the gastric mill by the cardiac sac, is macerated by the action of the three teeth and moves to the pylorus to be filtered to posterior digestion (Fénelon *et al.*, 2003).

The neuronal activity of the gastric mill is described as follows. The LG and the MG neurons fire and activate the muscles that close the lateral teeth making them hold the food particles. When the LG and MG neurons fire they inhibit all the others except the GM which continue to fire at low frequency, and the Int_1 fires when LG and MG are slowing down. The Int_1 triggers the excitation of the DG and AM which activate the medial tooth to be reset and inhibit the LG and MG neurons. When these neurons have ceased firing, the LPG fires, forcing the lateral teeth to pull open, this is followed by the firing of the four GM neurons which make the medial tooth tear food apart with movements forwards and downwards, scraping the food across held by the lateral teeth. When these last neurons recover, the cycle is completed and ready to start again (Selverston and Moulins, 1987; Heinzel, Weimann and Marder, 1993; Selverston *et al.*, 1998).

2.1.4. The Pyloric Rhythm

The pyloric rhythm of the crustacean STG is among the best well-known CPGs in invertebrates. It controls the pylorus or pyloric filter, responsible for filtering the macerated food, resultant from the

gastric mill, to be sent on to the gut and hepatopancreas for the further digestive process (Selverston, 2005).

The circuit in *C. pagurus* involves ten motor neurons: single cell neurons IC, LP and VD, two PD, five PY neurons and one interneuron AB (Selverston and Moulins, 1987; Weimann and Marder, 1994; Marder and Bucher, 2007).

The pyloric rhythm is characterised by a fast, strong and continuous triphasic rhythm (PD, LP & PY; see Figure 5) with a periodic frequency of 0.3-3Hz, commonly described as 0.5-1Hz. It is driven by a pacemaker group (AB-PD) triggered by the anterior burst (AB) neuron (Rezer and Moulins, 1983; Harris-Warrick *et al.*, 1992; Marder and Bucher, 2007; Stein, 2009; Hedrich, Diehl and Stein, 2011; Derby and Thiel, 2014). The frequency variation depends on multiple factors, such as animal-to-animal variation (Bucher, Prinz and Marder, 2005; Goaillard *et al.*, 2009; Williams *et al.*, 2013), temperature (Tang *et al.*, 2010, 2012; Caplan, Williams and Marder, 2014; O'Leary and Marder, 2014, 2016; Soofi *et al.*, 2014; Marder *et al.*, 2015) and neuromodulation (Nagy and Dickinson, 1983; Rezer and Moulins, 1983; Hooper and Marder, 1987; Nusbaum and Marder, 1988; Harris-Warrick and Marder, 1991; Norris, Coleman and Nusbaum, 1996; Hooper, 1998; Marder and Bucher, 2001; Dickinson, 2006; Stein, 2009).

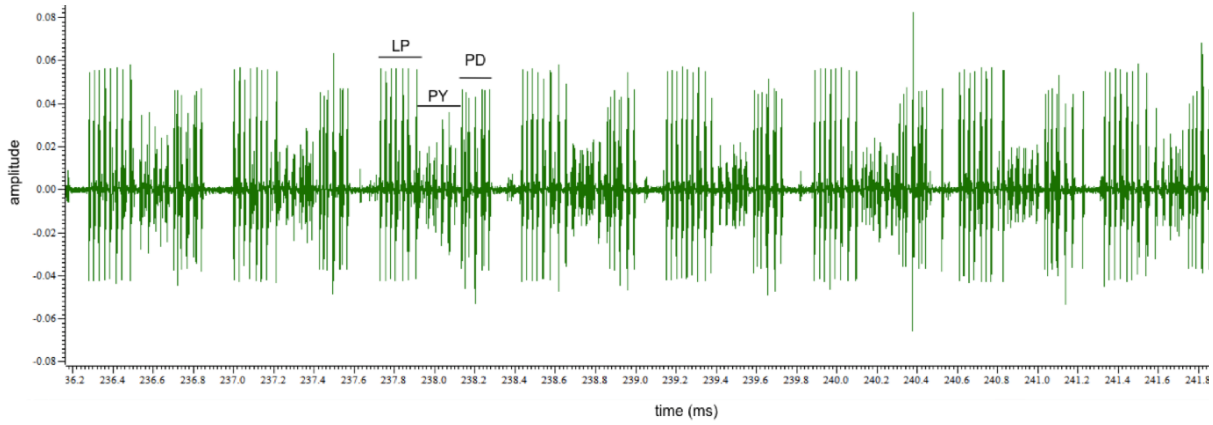

Figure 5 – An example of the pyloric rhythm recorded on the lvn, sowing the triphasic rhythm; LP, PY and PD neurons.

In vivo recordings have demonstrated the consistency and robustness of this rhythm, although the intensity of the rhythm is dependent on the animal's physiological status (Rezer and Moulins, 1983; Clemens, Combes, *et al.*, 1998; Clemens, Massabuau, *et al.*, 1998; Böhm, Dybek and Heinzel, 2001; Tang *et al.*, 2010; Stein, 2014; Marder, Goeritz and Otopalik, 2015). *In vitro* studies have shown that the strength of the spontaneous activity kept by the pyloric rhythm can be maintained from several days to a couple of weeks (Mizrahi *et al.*, 2001; Marder and Bucher, 2007; Soofi *et al.*, 2014).

Anatomically, the pyloric rhythm starts with the electrical coupling of the AB and PD neurons which works like a pacemaker; their burst action potentials inhibit all other neurons within the circuit. Additionally, there is a silent period between when the AB-PD stops firing and before both the LP and IC recover from the inhibition (see in Figure 5) and start firing. When the latter starts slowing down the firing, it causes the PY and VD neurons to fire, which inhibits the LP. PY and VD will continue firing until the AB-PD bursts again, starting a new cycle (Hartline, 1979; Selverston and Moulins, 1987; Harris-Warrick *et al.*, 1992; Marder and Bucher, 2007).

This electrical circuit (pyloric rhythm) is decoded into a functional biological system as follows. The firing of the pacemaker group opens the valve that connects the gastric mill with the pyloric region, allowing the food particles to flow to the pylorus; in other words, the muscles innervated from PD neurons are pulled in the opposite direction to dilate the pylorus. When the food arrives in the pylorus, the surrounding muscles are excited and dilate the next region, contracting the posterior one. This produces a peristaltic-like contraction that pushes in the posterior direction. The firing of the LP neuron causes a contraction of the lateral pyloric muscle, which prevents the valve from opening before the cycle is completed. The PY neurons are responsible for the movement of the sieve plates that sort out the food for further digestion (Selverston and Moulins, 1987; Selverston, 2005; Stein, 2009; Derby and Thiel, 2014).

2.1.5. Voltage-Sensitive Dye (VSD)

Voltage-sensitive dyes or potentiometric dyes have been used in imaging since early 1970 (Cohen, Keynes and Hille, 1968; Tasaki *et al.*, 1968) to facilitate studies *in vitro* and *in vivo,* with a wide range of animals such as amphibians (frogs and salamanders) (Konnerth and Orkand, 1986; Kauer, Senseman and Cohen, 1987), mammals (mainly rats, mice, ferrets, cats and monkeys) (Slovin, 2002; Petersen, Grinvald and Sakmann, 2003; Mohajerani *et al.*, 2010; Onat, König and Jancke, 2011), *Tritonia*, *Aplysia*, leech, goldfish, snails, squid, sea crabs and lobsters (Chemla and Chavane, 2010; Hill, Bruno and Frost, 2014; Frost and Wu, 2015).

VSD are dyes that bind to the cell membrane, where the changes in membrane potential (for example, at the time of an action potential) trigger voltage variations in relation to changes in the light which are subsequently captured by cameras (Baker *et al.*, 2005; Hill, Bruno and Frost, 2014). The emitted optical signals are linearly related to changes in the membrane potential; the small light intensity variations are enough to capture the action potential of a firing neuron without the need to average the data.

There are three main advantages to the use of VSD. The first is the possibility of simultaneous recordings from multiple sites in the field of view. The second is the high temporal resolution achievable since the dyes can record voltage changes of less than 1µs (Cohen, 2010). The third is that the dyes can be applied by bath or perfusion, which is a non-invasive procedure (Cohen, 2010). However, as with most fluorescence dyes, VSD has a significant disadvantage – namely, phototoxicity[6], which can be overcome/minimised with small intervals of light exposure and manual brightness adjustments of the light source. In combination, these two practices allow enough time for the preparation to recover between recordings and avoid light saturation (Schaffer *et al.*, 1994; Obaid *et al.*, 2004; Hoebe *et al.*, 2007; Cohen, 2010; Frost and Wu, 2015).

[6] Phototoxicity is a toxic reaction between a chemical and light exposure that can lead to cell death.

In passing, it is noted that VSD imaging (VSDI) has been used in small invertebrates to study the relatively small neural circuits, with large size neurons such as those of the leech, *Tritonia*, *Aplysia* and some decapod crustaceans such as crab and lobster (Zecevic *et al.*, 1989; Briggman and Kristan, 2006; Frost *et al.*, 2010; Stein and Andras, 2010; Städele, Andras and Stein, 2012; Hill, Bruno and Frost, 2014; Frost and Wu, 2015). Further details on the use of VDSI in *Cancer pagurus* are included in section 3.2.4.

For this thesis, the chosen dye was the di-4-ANEPPS (Cambridge Bioscience, Cambridge, UK) or Pyridinium. It belongs to the ANEP family (AminoNaphthylEthenylPyridinium) developed by Fluhler et al. (1985). Di-4-ANEPPS is a fast VSD, with response time in microseconds, frequently less than 10μsec. The dye is used as chemical probes that attach to cell membranes and change their fluorescence or absorbance, in response to electrical field changes registered in the transmembrane potential (Tsytsarev *et al.*, 2014). It exhibits a reasonably uniform 2-10% fluorescence change per 100mV (Loew, 2010; ThermoFisher, 2018). The fast membrane changes are recorded by contemporary high-speed cameras, which can record typically over 1,000 frames per second.

Di-4-ANEPPS has been used to stain preparations such as bacteria, cardiac tissues, myocardium, neurons, and proteins (Fromherz and Lambacher, 1991; Loew *et al.*, 1992; Sabnis, 2010; Tsemperouli and Sugihara, 2018). This dye was chosen due to its extensive use in neuroscience, as well as the fact that it has been previously used in crustaceans' nervous systems (*Cancer borealis*, *Cancer pagurus* and *Homarus gammarus*) (Stein and Andras, 2010; Städele, Andras and Stein, 2012; Follmann, Goldsmith and Stein, 2017).

Table 1 below presents a brief review of some of the most commonly used VSDs that have been used in the STNS of decapod crustaceans, including their absorption and emission wavelengths, and the time needed for each application. Here, it should be noted that all dyes were bath applied except the di-8-ANEPPS, which was injected into the cell bodies. These dyes were applied in the STG, with the exception of di-4-ANEPPDHQ which was applied in the CoG, whilst the RH795 was applied in both non-desheathed and desheathed STG. For the experimental dyes, only JULBD6 was able to achieve

similar performance to di-4-ANEPPS. Di-4-ANEPPS was the most common choice for short-term experiments that require high signal quality, whilst for long-term experiments, the RH795 would be preferred due to reduced toxicity in comparison with di-4-ANEPPS.

Table 1 – Resume table of dyes previously used in STNS.

Dye	Staining Applications	Biological Measuring Applications	Absorption (λmax)	Emission (λmax)	Colour in powder	Administration time	Relevant papers
di-4-ANEPPS	Bacteria, cardiac tissues, myocardium, neurons, proteins	Measuring membrane potential, preventing arrhythmias, probes for Na, K-ATPase reaction mechanism, assays for identifying taste-specific genes, quantum dots	497nm	705nm	Orange	25min	(Stein and Andras, 2010; Städele, Andras and Stein, 2012; Preuss and Stein, 2013)
di-4-ANEPPDHQ	Neurons, neural networks, brain slices, lipid particles	Functional imaging of neurons, cholesterol-enriched lipid domains	512nm	712nm	Infrared	30-60min	(Follmann, Goldsmith and Stein, 2017)
di-8-ANEPPQ	Cardiac myocytes, lipid membrane surfaces, lipid particles, neurons, proteins, sea urchin eggs	Measuring membrane potential, imaging exocytosis at fertilisation	498nm	713nm	Orange	20-30 min/per cell	(Stein, Städele and Andras, 2011)
RH795	Brainstem, cortex, neurons	Measuring membrane potential, probes for Na, K-ATPase reaction mechanism, examining the activity of ion channels	530nm	712nm	Red	30-60min	(Preuss and Stein, 2013; Goldsmith, Städele and Stein, 2014)
JULBD	Experimental dyes, synthesised at Molecular Photonics Laboratory (Newcastle University)*		540, 590 nm	–	Blue-green (aqua)	20min	(Bai *et al.*, 2014)
MJULBD			~525nm	–			
JULBD 1	Experimental dyes, synthesised at Molecular Photonics Laboratory (Newcastle University)*		349, 630nm	653nm	Blue-green (aqua)	20min	(Sirbu *et al.*, 2017)
JULBD 2			362, 641nm	658,721nm			
JULBD 3			359, 634nm	660, 729nm			
JULBD 4			324, 647nm	683nm			
JULBD 5			260, 616nm	653 nm			
JULBD 6			277, 376, 639nm	684nm			

This table has been adapted from Sabnis (2010); Benniston et al. (2011); ThermoFisher (2018). (*) https://research.ncl.ac.uk/mpl/synthesis/index.php.

2.2. Signal Processing

Signal processing is a powerful technology that has been shaping science and engineering in the past few decades; revolutionary changes have already been made in a broad range of fields including (traditionally) communications, radar and sonars, high fidelity music and video re/productions, medical imaging and diagnosis, and lattely genomics (Dougherty *et al.*, 2005), to name just a few. Technically, it is distinguished from other areas in computer science by the unique type of data which it uses: signals that originate as sensory data from the real world. Depending on the tasks at hand, these signals are analysed for a variety of reasons; for example, it is sometimes possible or necessary to seek an alternative representation of an apparently complex signal waveform by a limited set of parameters. On other occasions, more relevantly, such an alternative representation is instrumental to a detailed analysis of the signal at hand, which may often be used to facilitate a deep insight into the source that produced it. In other words, certain detailed characteristics of a signal which are not immediately apparent can often give important clues to the nature of the underlying signal source, or perhaps importantly, to the type of processing which has occurred between the source and the point at which the signal is recorded or detected.

The sub-sections that follow (2.2.1 to 2.2.11) are organised into different but necessary topics, which seek to provide a foundation background of the technologies and techniques used in the subsequent chapters of this thesis.

2.2.1. Duty Cycle (DC)

Before getting into the explanation of the duty cycle (DC), a brief explanation of the period (*T*) and frequency (*f*) is given. The period (*T*) is the smallest interval in a signal that is considered a signal to be repeated (see equation (1)); the signal is called periodic with period *T* (cycle duration or cycle per unit of time) commonly measured in seconds (s). Frequency (*f)* is represented by the number of

oscillations per unit of time, commonly measured in cycles per second or Hertz (Hz); frequency and period are inversely proportional as can be seen in equation (2) (Barrett and Pack, 2006). Figure 6 presents two sine waves with two different frequencies (or periods); the blue sine wave has a frequency of 1Hz with a period of 1s, while the orange represents a sine wave with a frequency of 0.5Hz with a period of 2s.

$$x(t) = x(t + T) \tag{1}$$

$$f = \frac{1}{T} \quad and \quad T = \frac{1}{f} \tag{2}$$

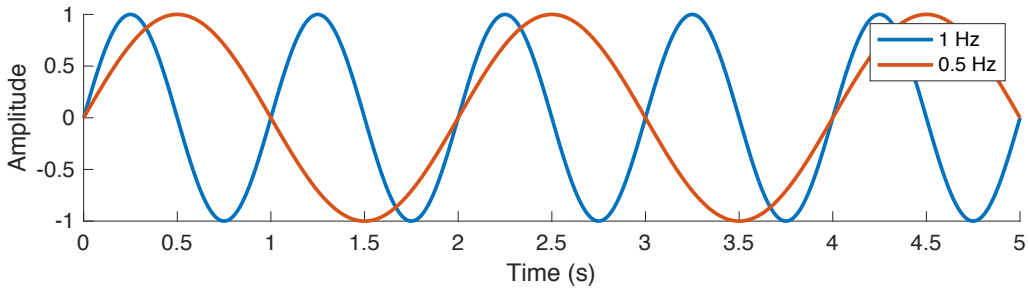

Figure 6 – Representation of two different frequencies.

In electrical engineering, the DC is defined as the percentage of time that such pulse is positive (or above zero) in a cycle (Barrett and Pack, 2006); mathematically, it is commonly measured as the percentage of time that a signal is positive (active) in an electrical device (Barrett and Pack, 2006). In biology, and more specifically in neurosciences, the DC is computationally defined as the proportion of time that a neuron is firing or active over one cycle (Ermentrout and Terman, 2010). In other words, it is the percentage of the time, calculated in each cycle, that the displayed waveform of the neuron is above its mean membrane potential (positive). Using the 1/3classical theory of Fourier/harmonics analysis (explained in section 2.2.2), this well-defined property of the DC enables studying any general, non-periodic waveform or, more relevantly, the waveform generated by a neuron that contains energy at individual harmonics of (the fundamental) frequency *f*.

In Figure 7, the DC is illustrated, in the time domain, with a rectangular pulse wave/train, with a DC = k/T, that is defined as the fraction of time when the amplitude (A) of the wave is positive.

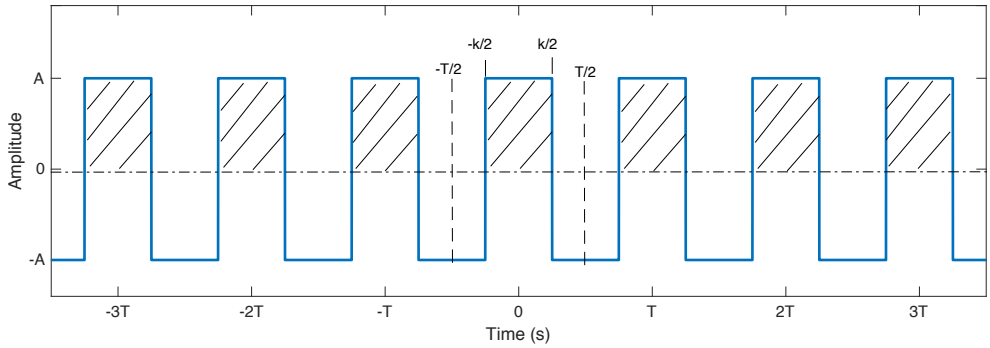

Figure 7 – An example pulse train with a duty cycle calculated as the ratio of k/T and a period from (-T/2) to T/2. The shaded area is the positive part of the pulse.

In the biological context, the relative phasing and DC of the component neurons in a network are extremely important for the generation of specific behaviour, as well as to maintain the rhythmic activity (Harris-Warrick *et al.*, 1992; Golowasch, Manor and Nadim, 1999). More relevantly, in the STG, the ability of the pacemaker (AB-PD) ensemble to maintain a constant DC at different frequencies in the pyloric circuit could explain how the full network maintains fixed phase relationships at different frequencies (Harris-Warrick *et al.* 1992).

2.2.2. Harmonics and Ratio of Harmonics (RH)

The study of harmonics is applicable to a wide range of problems; magnetic fields, echolocation, light, ultraviolet, ultrasound imaging, microscopy, pitch or gravitational fields, are just some examples (Zerilli, 1970; Caspi, Helm and Laslett, 1994; Tranquart *et al.* 1999; Dombeck, Blanchard-Desce and Webb, 2004; Fenton *et al.* 2011; Takekawa, Isomura and Fukai, 2012; Osmanski, Song and Wang, 2013).

Generally speaking, the harmonic of a signal is a wave whose frequency is an integral multiple of a frequency *f* (*2f, 3f,…, nf*) of some reference signal (Rode and Ladhake, 2010). In the classical study of a signal, it is called harmonic analysis or Fourier synthesis, although it can also be studied as the ratio (ratio of harmonics – RH) of the frequency between signal and reference.

Harmonic waves are a superposition of sine and cosine waves to reconstruct the periodic signal In other words, the harmonic analysis is the reconstruction process of a periodic waveform by adding together the fundamental frequency, defined as the sampling frequency ($1/T_0$), or the 1st harmonic (f_1), and the harmonics of various amplitudes (a_K for the K^{th} harmonics). This is represented by equation (3).

$$x(t) = \sum_{k=-\infty}^{\infty} a_K e^{i\left(\frac{2\pi}{T_0}\right)kt} \tag{3}$$

The previous equation (3) can be re-arranged in series such as:

$$f(t) = \frac{a_0}{2} + (a_1 \cos t + b_1 \sin t) + (a_2 \cos 2t + b_2 \sin 2t) + (a_3 \cos 3t + b_3 \sin 3t) + \cdots \tag{4}$$

The term ($a_1 \cos t + b_1 \sin t$) is known as the fundamental, the term ($a_2 \cos 2t + b_2 \sin 2t$) is called the second harmonic, the term ($a_3 \cos 3t + b_3 \sin 3t$) is called the third harmonic, and so on (Akansu and Haddad, 2001; James, 2011).

The first harmonic or fundamental frequency represents the harmonic with the longest wavelength and lowest frequency. The second harmonic wavelength has half of the length of the first, and its frequency is double that of the first. The third harmonic has 1/3 of the wavelength of the first with a frequency three times higher than the first. The pattern continues for all harmonics; the frequency will double, and wavelength shrinks proportionally. In general, the frequency for *n* harmonic and the respective wavelength (λ) are calculated as follows:

$$f_n = n * f_1 \tag{5}$$

$$\lambda_n = \frac{1}{n} * \lambda_1 \tag{6}$$

Where the frequency, f_n, of the nth cosine component in the previous, is $f_n = nf_1$ (harmonic frequencies). The frequency f_n is called the nth harmonic of f_1 because it is an integer multiple of the fundamental frequency f_1.

In studying harmonics, it should be noted a pure sine wave is the only periodic wave that does not carry any harmonics; instead, it has only a single frequency, commonly known as the fundamental

frequency, of a mono-frequency wave. This can be observed in Figure 8(A), where a perfect sine wave (red), having a frequency of 1Hz and its power spectrum analysis in Figure 8(B), with only one peak frequency. In this figure is also shown a pulse train wave (blue) and its harmonics (Figure 8(B)), carrying different frequencies at 1, 3 and 5Hz. For more detail on this topic, Arrillaga et al. (2000) provide a full discussion on the harmonics calculation of a rectangular train wave.

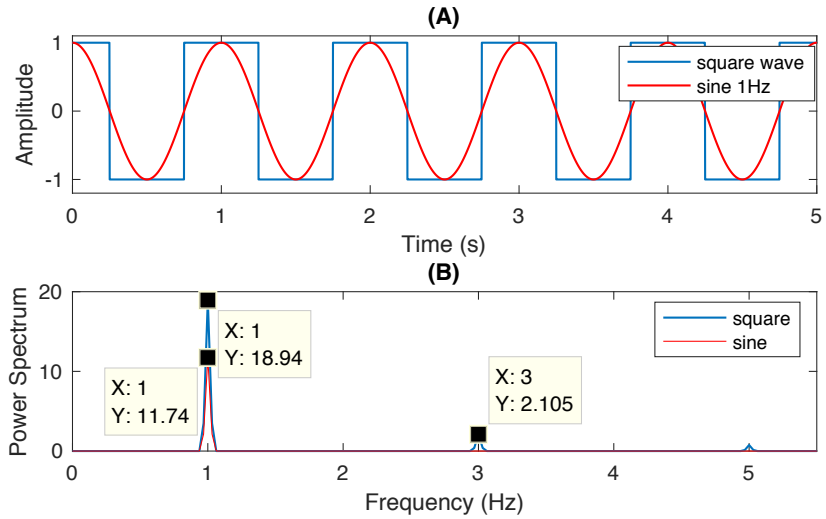

Figure 8 – (A) Pulse train and a sine wave of 1Hz. (B) The respective power spectra for (A). Note also the absence of even harmonics in the power spectrum computed for the rectangular pulse train; see equation (7) below.

Mathematically speaking, it can be shown that the sum of harmonics can reconstruct a signal (McClellan, Schafer and Yoder, 2016); in fact, the higher the number of harmonics added, the greater the detail of the reconstruction. However, it should also be noted that if the signal is noisy, the further harmonics added to the reconstruction of the greater detail of the noise may lead to 'overfitting', as the noise is embedded in the additional harmonics (James, 2011).

The above could be explained using the familiar example of the progressive JPEG compression technique, which computes the energy contained in the individual harmonics. Here, it is apparent that the first few harmonics, which carry the majority of the energy contained in a waveform (Sayood, 2012), are usually sufficient to approximate an image, with more details to be appreciated by adding higher harmonics. Indeed, this is illustrated by the results of the frequency analysis of the

rectangular train pulse as depicted in Figure 8(B), where the fundamental frequency f_1 (= 1Hz) carries the largest energy (= 11.74 units) of the original rectangular waveform (shown in blue).

In recent years, the ratio of harmonics (RH) or harmonics ratio (HR) has been adopted to quantify the step-by-step symmetry or rhythmicity within a stride by exploiting the periodicity extracted from the signal, offering an independent amplitude measure (Bellanca *et al.*, 2013).

Technically, RH offers a characterising global measure that underlines changes in symmetry as the defining characteristic between the individual walking patterns/steps. Here, it was suggested that, when describing or explaining RHs, the term "symmetry" should be emphasised as the defining characteristic instead of using the terms rhythmicity, dynamic stability, or walking balance. From an analytical viewpoint, the harmonic coefficients used to obtain the RHs directly correspond to the energy contained at harmonics of the fundamental frequency of any non-sinusoidal repetitive waveform. As such, these coefficients, expressed in the frequency domain, will uniquely describe the original signal waveform in terms of its shape and amplitude in the time domain.

Computationally, the RHs used in this thesis are based on the coefficients (a_n and b_n) of the Fourier series expansion, which is calculated by correlating the waveform, *x(t)*, with cosine and sine waves over a full period *T* or frequency *f*. For a rectangular pulse train whose amplitude and duty cycle (in %) are given as *A* and *d* respectively, the results, described in most textbooks (McClellan, Schafer and Yoder, 2016), are given in equation (7), which provides a complete description of the harmonics *(nf, n =1,2,…)* contained in *x(t)*. The latter can be used to characterise the rectangular pulse train of which *d* represents the duty cycle (in %) and, in general, any periodic waveform. Note here that without losing generality, the coefficients b_n, n = 1,2,… in this example are all zeros, as *x(t)* is symmetrical at t = 0. See Figure 7 (in section 2.2.1).

$$x(t) = Ad + \sum_{n=1}^{\infty} a_n \cos 2n\pi f t \ , \qquad where\ a_n = \frac{2A}{n\pi} \sin(n\pi d) \tag{7}$$

In this thesis, two harmonic ratios were used; namely, RH_{21} = a2:a1, which correspond to the ratio between the second and first harmonics and, R_{31} = a3:a1, the ratio of the third and first harmonics. They were calculated as $\frac{\sin 2\pi d}{2\sin \pi d}$ and $\frac{\sin 3\pi d}{3\sin \pi d}$ respectively.

A few notes are in order here. First, it should be understood that, based on equation (7), the first harmonic or fundamental frequency represents the pyloric frequency in the Fourier/harmonic expansion as described above. Second, in view of the uniqueness of the ordered set of harmonic coefficients obtained for a given (periodic) signal/waveform, the RH calculation by definition (above) should also afford us a unique and dimensionless characterisation (meaning that the *A* is cancelled out in the ratio calculation) of such a signal that is (naturally) amplitude independent. Third, perhaps most importantly, by applying the above analysis to a rectangular pulse train, RHs offer both a simple and effective quantitative measure of duty cycle discussed earlier (in section 2.2.1) in the time domain and, by virtue of the Parseval's theorem (see chapter 5), in the frequency domain.

2.2.3. Power Spectrum

The terms Power Spectral Density (PSD) or Energy Spectral Density are commonly known as power spectrum, which is a visualisation tool in the frequency domain where amplitude or a relative unit/value is displayed against frequency computed from a signal. Visually, it is a plot that represents the portion of energy per unit of time falling within a given frequency bin, with the spectrum showing the power distribution of the spectral components composing a signal (Nuttall and Carter, 1995; Stoica and Moses, 2005). The most common way to produce the power spectrum is by using a discrete Fourier transform (periodogram).

The power spectrum analysis presented in this thesis was calculated using the MATLAB command using `pwelch(x)` (MathWorks, 2016). This method consists of dividing the time series data into (possibly overlapping – Hamming window) segments, computing a modified periodogram of each segment, and then averaging the power spectrum density. In this research, the sampling frequency,

$f = \frac{1}{(1.5*10^{-3})} = 666{,}66Hz$ where 1.5*10^{-3}s or 1.5ms represents the sampling rate that is explained in section 3.2.4. Applying the Nyquist Theorem (Nyquist, 1928), the maximum frequency is thus limited to 333.33Hz. Note, to replicate a signal *x(t)*, Nyquist's Theorem requires that *x(t)* should be periodically sampled at a rate which must be at least twice the highest frequency (*d*) that is wished to be recorded; in other words, the sampling rate (the Nyquist rate) should be at least double the size of the highest frequency that must be recorded (Nyquist, 1928). Mathematically, this is summarised in the following equation (8), where *d* represents the highest frequency that is wished to be recorded.

$$Nyquist\ samplig = \frac{d}{2} \tag{8}$$

2.2.4. Continuous Wavelet Transform (CWT)

The Wavelet Transform (WT) is one of the best known practical signal transformation techniques, including the extensively documented Short Time Fourier Transform (STFT) and Wigner distribution and Hilbert Transform (described later in section 2.2.6) etc., designed to provide the time-frequency information of a signal. Specifically developed to address the major shortcoming of the long-established Fourier Transform in analysing non-stationary signals, where the individual spectral or frequency components may not exist at all times, WT is capable of providing the time and frequency information of such signal simultaneously. As a result, the so-called Continuous Wavelet Transform (CWT) offers a time-frequency or (mathematically) time-scale analysis of signals and images; for example, in experimental neuroscience, where many of the concerned signals/images are inherently complex and non-stationary – as in most real-world signals (Hramov *et al.*, 2015). This means that CWT has an exceptional ability to perform both time and frequency localisation, which is an important feature when analysing complex non-stationary signals, enabling the contribution of a particular scale (which is inversely proportional to frequency) at a particular given time to be determined. More generally, in addition, CWT benefits from simultaneous localising in time and frequency domain, by obtaining a reasonable approximation of the given function (*f*) with only a few

coefficients and/or revealing fine details in a signal with noise removed from a signal without appreciable degradation (Sifuzzaman, Islam and Ali, 2009; Adamczak, Makieła and Stępień, 2010).

Mathematically, if the (1-D) signal is real-valued, the CWT is a reversible transform which results in a (2-D) real-valued function of scale (≈ 1/frequency) and position (in time); specifically, for a scale parameter *a>0*, at position *b*, the CWT is computed as (Misiti *et al.*, 2018):

$$C(a,b;f(t),\psi(t)) = \int_{-\infty}^{\infty} f(t)\frac{1}{a}\psi^*\left(\frac{t-b}{a}\right)dt \tag{9}$$

where ψ^* represents the complex (mother) wavelet kernel (or 'window') that is respectively shifted or translated (with parameter *b*) and contracted/dilated (with parameter *a*) in time.

It should be noted that CWT as defined above was developed as an alternative approach to STFT to overcome the resolution. Analytically, since the time and frequency resolutions as determined by the parameter/variable *a* are inversely related, the CWT provides better frequency resolution when *a* is large and the length of the wavelet (and thus its effective time window) is long. Conversely, when *a* is small, the wavelet/window is short, and the resulting time resolution is maximised (or better localised), with the wavelet responding only to high-frequency components. Note here, translations of shifts in time by varying the values of *b* do not alter either the time or frequency resolution. Thus the computation of basic CWT equation (9) represents an inherent trade-off between time and frequency resolution, which is the key to CWT's success, making it well suited in principle to analysing signals with rapidly varying high-frequency components superimposed on slowly varying low-frequency components. Indeed, this is the main reason for the adoption of the CWT, as described in chapter 4, where initial attempts, as a test of principle, to identify the individual neurons within the pyloric circuit of the STG were made (dos Santos, Andras and Lam, 2017b). An illustration of this can be seen later in chapter 4, Figure 31.

2.2.5. Morlet and Morse Wavelets

The Morlet wavelet, or Gabor wavelet as it is known in mathematics, is one of the most popular wavelet analysis tools used to reveal the time-frequency structure of signals. Known particularly for its accuracy and superior time localisation property, it can be used in both time and frequency domain (Hramov *et al.*, 2015).

The time-frequency trade-offs or limitations described in the preceding section is a fact whose roots can be traced back to what is widely known as the *Heisenberg Uncertainty Principle* which applied originally to the momentum and location of moving particles in Quantum Physics. When applied to time-frequency information of a signal, this principle simply states that one cannot know the exact time-frequency representation of a signal; that is, it is impossible to know exactly what spectral components exist at exactly which instances of times. From a signal analysis viewpoint, therefore, what can be known with the CWT are the time intervals in which a certain band of frequencies exists. This latter fact is, in essence, a resolution problem that manifests itself as the aforementioned trade-offs in the time-frequency estimation of the non-stationary signal at hand.

Computationally, the CWT given in equation (9) does not exist at a specific time or a specific frequency. As such, the transform provides only a compromise in the battle between time and frequency localisation; *viz.*, a well-documented fact that wavelets are well localised on both time and frequency but not precisely or exactly localised in either. Here, the time-frequency characteristics of any wavelet can be defined by measuring the time range of a specific wavelet, Δt_ψ, which can be specified by the square root of the second moment of a given (mother) wavelet about its time centre or, similarly, the frequency range, $\Delta\omega_\psi$, where $\psi(\omega)$ is the frequency domain representation (for example Fourier Transform) of $\psi(t/a)$ (Akansu and Haddad, 2001). Given the inverse relationship between time and frequency resolution as described in the previous section (2.2.4), it can be shown that the product of Δt_ψ and $\Delta\omega_\psi$ is a constant (K) that is solely dependent on ψ; that is,

$$\Delta t_\psi \, \Delta\omega_\psi = K_\psi \tag{10}$$

Equation (10) provides the theoretical foundation for specifying the time-frequency characteristics of CWT in general and, in particular, any wavelets. More relevantly, it provides both a formal and practical means for selecting the most suitable ψ for the application at hand.

Whilst a formal discussion on the subject of wavelets specification or selection in terms of their time-frequency characteristic is beyond the scope of this thesis, two wavelet families relevant to this thesis are worthy of note here.

1. Morse wavelet is an analytic family of wavelets (by means of dilation and contraction) which have been widely used in applications ranging from signal/frequency modulations modulate signals with time-varying amplitudes and frequencies, to the with particular applications in localisation in the time domain the discontinuities within a signal (Olhede and Walden, 2002). As such, it offers a good time-frequency resolution for most general applications where a balanced estimation of the time and frequency information about a signal may be sought. An example of such an application is described in chapter 4 (see section 4.4) where exploratory studies of the complex signals obtained from the bath dyed STG sample were carried out in order that relevant spectral components could be identified (visually) using the standard time-frequency plot.
2. Morlet wavelet or Gabor wavelet was first known in mathematics as one of the most popular wavelet analysis tools used to reveal time-frequency structure of seismic data/signals (Morlet, Arens, Fourgeau and Giard, 1982; Morlet, Arens, Fourgeau and Glard, 1982). Known particularly for its superior time localisation property and estimation accuracy, it has since been used widely in many scientific and engineering studies and, relevantly, for neuroscience applications (Hramov *et al.*, 2015), with notable examples which include detailed analysis of the electrophysiological recordings commonly known as the electroencephalogram (EEG) (Jobert *et al.*, 1994; Herrmann, Grigutsch and Bush, 2005; Omidvarnia *et al.*, 2017; Ieracitano *et al.*, 2018). Mathematically, the real-valued Morlet wavelet can be defined as follows (Misiti *et al.*, 2018):

$$\psi(x) = Ce^{-x^2}\cos(5x) \tag{11}$$

Qualitatively, the Morlet wavelet has a Gaussian shape (the e^{-x2} terms), which is centred and normalised by the constant *C* to ensure an equal number of cycles in the (mother) wavelet (*a = 1*) for each frequency. To illustrate its superior time localisation property, a popular and similarly constructed real-value wavelet, defined mathematically as the second derivative of a Gaussian ($\psi(x) = Ce^{-x^2}(1-2x^2)$) and commonly known as the Mexican Hat, is constructed. This allows a direct comparison of the time-frequency characteristics of the two wavelets based on equation (10) described above. In essence, by varying the value of the scaling factor (*a*) in equation (9), the corresponding Δt_ψ and $\Delta\omega_\psi$ and their product (K_ψ) were computed for each specified resolution/value of *a*. The results are summarised on Figure 9 below.

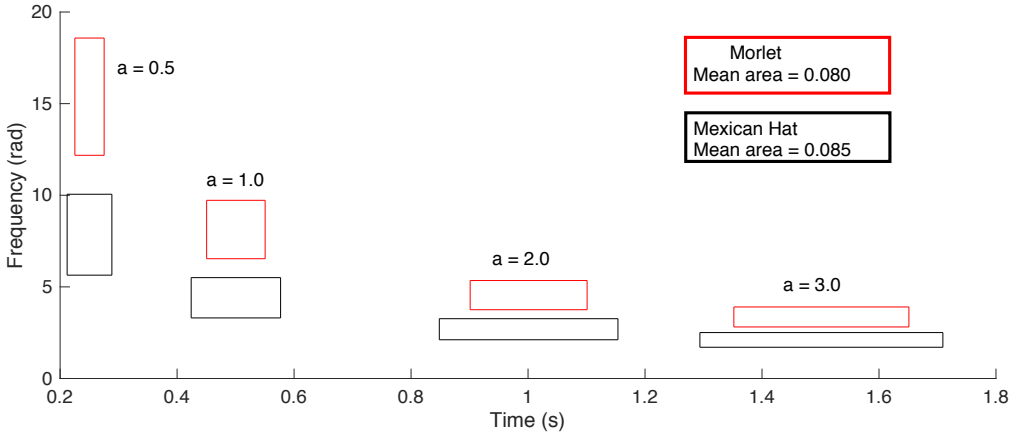

Figure 9 – The time-frequency spreads or boundaries of the Morlet(red) and Mexican Hat (black) wavelets computed for various resolution/values given by a. See equation (9). As per equation (10), the area is the same for each box which was computed as Δt_ψ (width) x $\Delta\omega_\psi$ (length) for the same family (displayed using the same colour). The superior time localisation of the Morlet wavelet, as is evident in the resulting narrower 'box' achieved for each scale/resolution specified by a, is apparent.

As expected, the results shown in Figure 9 clearly demonstrate the superior time localisation capability of Morlet over the similarly constructed Mexican Hat wavelet. Specifically, the significantly narrower width (Δt_ψ), and hence the 'spread' in time achieved by the Morlet wavelet at each scale (*a*) is most apparent. As a result, the Morlet wavelet was chosen in this work (described in chapter 4) to localise better or demarcate the transients between individual phases of the pyloric rhythm, which

are manifested extracellularly as discontinuities observed on the electrophysiological recording of the lvn.

2.2.6. Hilbert Transform

Hilbert transform (HT) is widely used in mathematics and signal processing to facilitate construction of an analytic representation of a real-valued and, importantly, a non-stationary signal (Hahn, 1996; MathWorks, 2016). As such, the transform was introduced to address the shortcomings of the classical Fourier Transform particularly in situations where there exist relationships between real and imaginary parts or, relevantly, the magnitude and phase of the transform. Specifically, HT has a complex-valued function as part of its Cauchy-Riemann principle known as the harmonic conjugate, which is used as a signal processing method to analyse non-stationary and nonlinear data by relating through the so-called HT integral (defined below) the real and imaginary parts of its Fourier transform. Here, it communicates with a phase shift of π/2 to every Fourier (or sinusoidal) component of a real-valued function *f(x)*, commonly measured in radians (Benitez et al. 2001). Mathematically, the transform or HT integral is defined by the following convolution function:

$$\mathrm{F(t)} = \frac{1}{\pi}\int_{-\infty}^{\infty} \frac{f(t')}{t-t'}\, dt' \tag{12}$$

where the integral is evaluated as a Cauchy principal value. Equivalently, equation (12) can be written using a linear/convolution operator, ⊛, in the form of mathematical convolution:

$$\mathrm{F(t)} = \frac{1}{\pi t} \circledast f(t) \tag{13}$$

Using the well-known Convolution Theorem, equation (13) and thus equation (12), can be evaluated in the frequency domain as the product of the complex-valued Fourier transforms of the two functions of $\frac{1}{\pi t}$ and $f(t)$ respectively. Importantly, the latter enables HT integral to be computed in three relatively simple steps: first, the Fourier transform of the signal *x(t)* is calculated. Second, the negative frequencies are rejected or removed from the result obtained by step one. Note here, this is

due to the result of the Fourier transform of $\frac{1}{\pi t}$, whose calculation is beyond the scope of this thesis. Third and lastly, the standard inverse Fourier transform is applied, resulting in a complex-valued signal (*Z(t)*) where the real (*X(t)*) and the imaginary (*Y(t)*) parts collectively form the Hilbert transform pair.

From a signal processing perspective, an important property of the Hilbert transform is that if a signal *x(t)* is *mono-component* (for example *x(t)* has only one spectral/frequency component), the time derivative of instantaneous phase $\theta(t)$ derived from *x(t)* can be attributed with physical meaning as the instantaneous frequency ω(t) of the signal x(t):

$$\omega(t) = \frac{d\theta(t)}{dt} \tag{14}$$

It follows that the $\theta(t)$, the instantaneous phase information of *x(t)* can be directly obtained from the HT integral, defined in the preceding paragraph above as *Z(t) = X(t) + iY(t)*, simply by the arctangent of the complex valued quotient of the imaginary and real parts of *Z(t)*:

$$\theta(t) = tan^{-1}\left(\frac{Y(t)}{X(t)}\right) \tag{15}$$

In section 4.6, Hilbert transform is going to be used exclusively to compute the instantaneous phases of two input/signals, x_1 and x_2, represented in the Hilbert space to the correspondent analytical signals (h1 and h2), using the in-built MATLAB functions/commands: `h1 = hilbert(x1)` and `h2 = hilbert(x2)` (MathWorks, 2016; McClellan, Schafer and Yoder, 2016). The results, described as the respective Hilbert spectra, `h1` and `h2`, facilitated the estimation of the instantaneous phase relationship between the inputs `x1` and `x2`.

2.2.7. Signal-to-Noise Ratio (SNR)

Signal-to-noise ratio (SNR) or S/N is a standard measure, which is used to compare pressure fluctuations amplitudes of audio/sound waves or the level of the desired signal to the level of background noise. Commonly measured in dB, an SNR of zero dB (SNR = 0dB) corresponds to a ratio

of 1:1 between signal and noise, meaning that the sound and noise levels are equal. If the ratio is larger than one (for example x:y, where x>y), then SNR > 0dB; this indicates the signal strength or amplitude is larger than that of the noise. Conversely, a ratio (x:y) smaller than one corresponds to an SNR < 0dB, revealing that the signal is smaller than the reference (Norton and Karczub, 2007).

In practice, signal and noise are relative terms, as most real-world waveforms consist of signal plus noise mixed together. Here, depending on the task at hand, the signal refers to the portion of the waveform of interest, while the noise is everything else. Often the goal of signal processing is to separate signal from noise, to identify the presence of a signal mixed with noise, or to detect features of a signal buried in noise. It follows that SNR is defined as the relative amount of signal and noise energies present in a waveform, as follows:

$$SNR_{dB} = 10\ log_{10}\left(\frac{P_{signal}}{P_{noise}}\right), \tag{16}$$

where *P* represents the averaged power (amount of energy per unit of time) with the result expressed in dB as described above. Equivalently, equation (16) is often computed as a ratio of signal-to-noise that is measured in their respective root-mean-squared (RMS) amplitudes; that is, $SNR_{dB} = 20\ log_{10}\left(\frac{Signal}{Noise}\right)$. This is due to the fact that the power of a signal X is proportional to the square of the RMS amplitude of X; for example, Power (X) $\propto (X_{RMS})^2$. Using this formula, the dB scale can be converted to a linear scale, by evaluating the inverse, as: $SNR_{linear} = 10^{(db/20)}$. For example, a ratio of 20dB means that the RMS value of the signal was 10 times the RMS value of the noise and, conversely, -20dB means that the signal is 1/10 (or 10%) of the noise in RMS units.

In passing, noise generated by optical imaging techniques that are used for electrophysiological recordings can be categorised in different ways (Cohen, 2010). There are three main types of noise described affecting such recordings. One is the shot noise or Poisson noise that represents the limit of accuracy with which light can be measured due to photon fluctuations. Another is the extraneous or technical noise, which can be caused by different factors including fluctuations in the output of

the light source, vibrations or movement of the preparation. The last noise category is the dark or read-out noise caused by the recording cameras (Baker *et al.*, 2005; Cohen, 2010).

In this thesis, the SNR was measured in all recordings; however, the sources of noise were not individually separated. See further details in sections 3.3 and 3.4.

2.2.8. Singular Spectrum Analysis (SSA) and Sequential SSA (s-SSA)

SSA is a nonparametric statistical method which is used across different scientific fields including mathematics, economics, meteorology, oceanography, volcanology, biomedical engineering and medicine (Pereira *et al.*, 2004; Carniel *et al.*, 2006; Hassani, Heravi and Zhigljavsky, 2009; Seitola, Silén and Järvinen, 2015). In particular, it has been used to solve a wide variety of problems in time-series analysis including multivariate statistics, dynamical systems, signal processing, smoothing, extraction of seasonality components, simultaneous extraction of cycles with short and long periods, extraction of periodicities with varying amplitudes, finding structure in short time series, among others (Golyandina, Nekrutkin and Zhigljavsky, 2001; Hassani, 2007; Ghaderi, Mohseni and Sanei, 2011; Golyandina and Zhigljavsky, 2013; Lam *et al.*, 2016). Originally introduced in the 80s by Broomhead & King (1986) and Fraedrich (1986), the procedure gained its widespread popularity 15 years later; for example in Golyandina et al. (2001), which are the guidelines followed by this thesis.

Technically, the nonparametric technique of the SSA makes no prior assumptions about the data and, as such, explains its versatility across many subject domains. As described above, it can be used to analyse linear or nonlinear, stationary or non-stationary, Gaussian or non-Gaussian data series.

Comparing with traditional methods used in time series analysis, which are based on either an autoregressive approximation model or structural characteristics (which usually assume normality of the residuals and/or stationarity of the time series) (Hassani, 2010), SSA is recognised as a data-driven or model-free computational tool for time series structure recognition and identification.

Loosely speaking, SSA relies on the principle of the multivariate technique of principal component analysis (PCA) with the variables analysed being lagged versions of a single time series variable

(Jolliffe, 2002). Thus, it is commonly applied to time series that are governed by recurrent linear formulae to forecast the new data points. There are two methods to construct the confidence intervals: the *empirical* method and the *bootstrap* method. The empirical method relies on confidence intervals that are constructed for the entire series, while bootstrap the method relies on confidence intervals built for the continuation of the signal, which are the main components of the entire series (Golyandina, Nekrutkin and Zhigljavsky, 2001). The method used in this thesis was the empirical method.

Technically speaking, the basic approach of SSA seeks to decompose a set of original time series using singular-value decomposition (SVD) of the so-called trajectory matrix constructed upon the time series into a mixture of a small number of independent and interpretable components. For example, a slowly varying trend, oscillatory components and a 'structureless' noise (Golyandina, Nekrutkin and Zhigljavsky, 2001; Hassani, 2007; Golyandina and Zhigljavsky, 2013):

$$S = S_{signal} + S_{noise} \tag{17}$$

where S is the original time series and S_{signal} and S_{noise} represent the lagged-covariance matrices of the signal and 'structureless' noise components respectively (Elsner and Tsonis, 1996). To compute accurately S, this process makes three assumptions; namely, the noise is white (random signal with equal intensity at various frequencies), the signal is autocorrelated (correlation of the signal with a delayed copy of itself), and the record is long enough. More generally, one needs not assign any stochastic meaning to the term 'noise', by observing that the concept of a deterministic stationary 'noise' series (*i.e.* noise that does not change over time) is more convenient for SSA when it deals with a single trajectory of a time series rather than a sample of such trajectories (Golyandina, Nekrutkin and Zhigljavsky, 2001).

The most common approach to SSA is performed in four successive steps: *Embedding* (in section 2.2.8.1), *Singular-Value Decomposition* (SVD) (in section 2.2.8.2), *Grouping* (in section 2.2.8.3), and *Diagonal Averaging* (in section 2.2.8.4). These four steps are often grouped into two main categories (decomposition and reconstruction), hence the reason some literature claims that SSA is composed

of two main complementary steps each divided into sub-steps (Golyandina, Nekrutkin and Zhigljavsky, 2001; Hassani, 2010). Qualitatively, the first two stages concern the decomposition of the time series, and the last two stages reconstruct the original series based on forecasting data points. A summary of each of these four stages following the approach described and detailed by Golyandina et al. (2001; Golyandina & Zhigljavsky (2013) is given below.

2.2.8.1. Embedding

Embedding serves to map the original time series to a sequence of multidimensional lagged vectors, being represented by a trajectory matrix – the Hankel matrix (see equation (18)) – which is regarded as a mapping that transfers one-dimensional time series $F = (f_0, \ldots, f_{N-1})$ onto the multidimensional series $X_1, \ldots, X_K$ with the vectors $X_i = (f_{i-1}, \ldots, f_{i+L-2})^T \in \Re^L$, where $K = N - L + 1$. Vectors X_i are called *L-lagged vectors*.

$$X = \left(x_{ij}\right)_{i,j=1}^{L,K} = \begin{pmatrix} f_0 & f_1 & f_2 & \cdots & f_{K-1} \\ f_1 & f_2 & f_3 & \cdots & f_K \\ f_2 & f_3 & f_4 & \cdots & f_{K+1} \\ \vdots & \vdots & \vdots & \ddots & \vdots \\ f_{L-1} & f_L & f_{L+1} & \cdots & f_{N-1} \end{pmatrix} \tag{18}$$

At this step, only one parameter is important, that is the window length L, which is an integer such that $2 \leq L \leq N-1$ and N is the number of points/samples of the signal (N>2). If L is sufficiently large, then each L-lagged vector X_i can be considered a separate series and dynamics or specific characteristics can be analysed independently. A schematic diagram illustrating the above is given in Figure 10.

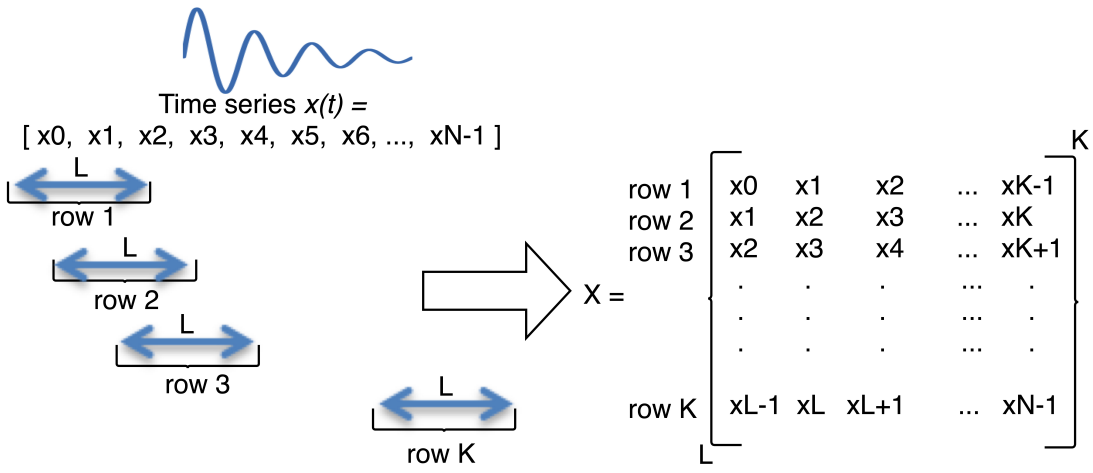

Figure 10 – Schematic diagram of the Hankel matrix. N is the number of points in the signal, L is the window length and K = N-L+1.

2.2.8.2. Singular-Value Decomposition (SVD)

The second step of the SSA is the singular-value decomposition (SVD) of the trajectory matrix into a sum of rank-one bi-orthogonal matrices. SVD can be described in multiple ways depending on its use. Here, the description relates to the used methodology leaving other explanations aside. So, SVD of an arbitrary nonzero $L \times K$ matrix $X = [X_1 : \ldots : X_K]$ is a decomposition of X in the form

$$X = \sum_{i=1}^{d} \sqrt{\lambda_i} U_i V_i^T \tag{19}$$

where λ_i $(i = 1, \ldots, L)$ are eigenvalues of the covariance matrix $S = XX^T$ arranged in decreasing order of magnitudes ($\lambda_1 \geq \ldots \geq \lambda_L \geq 0$), and d = rank (X) such that the covariance matrix is LxL (square) and positive definite:

$$d = \max\{i, such\ that\ \lambda_i > 0\} = rank\ (X) \tag{20}$$

noting that $U_1, \ldots, U_L$ are the orthogonal system of the eigenvectors of the matrix S (or left singular vector of X) corresponding to these eigenvalues, and V_i, … denote the right singular vectors of X in equation (19). Here, given that

$$V_i = \frac{X^T U_i}{\sqrt{\lambda_i}}, (i = 1, \ldots, d) \tag{21}$$

or

$$X^T U_i = \sqrt{\lambda_i} V_i \tag{22}$$

then the SVD of the trajectory matrix *X* known as expansion can be written as

$$X = X_1 + \cdots + X_d \tag{23}$$

where $X_i = \sqrt{\lambda_i} U_i V_i^T$. These X_i matrices have rank one so are called elementary matrices. The collection $(\sqrt{\lambda_i}, U_i, V_i^T)$ is also known as the *i*th eigentriple of the SVD. Figure 11 has a schematic representation of the above step, including also the sizes/dimensions of the individual matrices.

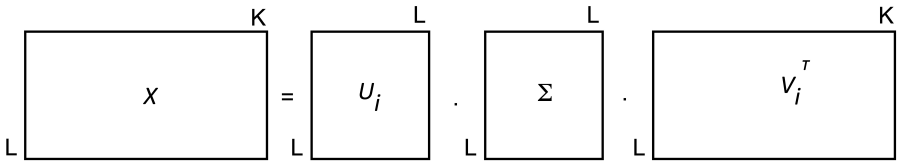

Figure 11 – SVD schematic representation of matrix rank separation.

2.2.8.3. Grouping

After the above first two steps (decomposition) the first step in reconstruction is the grouping. This phase corresponds to splitting the matrices, computed at the previous stage (SVD), into several groups and summing the matrices within each group. It is represented by partitions of set indices {1, ... , *d*} grouped in *m* disjoint subsets $I_1, \ldots, I_m$, each group of indices $I = \{i_1, \ldots, i_p\}$. Then the resultant matrix X_I corresponding to the group *I* is defined as $X_I = X_{i1} + \ldots + X_{ip}$. These matrices are computed for $I = I_1, \ldots, I_m$ (based on the *eigentriple* grouping) and the expansion of equation (23) then leads to the decomposition:

$$X = X_{I_1} + \cdots + X_{I_m} \tag{24}$$

A Hankel matrix can represent the result of this grouping stage as a sum of several resultant matrices, each of which corresponds to an orthogonally transformed 'component' of *X*. In other words, X can be reconstructed as the sum of *m* such components using the SSA procedure, with *m* determined by means of the so-called scree plot; for example, see sections 3.3 and 3.4.

2.2.8.4. Diagonal Averaging

The fourth and last step of SSA is the diagonal averaging, which transforms each of the previous resultant matrices of the grouped decomposition into a time series of length *N* and represents a linear additive component of the original series. As such, this stage aims to decompose the original time series into the several additive components (as separated by the grouping step described above). It represents the 'separability' of the SSA, a property of this technique. Briefly, it characterises how well different components can be separated from each other. It is a linear operation that maps the trajectory matrix of the initial series into the initial series itself. In simple terms, the separability is associated with how two or more components are related together; if they are mutually exclusive, then they present a weak separability, on the other hand, if they are independent they present a strong separability.

Computationally, let Y be an L × K matrix with elements, 1 ≤ i ≤ L and 1 ≤ j ≤ K. We set L* = min (L,K), K* = max(L,K) and N = L + K − 1. Let Y = Y*, if L < K and Y = $(Y^*)^T$ otherwise. Diagonal averaging transforms the matrix *Y* to the series $x_0, \ldots, x_{N-1}$ by the following equation (25) as depicted in Figure 12:

$$g_K = \begin{cases} \dfrac{1}{k+1} \displaystyle\sum_{m=1}^{k+1} y^*_{m,k-m+2} & for\ 0 \le k < L^* - 1, \\ \dfrac{1}{L^*} \displaystyle\sum_{m=1}^{L^*} y^*_{m,k-m+2} & for\ L^* - 1 \le k < K^*, \\ \dfrac{1}{N-k} \displaystyle\sum_{m=k-K^*+2}^{N-K^*+1} y^*_{m,k-m+2} & for\ K^* \le k < N. \end{cases} \qquad (25)$$

$$X = \begin{Bmatrix} x0 & x1 & x2 & x3 & x4 & x5 & x6 \\ x1 & x2 & x3 & x4 & x5 & x6 & x7 \\ x2 & x3 & x4 & x5 & x6 & x7 & x8 \\ x3 & x4 & x5 & x6 & x7 & x8 & x9 \end{Bmatrix}$$

Figure 12 – Schematic representation of the fourth stage of the SSA (diagonal averaging) in a matrix form; see coloured coded expression in equation (25).

The last equation (25) corresponds to the averaging of the matrix elements (i, j) over the 'diagonals', where *i + j = k + 2*; thus, the choice of *k = 0* gives $x_0 = y_{11}$, for *k = 1* there is $x_1 = \frac{y_{12}+y_{21}}{2}$, and so on. From the viewpoint of the reconstruction of X, it should be noted that such a diagonal averaging process provides an in-built low-pass filtering capability that is simple and effective.

Lastly, in passing, it is often observed that when signals or time series with complex structures have either weak or even absence of separability, the SSA will not reach accurate results. As a result, modified SSA techniques such as SSA with single and double centring, Toeplitz SSA and sequential SSA (s-SSA) (Hassani, 2007, 2010) start to emerge.

2.2.8.5. SSA Summary

For analysis in the presented thesis s-SSA was the approach that was chosen. Figure 13 presents a schematic representation, which summarises the four stages of the SSA technique previously explained in sections 2.2.8.1 to 2.2.8.4.

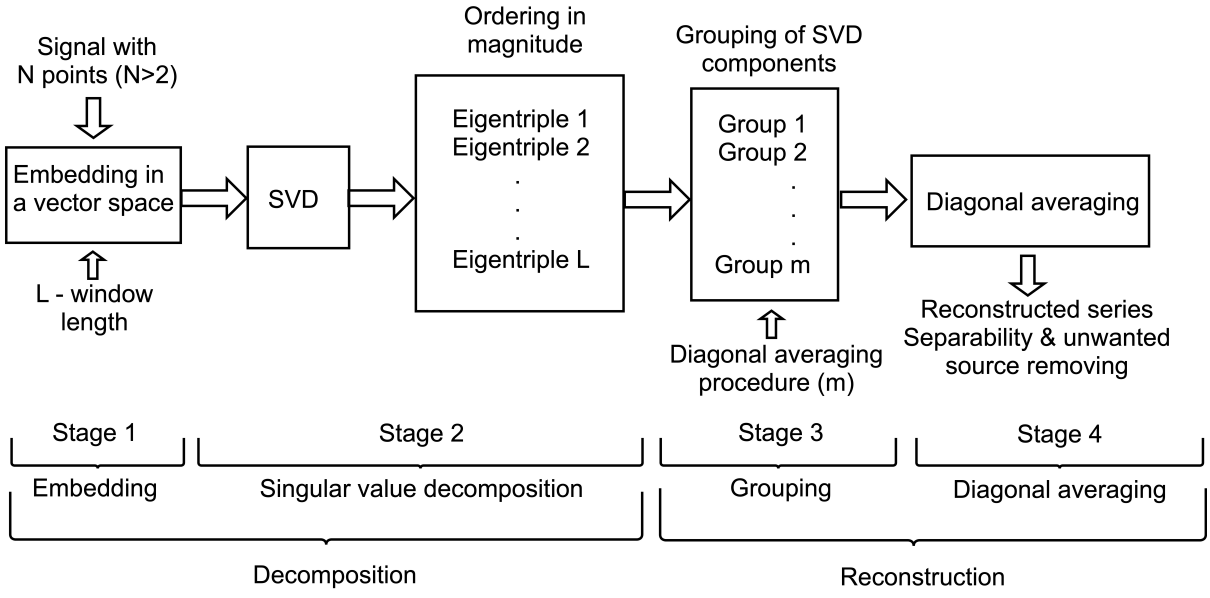

Figure 13 – Schematic representation of four stages of the SSA procedure. Adapted from Iranmanesh et al. (2012).

2.2.8.6. Sequential SSA (s-SSA)

The Sequential SSA (s-SSA), also known as Multi-stage SSA or Reiterated SSA (Golyandina, Nekrutkin and Zhigljavsky, 2001), is no less than a series of SSA applied to the data, where the window length *L* plays the most critical role in the technique. Essentially, an SSA is applied to the original data with a window length L_1; a second SSA is applied to the residual with an L_2, and this process could be repeated as many times as needed. Thus, for a two-stage s-SSA algorithm, the first SSA is applied to the original data, which extracts some signal components; then the second SSA is applied to the residuals of the first SSA, to extract further components. More specifically, the first window length is chosen by calculating the minimum number of frames/samples (L_1) per cycle averaged over the sampled date/sequence, as explained later in equation (26) in section 3.3. The second window length (L_2), which is often larger than the first ($L_2 > L_1$), adds around 25% more frames to allow for the (natural) variations in cycle length of the periodic component extracted from the original data.

Once there are two or more extracted sets of time series components they can be grouped into different ways. For example, if in the first stage a rough trend was extracted and at a second stage other trend components were extracted, then they can be added together to obtain a more accurate trend (Golyandina, Nekrutkin and Zhigljavsky, 2001; Golyandina and Zhigljavsky, 2013). As such, this provides a multiresolution approach to signal extraction as described later in chapter 3. Figure 14 is a schematic representation of the above (s-SSA).

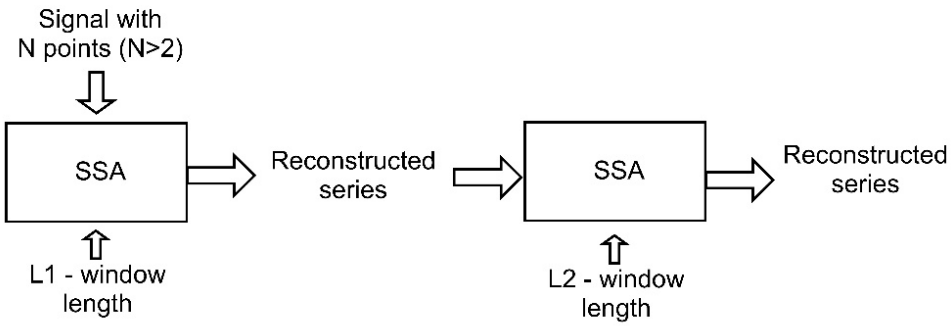

Figure 14 – Schematic diagram of s-SSA.

I should emphasize the importance of the choice of the best window length (L) (maximum time lag of autocorrelation) to achieve optimal performance by ensuring the most accurate separation of noise and signal (components). Briefly speaking, the window should be as large as possible but not larger than half of the number of data points (N). This is due to the fact that, as L increases in size, the computational complexity in handling the trajectory matrix also increases in the order of approximately $O(L^2)$. More importantly, if L is larger than half of N, the resulting trajectory matrix would just have an inverse shape, whilst the values of its elements would remain the same (or mirrored). In general, the larger the window, the smaller are the errors and more robust is the method. However, if the window becomes too large, then the noise could be incorporated within the window, especially if dealing with datasets with weak separability (Golyandina, 2010; Atikur Rahman Khan and Poskitt, 2013; Shaharudin, Ahmad and Yusof, 2015; Wang *et al.*, 2015).

2.2.9. Principal Component Analysis (PCA)

PCA is a mathematical/statistical procedure which involves finding the orthogonal linear combination of a set of variables that has maximum variance. By removing the possible correlations between the original variations, it uses an orthogonal transformation to convert a set of observations of these variables into a smaller set of values of linearly uncorrelated variables called principal components (PC). In other words, PCA is a dimension-reduction tool that is used to reduce a large set of variables (correlated variables) to a smaller set (uncorrelated variables/principal components) to facilitate approximation with minimal information loss (Jolliffe, 2002; Haykin, 2008; Jolliffe and Cadima, 2016). Thus, PCA is primarily used to reduce the risk of over-fitting in multivariate datasets, by reducing the dimensionality or the number of variables following the transformation.

First proposed by Karl Pearson in 1901 (Pearson, 1901) and later by Hotelling (1933), PCA was initially used in meteorology and oceanography. To date, it has applications in agriculture, genetics, geology, food research, psychology, economics, ecology, chemistry and neurosciences among others

(Byrne, Crapper and Mayo, 1980; Overland *et al.*, 1982; Berg *et al.*, 1995; Balsera *et al.*, 1996; Beauchemin, Hesterberg and Beauchemin, 2002; Rocchi *et al.*, 2006).

Broadly speaking, while PCA can be (and is often) used to transform one set of variables into another smaller set, the newly created variables are not usually easy to interpret. As a result, the more successful applications of PCA in signal processing are in contexts such as signal/image compression where data reduction, rather than interpretation, is of primary importance. In many applications, PCA is also used to provide information on the so-called "true dimensionality" of a data set. Formally, if a data set includes *m* variables, one must establish if all *m* variables are needed in order to represent the information, or alternatively, one can establish that the variables can be recombined into a smaller number (as true dimensionality) that still contain most of the information. Qualitatively, PCA operates by transforming a set of correlated variables into a new set of uncorrelated variables. Note that if the variables in a data set are already uncorrelated, PCA is of no value compared with Gaussian noise/distributions. In addition to being uncorrelated, the resulting principal components are orthogonal and are ordered in terms of the variability they represent. The first principal component (PC_1) represents, for a single dimension (variable), the greatest amount of variability in the original data set. Each succeeding orthogonal component (PC_k) accounts for as much of the remaining variability as possible. The operation performed by PCA can be described in a number of ways, but the geometrical interpretation of rotation is the most straightforward. The latter is readily understood by observing that for PCA to decorrelate two variables it simply needs to rotate the two-variable data set (in the 2-D plane) until the data points are distributed symmetrically about the mean. In the decorrelated condition (for example, $PC_1 \,.\, PC_k = 0$, $k = 2, 3, ...$), the variance is maximally distributed along the two orthogonal axes. One should also note that it could be necessary to centre the data by subtraction of the mean prior to rotation.

Computationally, the PCs are generated by the eigenvalue decomposition of the data covariance/correlation or by SVD of a data matrix. Eigenvalue decomposition (eigendecomposition) or spectral decomposition concerns the decomposition of a square matrix into eigenvalues ($\lambda = \sigma^2$)

and eigenvectors. Such a decomposition often takes the name of matrix diagonalisation, so it implies that only diagonalisable matrices can use this technique (Weisstein, 2018). The closely allied technique of singular-value decomposition (SVD), described in section 2.2.8.2, concerns the factorisation of a matrix *X* (real or complex) into a product of three matrices X = $V\lambda U V^T$, the so-called eigentriple (Jolliffe, 2002); see also 2.2.8.3.

The PCA technique is further discussed in section 4.5 as a potential approach to de-correlate the characterising triphasic structure of the pyloric rhythm, which is generated by the individual neurons.

2.2.10. Independent Component Analysis (ICA)

ICA is a statistical and computational method (used for example in machine-learning) for separating hidden factors (as additive subcomponents) from a multivariate signal or random variables typically given as large databases of samples (Hyvärinen, Karhunen and Oja, 2001).

This technique assumes that: (i) the data variables are linear mixtures of some unknown latent variables in an unknown mixing system. (ii) The subcomponents are non-Gaussian (thus uncorrelated) signals and statistically independent from each other. (iii) The ICA algorithm can only be applied when there are fewer sources than detectors, which means that it will fail when there are more sources than detectors (Hyvärinen, Karhunen and Oja, 2001; Stone, 2004).

In small invertebrates, ICA has been successfully applied and validated (Brown, Yamada and Sejnowski, 2001; Brown *et al.*, 2008; Frost *et al.*, 2010; Hill *et al.*, 2010) with relatively large sets of neurons (>100). However, ICA performs relatively poorly on small data sets (with a low number of neurons) due to insufficient information collected from each neuron presented in the data; for example, this happens when neurons are vertical to or stacked on top of each other (Brown, Yamada and Sejnowski, 2001). In essence, ICA does not have enough information about each neuron to be able to distinguish between individual neurons and from other signals such as noise.

In passing, it is worth noting that, whilst it is common in everyday language to take the word uncorrelated as meaning unrelated (and hence independent), this is not the case in statistical

analysis, particularly if the variables are non-linear. In statistical analysis, if two or more variables are independent they will also be uncorrelated, but the reverse is not generally true; see assumption (ii) above. Many non-linear relationships, an example is the quadratic function, can generate related (non-independent) variables that are uncorrelated. Conversely, if the variables have a Gaussian distribution (as in the case of most noise), then when they are uncorrelated they are also independent. An important observation is that most signals do not have a Gaussian distribution and, therefore, are not likely to be independent after they have been decorrelated using PCA. In fact, this is one of the main reasons why the resulting principal components are not usually meaningful variables. They are inherently mixtures of the underlying sources since the transformation is essentially a re-expression of the original data. This inability to make two signals independent through decorrelation provides the key motivation for the source separation technique of the ICA that seeks to uncover the so-called latent variables with greater meaning.

As with the PCA technique described in the preceding section, the potential use of the ICA technique to separate the signals generated by the individual neurons in the pyloric circuit is described further in section 4.5.

2.2.11. Template-Based Matching Approach

The template-based matching approach or, simply, template matching is one of the most well-known pattern matching techniques used in digital image processing to detect, recognise and localise objects based on an image template regardless of its orientation, scale and view from the image (Brunelli, 2009). As a high-level computer vision algorithm, the technique might require sampling a large number of points of the image, although it is possible to reduce the resolution of the search and template (2-D) images by the same factor and perform the search operation on resulting downsized images by repeated smoothing and subsampling (multiresolution or Pyramid image processing technique). This is achieved by providing a search window of data points inside the search

image in order that the template does not have to search for each possible data point in it and the combination of the two (Swaroop and Sharma, 2016).

For 1-D signal/data, the template-based approach relies on the (cross) correlation between the template or reference and target/signal, as it seeks to localise the position(s) where the target matches the reference template; see Figure 15, which presents a schematic view of this method. Here, the correlation operation measures the degree of similarity of the templates and the reference signal, with results (depicted as the output in Figure 15 (D) & (E)) of the cross-correlation reaching a maximum when the target image is aligned with the same features in the reference/template.

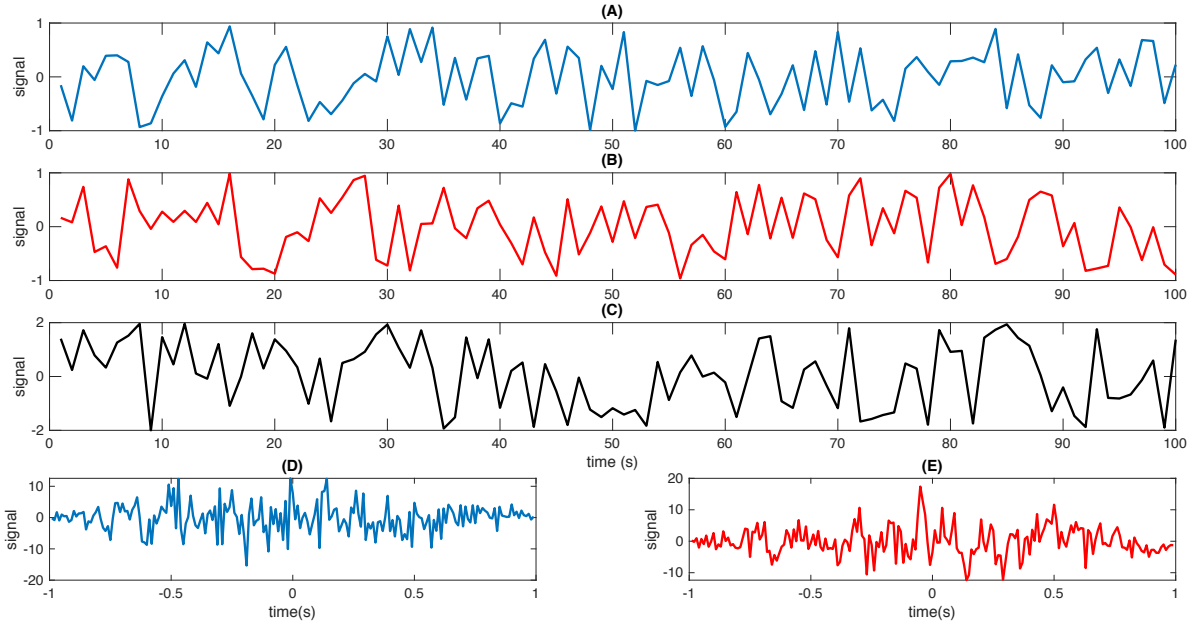

Figure 15 – Schematic view of the template-based approach. (A) Template 1, (B) template 2, (C) signal, (D) correlation between template 1 and signal and (E) correlation between template 2 and signal. The result in (E) suggests the highest similarity between template 2 and the target signal, with peak occurring after a relatively small lead time (≈ -0.04s) between the two signal waveforms.

The method described above has found applications in different areas of scientific endeavours including pattern recognition, electron tomography, cryptanalysis and perhaps more relevantly neurophysiology, among others (Brunelli and Poggio, 1993; Hulteen and Martin, 1997; Chi *et al.*, 2007; Murillo-Escobar *et al.*, 2015; Margarito *et al.*, 2016). Specifically, the template matching algorithm was studied, as one of the well-documented approaches to (neural) spike sorting

procedure, in the context of this work presented in section 4.5 on the identification of pyloric neuron activity using the VSD imaging technology.

2.3. Summary

The STNS and particularly the STG of the decapod crustaceans have been studied for some decades. The STG contains two central pattern generators, the gastric mill and the pyloric rhythm; they regulate sets of muscles that control the foregut. The gastric mill is a slow and intermittent rhythm (5 to 10s) while the pyloric rhythm is faster with an average of 1 to 2s, remains with spontaneous activity *in vitro* and has a characteristic triphasic rhythm identifiable in the extracellular recordings obtained from the lvn.

The VSDI technology has been used for around 50 years in a wide range of *in vivo* and *in vitro* preparations, using bath and injected dye application. In decapod crustaceans, it has allowed recording the entire STG network solving the space limitations produced by the intracellular recordings. To facilitate analysing the complex signals obtained, many signal processing techniques have been adopted in the work to achieve the ultimate goal to identify the individual neurons in the pyloric circuit. These include (but are not limited to) a number of basic signal processing concepts such as the DC, RH and SNR, etc. Such concepts were described as they were used as throughout the analysis of this thesis in quantifying the characteristics unique to each neuron. Additionally, the classical technique of power spectrum estimation is described as a visualisation tool to display the energy extracted; specifically, it is used to localise the pyloric rhythm frequency within the spectrum, as well as to visualise how clear/noisy is the data. All these methods have led to a detailed description of wavelet analysis, specifically, the CTW and Morse wavelets, which offer a relatively modern (and important) signal processing methods, which have been widely used for time-frequency representation to facilitate analysis of the signals obtained in the experiments. In particular, the Morse wavelet offers a good time and frequency localisation, while the Morlet offers a superior

frequency localisation performance that enables greater insight into the characterising triphasic pattern of the pyloric rhythm recorded extracellularly on the lvn. Finally, the Hilbert transform is also described as important to estimate the instantaneous phase-shift between any two signals.

Importantly, the multiresolution technique of s-SSA to facilitate the time-frequency analysis was developed and described. Constructed using the basic Singular Spectrum Analysis (SSA) procedure, such a technique is instrumental to the detection of the pyloric rhythm, presented in chapter 3 (in section 3.3), in dye-bathed STG samples and, subsequently, enabling the deconstruction of the regular phasing of the pyloric activities recorded in the lvn as described in chapter 3. Specifically, as with the dye-bathed image/data, the SSA-based procedure removed much of the noise from the lvn whilst preserving the pyloric frequency selectively and, relevantly, its higher order harmonics. In contrast to traditional time series analysis, the SSA procedure provides a relatively easy-to-understand (and powerful) data-driven or model-free approach which makes few prior assumptions on the data; namely, SSA is constructed in four successive stages which are well documented as embedding, SVD, grouping and diagonal averaging. This allows the development of the sequential SSA (s-SSA), which involves repeated or cascaded applications of the procedure (with potentially different window length) to the residuals of the preceding SSA, as a multiresolution approach to address the potential problem of weak separability identified in the dye-bathed data.

To facilitate the identification of the individual neurons in the pyloric circuit, two multivariate statistical procedures were examined in the context of traditional spike sorting methods described later in chapter 4. Essentially, these procedures were developed for and concerned with the detection/classification of neural action potentials observed from these neurons. They include, firstly, the classical technique of PCA, which is commonly adopted to reduce the dimension of a dataset, by removing the inherent/potential correlation of the variables. Additionally, the ICA is also presented as the advanced computational method that is widely known to be effective in separating linearly mixed and independent sources, particularly when both the mixture and the system are unknown. Finally, to enable matching and localising specific neural spike/waveform that is

characteristic of the individual pyloric neuron, the general approach of template matching was described. The approach requires a reference model of the spike shape (or template) to be compared or aligned with the target spiking pattern unique to each of such neurons, by computing the respective cross-correlations whose results provide a similarity measure between the target waveform and specific reference template.

3. Pyloric Rhythm Extraction

This chapter is the first of a three-part test of concept that deals with developing a reliable signal processing procedure to extract the pyloric rhythm from the typically noisy voltage-sensitive dye imaging (VSDI) data captured from STG samples prepared in a dye bath setting. Specifically, it describes the construction of a multiresolution approach developed to separate from such noisy data the pyloric rhythm, based on the sequential Singular Spectrum Analysis (s-SSA), which was discussed in detail in section 2.2.8.

The organisation of this chapter is summarised as follows. Sections 3.1 includes an introduction on how VSDI by bath application overcomes space limitations of the traditional method of electrophysiological recordings used for small neural networks and, by contrast, description on how such limitations could be overcome using VSDI. Section 3.2 presents the experimental procedures that entail including sample preparations, data collection and, in no small part, its accompanying collation method. These are followed by section 3.3, which covers the overall method of data analysis including particularly advanced signal processing techniques that have led to the development of the multiresolution algorithm constructed using the s-SSA approach. The results, some of which were published in dos Santos, Andras and Lam (2017a), are presented and discussed in section 3.4, where details covering how the pyloric rhythm was extracted from the VSDI data are presented alongside a brief performance evaluation. A summary is presented in section 3.5.

3.1. Introduction

Intracellular recording using sharp electrodes can be performed in multiple neurons on the stomatogastric ganglion (STG), to facilitate an understanding (in great detail) of individual neurons, the connections between neurons or more in-depth knowledge of a small network (Brette and Destexhe, 2012). However, due to space constraints, no more than eight neurons (Miller, 1987;

Faumont *et al.*, 2005; Selverston and Rabinovich, 2009) can be recorded simultaneously in the STG, with few exceptions (Heinzel and Selverston, 1988). The technology of voltage-sensitive dye imaging (VSDI), which records all neurons in the field of view of the optical imaging equipment, addresses this important shortcoming and has become in recent years the chosen method to achieve a large-scale view of the neuronal network (Hill, Bruno and Frost, 2014; Frost and Wu, 2015). Indeed, the technology has been successfully used in the STNS of decapod crustaceans; mostly in the STG but not exclusively (Stein and Andras, 2010; Stein, Städele and Andras, 2011; Städele, Andras and Stein, 2012; Preuss and Stein, 2013; Goldsmith, Städele and Stein, 2014; Steyn and Andras, 2016; Follmann, Goldsmith and Stein, 2017).

Biologically, the STG of the brown crab is the smallest neural circuit and consists of 26 neurons organised in a planar structure (see section 2.1.2). As such, it is possible to record the entire network using electrophysiology or, more relevantly, VSDI in one single field of view with a 20x objective, offering a promising means to investigate multi-neuron dynamics and the emergence of network scale functionality in neural systems.

Technically, the VSD is designed for either a bath or injected dye application. In terms of performance, it has been established (Stein, Städele and Andras, 2011) that injected dye technique could achieve better results than bath loaded in signal-to-noise ratio (SNR) terms. However, the technique requires a long time for application since each neuron takes 20–30 min to load (see Table 1 in section 2.1.5), added with the risk of having to 'poke' the cells with sharp electrodes multiple times that might lead to rhythm disturbance due to the death of affected cells, or even kill the preparation (network). For these reasons, the technique is impractical to load every single cell if there is the desire to record the entire neuronal circuit and not just a few neurons. Bath application, on the other hand, requires 20-30min to diffuse through the entire STG sample. Consequently, the choice between these techniques (bath and injection) is a trade-off between time/risks and signal quality; both have considerable impacts on the SNR of the resulting signals. For this thesis, dye bath application was the method chosen given the practicality of time (as it would take too long to load

the dye by injection) and, importantly, the added risk of killing the preparation while loading all cells with dye.

Previous studies using VSDI adopted a so-called *event-triggered time averaging* procedure (Städele, Andras and Stein, 2012; Bai *et al.*, 2014; Steyn and Andras, 2016) to model pyloric (PY) neurons, by applying a fixed averaging sliding window over the respective pyloric cycles manually identified from the optical data. This was implemented in Microsoft Excel (2010, 2013) in conjunction with its plotting tools. In terms of reproduction of the work, such a method was tedious, laborious and error prone. Technically, however, such a low-pass filtering technique not only removed noise and small-scale fluctuations in the data, but it also smoothed sharp changes in the signal that might be of importance in characterising the different neuronal types, (thus) making the exact identification more difficult (dos Santos, Andras and Lam, 2017a). From a signal-processing viewpoint, more importantly, the allied moving average (MA) technique (Hayes, 1996) adopted in an attempt to smooth the optically recorded data imposes significant limitations on the modelled spectrum of the pyloric rhythm, which is known to contain sharp peaks; see further discussions in section 5.2.2. The work presented here seeks to develop a more accurate method to extract the pyloric rhythm neurons without the need for averaging.

The pyloric rhythm is one of the two central pattern generators in the STG of the decapod crustaceans, which controls the pylorus, filtering the food particles resultant from the gastric mill (chewing process) (see section 2.1.4). The rhythm is characterised by a continuous repetitive triphasic pattern with a typical frequency of 1-2Hz; a detailed description was presented in section 2.1.4. As explained in section 2.1.5 the VSD chosen is the di-4-ANEPPS, which exhibits a uniform 2-10% fluorescence change per 100mV (Loew, 2010; ThermoFisher, 2018). To note here, as explained in section 2.1.2, the neuropil is a bundle of neurites dominated by pyloric rhythm, which can be recorded in the same ways as any other cell in STG. As such, the frequency estimated from the neuropil is used as a reference for the pyloric rhythm.

The multiresolution approach developed in this chapter is based on the SSA method (explained in section 2.2.8) which is a powerful tool in time series analysis; it combines elements of classical time series analysis, multivariate statistics, multivariate geometry, dynamical systems and signal processing (Golyandina, Nekrutkin and Zhigljavsky, 2001; Golyandina and Zhigljavsky, 2013). SSA broadly consists of two complementary stages: decomposition and reconstruction; each of these stages includes two separate steps. The first stage is the decomposition of the original times series with embedding and singular-value decomposition (SVD); the second corresponds to the reconstructed series for (new) data points with grouping and diagonal averaging sub-steps. As the VSDI data has components that were weakly separable, a multiresolution approach constructed with the s-SSA was developed to analyse such data (dos Santos, Andras and Lam, 2017a). Essentially, the two-stage s-SSA procedure facilitated a cascaded application of the basic SSA algorithm whereby the first application extracts several time series components from the input signal with a specific window length L_1. This is followed by applying the SSA again to the results, or residual, of the first application using a potentially different window length L_2. The computational model including the selection of the window length was covered in section 2.2.8.

3.2. Experimental Protocol Including Methods and Materials

3.2.1. *Cancer pagurus* Maintenance and Solutions

Live adult *C. pagurus* were obtained from Hodgkinson Fresh Fish, Manchester, bought in 10kg boxes, which contained 12 to 18 crabs. The crabs were kept alive in artificial seawater tanks (red sea salt, Red Sea) in the laboratory, with a water temperature of 12-14°C with a 12h light-dark cycle (Heinzel, Weimann and Marder, 1993; Goeritz *et al.* 2013). Maintenance of the live animals and experiments were carried out in accordance with the European Communities Council Directive of 24th November 1986 (86/609/EEC), with ethical guidelines applied by Keele University and supervised by the local veterinary.

A cold saline crab solution was used during dissection and experiments to maintain alive the nervous system as close as possible to optimal living conditions and temperature (11-13°C) (Städele, Andras and Stein, 2012); this saline was also used to keep clean the preparation throughout the dissection process and to wash out the dye excess after its application. This solution was prepared in 5L containers and kept in the fridge at 5°C; it consists of a mix of different salts diluted in purified water at 15MΩ (Elga DV25, PURELAB Option, Berlin, Germany). Table 2 has the salts and respective weights to prepare such a solution; all salts were acquired from Sigma-Aldrich (Darmstadt, Germany). The pH of this solution must be between 7.4-7.6 after mixing the salts prior to chilling; if pH was higher than 7.8 or lower than 7.2 the solution was discarded otherwise pH was corrected with Trizma Base or Maleic acid to reach the desirable range.

Table 2 – Cancer pagurus saline solution salts concentration and weights.

Salt	Concentration mM	g / 1 Litre	g / 2 Litre	g / 5 Litre
KCl	11.0	0.83	1.66	4.15
NaCl	440.0	25.8	51.6	129.0
$CaCl_2 2H_2O$	13.0	1.9	3.8	9.5
$MgCl_2 6H_2O$	26.0	5.3	10.6	26.5
Trizma Base	11.2	1.5	3.0	7.3
Maleic Acid	5.0	0.6	1.2	3.0

During the dissection process, the saline was changed every 20min while during experiments the solution was changed every 10-20min. Due to technical constraints, a continuous cooling saline flow (perfusion) during the experiment could not be set up. As a result, the saline had to be changed manually with a syringe. First, the old saline was removed, and then the fresh one was slowly injected. Aware of errors that this procedure might induce, for example, imaging shifting or rhythm disturbance, the saline was changed in the same way in all experiments so that if any error were induced it would be 'constant' throughout all the experiments. In addition, after the change of saline during the experiments, a period of 2 minutes was given to allow the preparation to rest and restore the rhythm from the stress caused by this manoeuvre before recording was started again.

3.2.2. Crab Dissection and Stomatogastric Nervous System (STNS) Extraction

On the day of the experiment, the animal was anaesthetised 20-30min (depending on animal size) prior to dissection, by being dipped in an ice bucket. Appendix 1 (Standard operating procedure) explains in detail the aesthetic protocol used in the laboratory. The dissection was divided into two different parts: the crude or gross dissection and the fine dissection. Gross and fine dissection protocols were followed by Gutierrez & Grashow (2009).

The first part of the dissection consists of the extraction of the brown crab's stomach, which is located in the frontal region of the cephalothorax; Figure 16 shows this region (yellow area).

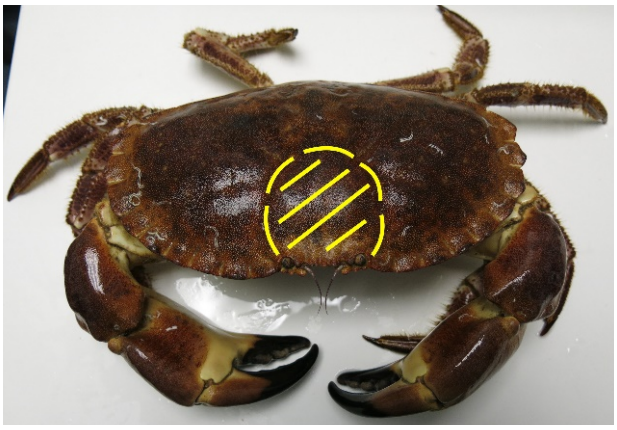

Figure 16 – C. pagurus cephalothorax region (yellow).

Then the legs were removed followed by the animal's carapace from the sides as Figure 17 displays. The mouthparts and the central part of the carapace (covering the cephalothorax) were last removed to allow the separation and extraction of the stomach from the meaty part of the animal. Figure 18 shows an extracted stomach filled with a saline solution. The final steps of the gross dissection were to cut open the stomach, remove the teeth and pin it to a black sylgard-coated dish, which was filled with fresh saline.

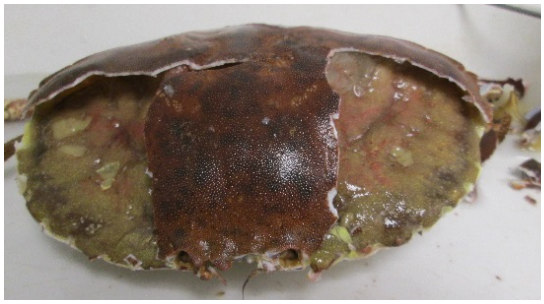

Figure 17 – Brown crab's gross dissection.

Figure 18 – Brown crab's stomach filled with saline.

The fine dissection is based on the extraction of the STNS from the stomach's wall, using the detailed protocol that starts with the removal of the epidermis and culminates with the desheating of the STG that allows intracellular recording, dye injection and improves dye bath diffusion. A picture from the fine dissection is shown in Figure 19; on the left is the stomach pinned to the black sylgard (partially dissected), while on the right is the STNS pinned to a clear silicone elastomer-lined (ELASTOSIL RT-601, Wacker, Munich, Germany) with the desheathed STG; some essential structures of the STNS are named in the picture.

Once the STNS was extracted from the crab's stomach, it was pinned down with fine wire pins and the STG into the clear silicone where the STG is desheathed.

Appendix 2 contains images showing the equipment/tools used to execute the *C. pagurus* dissection.

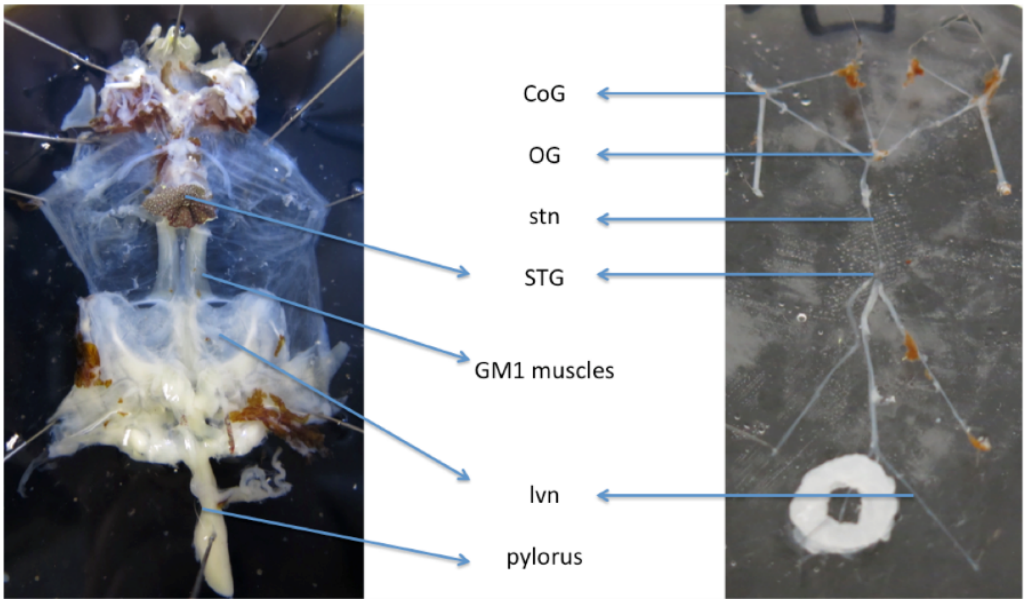

Figure 19 – Left: fine dissection of the brown crab's stomach. Right: stomatogastric nervous system (STNS) pinned in the clear sylgard, original size. CoG – Commissural ganglion, OG – Esophageal Ganglion, stn – stomatogastric nerve, STG – stomatogastric ganglion and lvn – lateral ventricular nerve.

3.2.3. Electrophysiology

The pyloric rhythm is widely known by the triphasic rhythm identified in the extracellular recordings from the lvn (analogue signal), as explained in section 2.1.4. This triphasic rhythm/signal was used as a frequency reference for the estimated power spectrum for the neuropil in the dye bath. Such recording was synchronised with VSD imaging equipment to corroborate the pyloric rhythm extraction from the optical data, as will become clear in section 3.4. The analogue signal was also used as a quick first visual aid to estimate the frequency of the pyloric rhythm, if present, extracted from the STG sample. Indeed, if the triphasic rhythm could not be identified, the preparation was discarded immediately as some cells in the sample might be damaged or even dead.

To generate the extracellular potential fields a petroleum jelly well was crafted around the lvn, one electro steel wire is placed inside the well while the other one penetrates into the gel near the well as a reference as Figure 20 demonstrates; the protocol was described by Gutierrez & Grashow (2009).

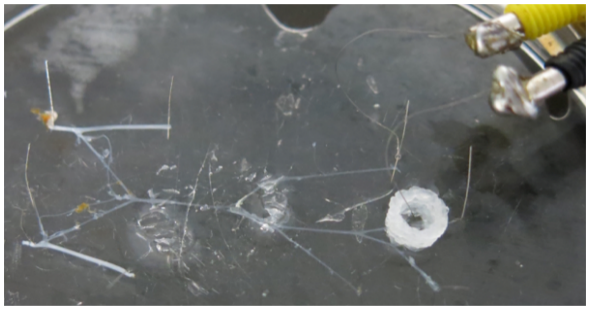

Figure 20 – Extracellular potential field crafted around on lvn.

The signal was recorded, filtered and amplified by an AC differential amplifier (A-M Systems model 1700, Sequim WA, USA) passed to a CED MICRO 1401 (Cambridge Electronic Design, Cambridge, UK) data acquisition box and read using Spike2 v8.07 (Cambridge Electronic Design, Cambridge, UK).

3.2.4. Imaging

As described in section 2.1.5, the dye used for bath application imaging is the di-4-ANEPPS. Figure 21 shows an image of the STG dyed with a filter through the microscope.

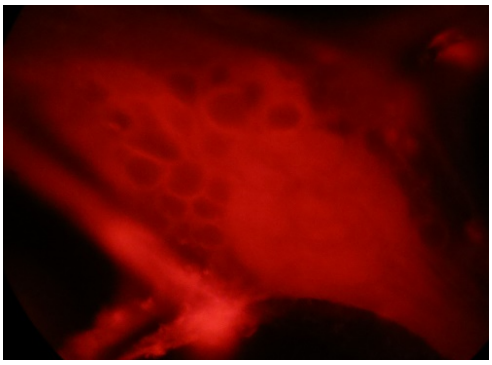

Figure 21 – Di-4-ANEPPS bath application under the microscope eyepiece.

The imaging was recorded using the MiCAM02 imaging system (SciMedia Ltd., Tokyo, Japan), analysed and stored with Brain Vision Ana (BV-Ana) software, version 11.01 (SciMedia Ltd., Costa Mesa, CA, USA). The camera was connected to an upright fluorescence microscope (BX51WI, Olympus Corporation, Tokyo, Japan) that was equipped with a 20x-mounted objective (XLUMPLFL20xW, N.A. 0.95, WD 2.0mm; Olympus Corporation, Tokyo, Japan). A wide green excitation filter was used (480–550nm, MSWG2, Olympus Corp., Tokyo, Japan). The lighting was

delivered from a 150W halogen light source (HL-151, Moritex Corporation, Tokyo, Japan) with a computer-controlled shutter; the light intensity was adjusted manually to minimise potential phototoxic damage.

The microscope was standing on a CleanBench™ vibration isolation table (TMC Vibration Control, Peabody, MA, USA) equipped with a Faraday cage to isolate from other electrical sources. This was covered with one layer of blackout fabric and another layer on top of standard thick cotton fabric, to further reduce light exposure as the room cannot do a complete blackout.

Before initiating the recordings, a high-resolution (192x128 pixels) image was taken to help identify the individual cells within the field of view of the microscope from a series of low-resolution (48x32 pixels) co-registered images recorded over the duration of a recording. These low-resolution images form a (3-D) image stack, which provides a sequence of 21,840 images sampled over the course of a recording, offering a temporal resolution of 1.5ms (sampling rate), and resulting in a total length of 32.67s.

The dye was applied in the isolated STG by a petroleum jelly-well of approximately 1cm diameter, the saline that remained inside of the well was removed by a syringe, and then 20µl of ready di-4-ANEPPS was inserted into the well. The dye was acquired in a bottle of 5mg (Thermo Fisher Scientific, UK) and prepared as a stock solution; 5mg di-4-ANEPPS were dissolved in 1 ml Pluronic F-127 (20% solution in DO – dimethyl sulfoxide, Invitrogen, Paisley, UK) and kept in a screw top tube cover with foil stored away from light source, at room temperature. On the day of the experiment, 10µl of the stock solution was mixed with 500µl of crab saline solution, using a Vortex Mixer MX-S (Camlab, Cambridge, UK) for 5min.

The dyed preparation was then left in the fridge for approximately 25 minutes. This allows the dye being diffused and absorbed by the STG while, it maintains a cold temperature and isolates the preparation from room light exposure. After 25 minutes, the petroleum jelly well around the STG was removed, and the dye was washed out using a saline flow. The petri dish was then filled with fresh saline solution.

3.2.5. Data Collection

The 3-D image stack was collected and stored (described in section 3.2.4) and subsequently analysed in the BV-Ana software (SciMedia Ltd., Tokyo, Japan), exported into CSV (comma-separated values) formatted spreadsheets to be analysed in MATLAB® (MathWorks, Natick, MA, USA).

First, in BV-Ana, the high-resolution (2-D) image of the STG is organised in a different region of interest (ROI) that maps each cell, with bundles of pixels to represent each of the ROIs as shown in Figure 22A. These bundles of pixels were then individually mapped to the corresponding pixels in the (low-resolution) image stack; each pixel value was extracted in the form of 1-D time/signal sequences from successive images of the 3-D stack (Figure 22B).

As mentioned in section 2.1.2, the neuropil is also treated as a cell, selecting the correspondent pixels forming its ROI. The number of pixels extracted from each cell varies depending on the size and the visibly of each cell/neuron; the neurons had a pixel representation between 8 to 35 pixels, while the neuropil had between 40 to 80 pixels.

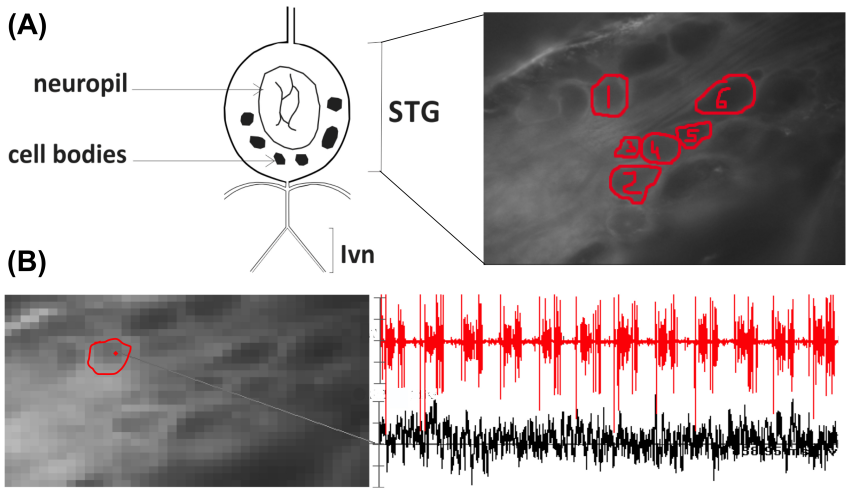

Figure 22 – (A) On the left a schematic figure of the STG and on the right a high-resolution image with the organisation of different ROI/cells. (B) On the left the low-resolution image (3-D image stack) corresponding to the high-resolution image, on the right in red is the analogue (lvn) recording; in black is the signal for one pixel of the cell (ROI) 1.

A key to the work is to map the STG neuron activity (the pyloric rhythm neurons) optically recorded, as changes in fluorescence over time by bath dye application, with the extracellular

captured triphasic pyloric motor pattern on the lvn, thus allowing the identification for the neuron type (pyloric or gastric) for each ROI.

3.3. Signal and Data Analysis

As described in section 2.1.2, the STG consists of two types of neurons – pyloric and gastric; each has its firing rate, around 1-2Hz and 0.05-0.2Hz respectively (Marder and Bucher, 2007). In this thesis, these neurons were dyed using bath application and imaged optically with a high-speed camera. The latter enables individual neurons, or ROIs captured in the field of view to be analysed, with the goal to determine the presence or absence of the pyloric rhythm extracted from each ROI including the ROI that represents the neuropil. As discussed in section 2.1.2, the main frequency extracted from the neuropil (bundle of neurites) is known to be dominated by the pyloric rhythm, which was used as a reference in the subsequent analysis.

The main challenge in analysing the data is the relatively poor SNR (~-20dB – see section 2.2.7) achieved by the VSD; as explained in section 2.1.5, the dye typically captures a maximum of 10% signal changes. Figure 23(A) shows an example of a segment of the raw data signal (blue) obtained from the dye bath with the extracted pyloric rhythm (red) overlaid on the top. Here, it is worth noting that the SNR achieved throughout this thesis was relatively poor.

Figure 23(B) reveals several notable features of the collated time sequences for the individual cell. First, the power spectrum was often dominated by some slow varying trends, which in this case is represented by a frequency of 0.06Hz as depicted in Figure 23(B). This suggests that it could correspond to an underlying gastric mill for which the typical activity frequency range is 0.05 – 0.2Hz. The latter is readily observable in Figure 23(A), where the mean-shifted sequence slightly fluctuates during the recording. Second, between 0-5.5Hz, there were other bandlimited noise processes, which seemed unrelated to the present pyloric rhythm, in addition to other highly correlated sinusoidal

components. Third, as evident in Figure 23(C), uncorrelated white noise was also present and covered almost the entire power spectrum (0 to 333Hz) beyond the 0-5.5Hz range.

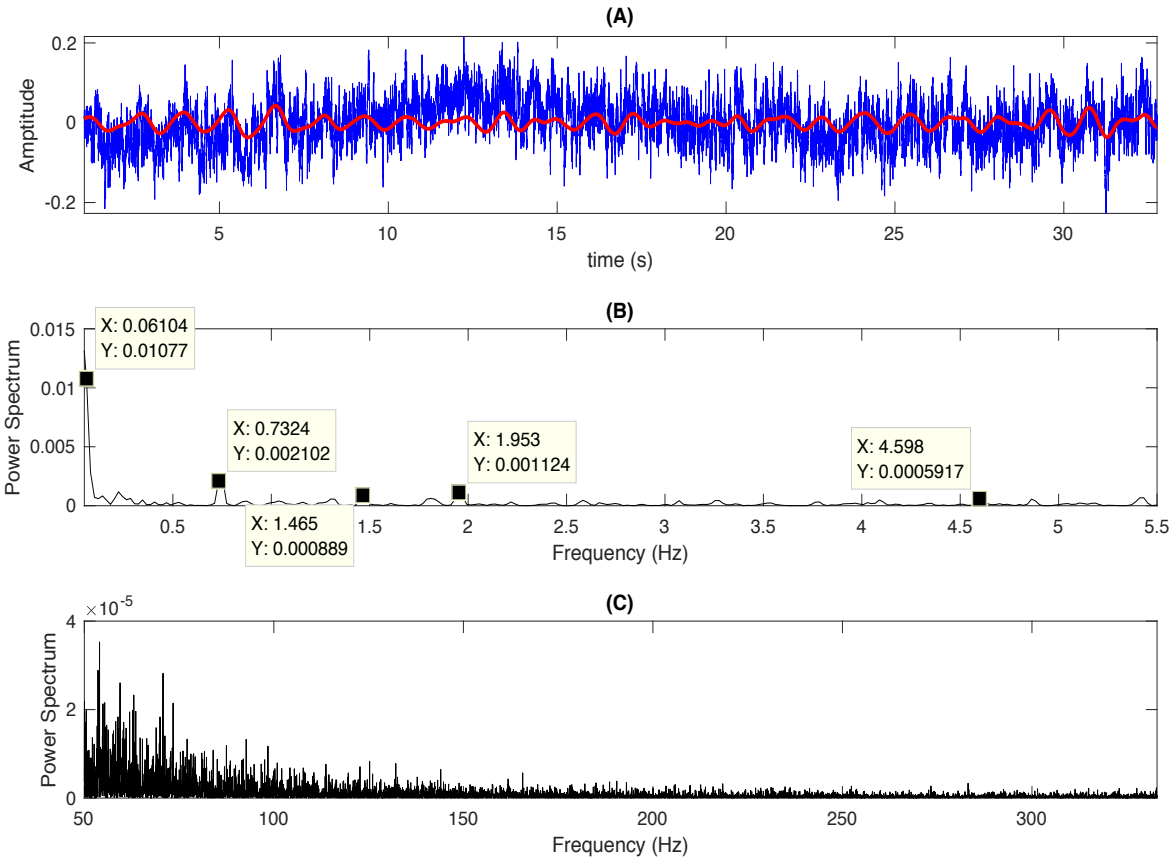

Figure 23 – (A) The time sequence shown in blue represents the mean-shifted signal (as an ensemble average) obtained from cell 3, overlaid with the extracted pyloric rhythm (in red). (B) The power spectrum computed between 0-5.5Hz for the time sequence depicted in (A). (C) As (B,) with the complete power spectrum (0-333.33Hz) displayed.

3.3.1. Earlier work

Earlier work on using VSDI to model neurons in the STG (Stein and Andras, 2010; Stein, Städele and Andras, 2011; Städele, Andras and Stein, 2012; Goldsmith, Städele and Stein, 2014; Steyn and Andras, 2016) have adopted the simple method of *event-triggered time averaging* to study the data, was specifically directed to model the pyloric (PY) neurons for each recording. Such a method has two major limitations, however. First, a de-trending averaging procedure had to be performed over

individual phases of the pyloric rhythm. This facilitated associating the still to be identified PR from the respective neuron (as ground truth) that is still largely unknown. As a result, additional steps such as intracellular recordings of the STG sample were required that might render the event-triggering based method somewhat inadequate, if not inappropriate, as the important advantages of the bath application of VSDs are significantly diminished; see earlier discussions in section 3.1. From the perspectives of this research/work, the need for such extra steps to identify the ground truth renders the event-triggering based method somewhat inadequate, if not inappropriate. Second, and relatedly, the event-triggered averaging procedure requires an extracellular recording to be used in order to determine the beginning of each phase. Such a task can be most challenging from a signal-processing perspective, as the spike trains of the pyloric rythm readily observable on the lvn must be decoded in order that its three characterising phases can be separated. Indeed, the complexity of this task is compounded by the generally unknown time lag between the optical image (camera recording of the STG) and the analogue recording captured on the lvn due to the variable delay of the axonal; see sections 4.1 and 4.6 in Chapter 4 for further discussions. In Steyn and Andras (2016), indeed, the identification of these phases has to be done by visually examining the trace and manually noting the time stamp of the first spike in a phase of each cycle with reference to the accompanying extracellular/lvn recording.

In passing, to help correlate the signals obtained from both recordings as described above, the technique of *Short-time Fourier transform* (STFT), a linear time-frequency analysis method closely allied to the CWT techniques as described in section 2.2.4 was also tested. In addition to the well-documented shortcomings of such a relatively simple time-frequency analysis, most notably the truncated (moving) time/data windows and the accompanying sidelobe problems in the resulting frequency spectra (described further in sections 5.2.1 and 5.2.2), the technique is inadequate to analyse the inherently high-frequency lvn recordings; see section 4.1 and the alternative methods described in 4.5.

Lastly, the recording software (BV-Ana) as described in section 3.2.5 had also been tested in an attempt to identify the pyloric neurons using a number of averaging procedures applied to the pixels selected for each ROI. As described earlier (section 3.1), however, this was shown to be far from adequate due to the typically poor SNR achieved in our experiments. Furthermore, such a manually operated procedure lacks accuracy, precision and perhaps importantly, generality, which makes its automation almost impossible.

3.3.2. A multi-resolution approach of the sequential SSA (s-SSA)

To address the above, methods such as the SVD or eigenvalue decomposition are generally known to provide good resolution and frequency estimation characteristics (see section 5.2) (Tufts and Kumaresan, 1982). Such an orthogonal decomposition approach is particularly useful in separating highly correlated signal components (for example sinusoidal or exponential), or other narrowband processes that are uncorrelated with white noise. However, these methods on their own could be ineffective in separating broadband processes from such noise, which is generally unstructured. As a result, the multiresolution procedure of the s-SSA, described in section 2.2.8, was developed.

As described in 2.2.8, the nonparametric technique of the SSA makes no prior assumptions about the data and, as such, explains its versatility across many subject domains. In particular, the SSA algorithm can be viewed as two main complementary steps each divided into sub-steps. Qualitatively, the first two stages concern the orthogonal and energy-preserving decomposition of a time/signal series (McClellan, Schafer and Yoder, 2016), and the last two stages reconstruct the original signal using a diagonal averaging process that provides an in-built low-pass filtering capability which is simple and effective.

To facilitate extracting the pyloric rhythm in a noisy environment, the multiresolution approach based on the sequential Singular Spectrum Analysis (s-SSA) was adopted (dos Santos, Andras and Lam, 2017a). Broadly speaking, the approach of the s-SSA was constructed to separate the pyloric rhythm from the optical image sequence that has shown to display a more complex form. Such a

procedure was devised specifically to aid resolve the mixing problem of signal components within the collated time sequences from each ROI or, formally, the problem of close singular values for weakly separate sequence components (Golyandina, Nekrutkin and Zhigljavsky, 2001; Golyandina and Zhigljavsky, 2013). Specifically, the two-stage s-SSA procedure was first applied to the time sequences collated from the neuropil. The reasons are two-fold; firstly, the neuropil, described in section 2.1.2 as a synaptically dense region in the nervous system composed of neurites, is known to be dominated by the pyloric rhythm in the STG. As such, it provides a reference or ground truth to compare with the extracted signal components from each cell. Secondly, studying the power spectrum helped determine features in the parameters used with the s-SSA; namely, the choice of the initial window width (*L*). This is calculated in equation (26) as follows: Given the pyloric frequency (PR) as shown in the power spectrum is 0.7324Hz and sampling rate R of 1.5ms, the minimum suitable window width L_{min}, measured in the time domain as a number of sampling frames, can be calculated as (Golyandina et al. 2001):

$$L_{min} = \frac{1/_{PR}}{R} = \frac{1/_{0.7324}}{1.5 * 10^{-3}} = 910 \quad (26)$$

The pyloric frequency extraction (0.7324Hz) and noise reduction during the different stages of the s-SSA are illustrated in the power spectra shown in Figure 24 (A-C).

In passing, it should be noted that the selected pyloric frequency was based on a corroborative (manual) study of the analogue signal captured on the lvn, where approximately 24 completed cycles were observed. Equivalently, given a sampling rate of 1.5ms and the 32.76 seconds (= 21840 samples * 1.5 ms) duration of a complete recording, this corresponds to a pyloric frequency of approximately 0.7326Hz; that is, 24 cycles / 32.76 seconds.

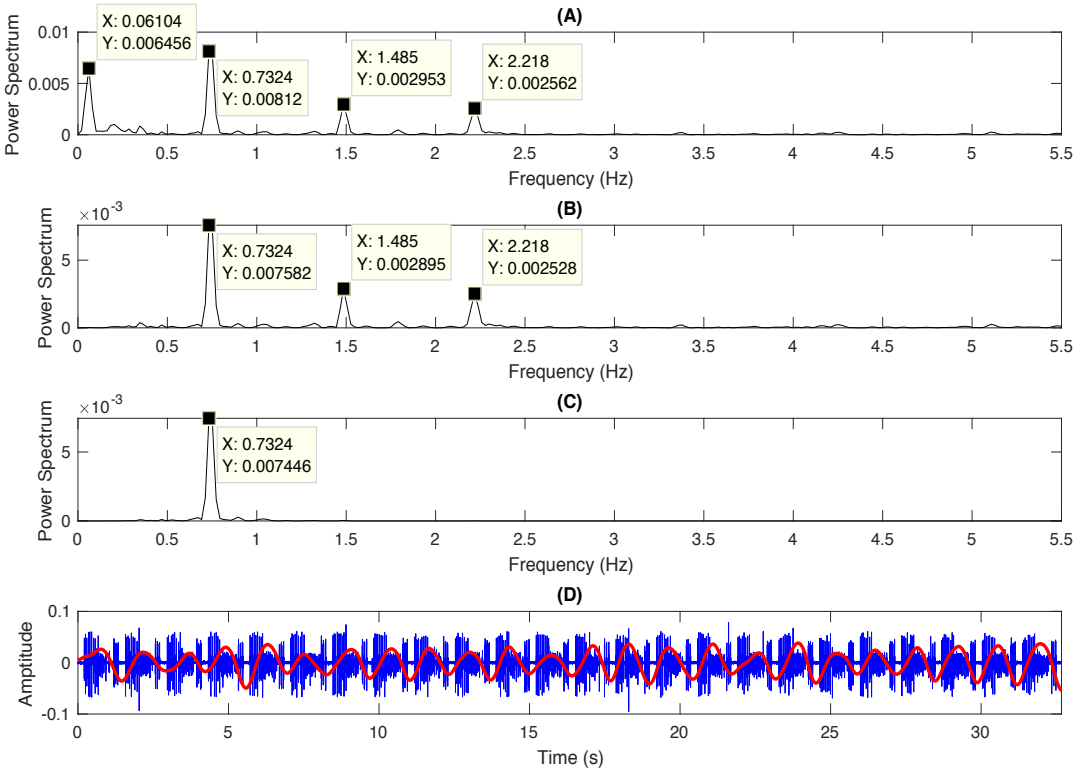

Figure 24 – (A-C) Power spectrum from the neuropil. (A) raw data, (B) first stage s-SSA with window length 1000, (C) second stage s-SSA with window length 1250. (D) The analogue signal (blue) overlaid with frequency extracted for the neuropil (0.7324Hz) shown in red.

From equation (26), the (first) window length L_1 was set at 1000 for the first stage of the s-SSA procedure, and the resulting power spectrum is shown in Figure 24(B). Here, it is noted that the slow varying trend at a frequency peak at 0.06Hz and the other low-frequency noise that was present previously in the neighbourhoods leading up to the pyloric rhythm were completely removed by this first s-SSA stage.

To afford a higher spectral resolution to the second stage of the s-SSA, the window length (L_2) was increased to 1250. The resulting power spectrum of the computed pyloric rhythm is depicted in Figure 24(C), where the pyloric rhythm was located accurately (at the pyloric frequency of 0.7324 Hz) and was practically free of noise. The analogue signal recorded from the lvn (blue) is included in Figure 24(D), to help compare with and validate the extracted pyloric rhythm (red) – 0.7324Hz.

Following selection of the window length (L) for each stage of the s-SSA, the grouping (the third stage of the SSA) and subsequently combination of the components were guided by the so-called

scree-plot, which displays the non-decreasingly ordered eigenvalues, which are obtained as part of the SVD procedure. In essence, the scree-plot is used to facilitate determining the number of signal components to be retained (or discarded), by plotting the eigenvalues (σ^2) against their corresponding orders/indexes (*k*). A common practice to facilitate the selection of component groups is by examining the plot and looking for 'elbows' – places where the curve (σ^2 vs *k*) levels off and becomes almost 'flat'. Alternatively, a relatively simple algorithm can be devised to evaluate the slopes of the lines by connecting adjacent points on the curve and determining *k* where the levelling off such slopes occurs. This is illustrated in Figure 25, where (A) shows the scree-plot (displayed in blue) generated in the first stage of the s-SSA, with window length (L_1) set to 1000, shown alongside the percentage variance (displayed in orange) accrued by the individual components up to and including the index/order (*k*). Similarly, Figure 25(B) shows the scree-plot of the second stage of the s-SSA (L_2 = 1250), which is performed on the residual of the first stage s-SSA from which signal/components whose frequencies were below the pyloric rhythm (0.7324Hz) were removed.

In passing, Figure 25(A) shows that the first 25 components (2.5% of the total number of components) account for over 80% (82.37%) of the variances, or total energy, of the input signal while the first two largest components are responsible for over one-third (34.13%) of the variance or signal energy contained in the data. At the other end of the spectrum, by contrast, less than a third of the total signal/data variance is distributed evenly over a much wider range of components where k = [10, 1000]. While Figure 25(B) shows that the sum of the first three components, which accounts for over 70% (71.27%) of the total input energy, corresponds to the individual signal components responsible for the extracted pyloric rhythm.

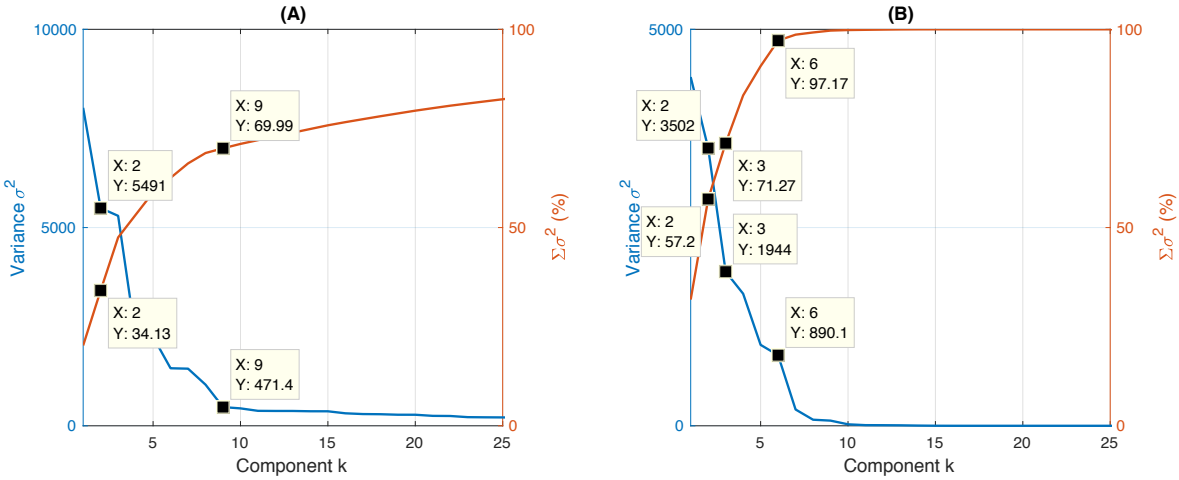

Figure 25 – Scree-plots from the neuropil. (A) Represents the first stage s-SSA, and (B) second stage s-SSA.

To illustrate the above, Figure 26 includes the individually computed periodograms that demonstrates the differences in noise captured in the optical recording of four different neurons/ROI (1, 10, 11 & 14), while Figure 27 shows the results obtained for the same neurons after the application of the two-stage s-SSA algorithm described here.

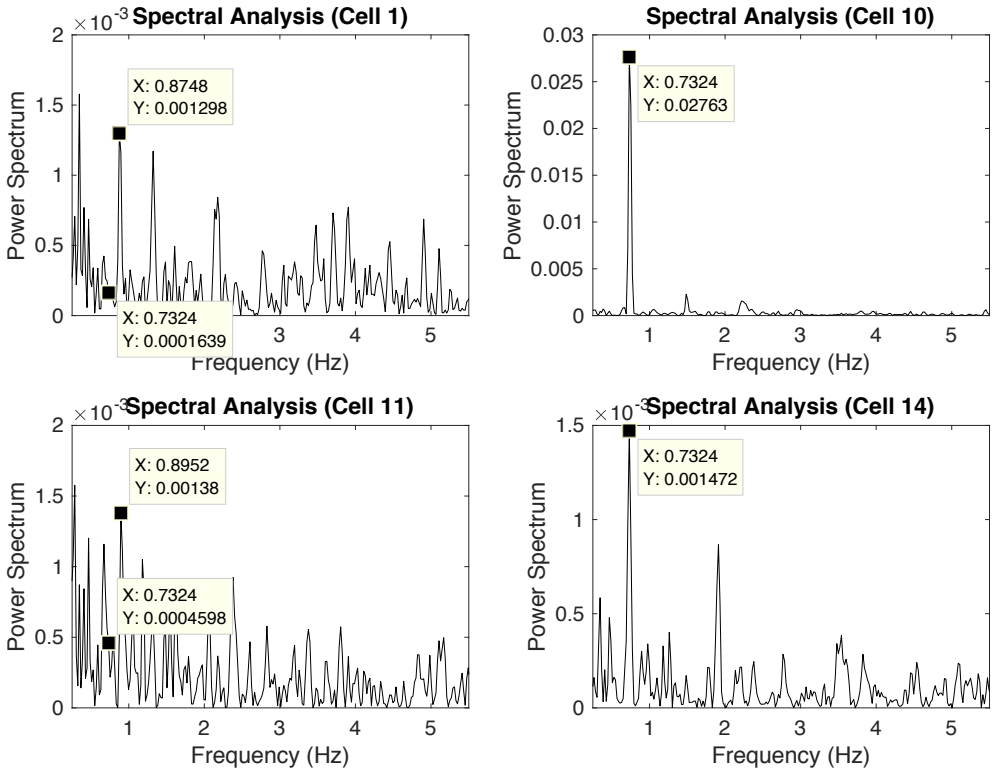

Figure 26 – Power spectrum of four neurons (1, 10, 11 & 14) in raw data.

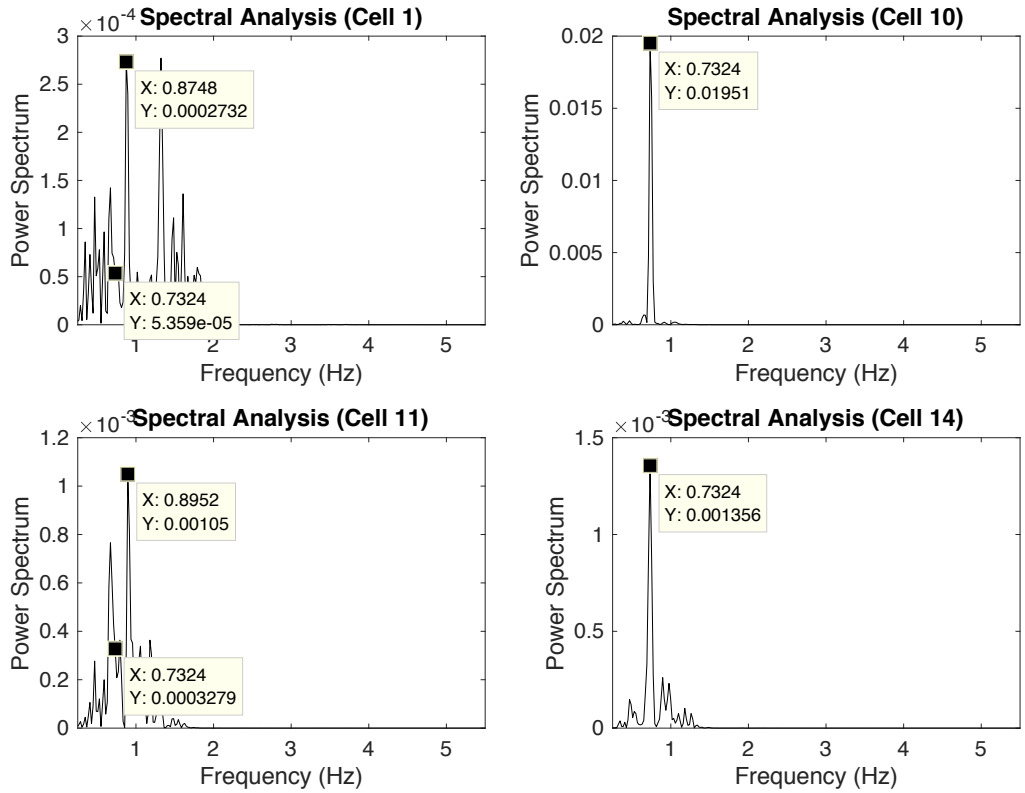

Figure 27 – Power spectrum of four neurons (1, 10, 11 & 14) after the multiresolution method was applied.

As a final note, the exceptional capability of the s-SSA to reduce or even remove broadband noises and undesirable narrow-band signals at frequencies located in the neighbourhood of the pyloric frequency is apparent in cells 1, 11 and 14. In particular, cells 1 and 11, both being examples of non-pyloric neurons, have significantly reduced the dominant signal component at frequencies 0.8749Hz and 0.8752Hz respectively that are close to the pyloric frequency (0.7324 Hz), following the two-stage s-SSA procedure. In the case of cell 11, a pyloric cell, this effect is even more apparent.

3.4. Results and Discussions

Using the same dataset as demonstrated in the preceding section, the results obtained by VSDI from the neurons/ROI were compared with pyloric rhythm extracted from the neuropil. In addition, the computed pyloric frequency was further corroborated by the separate evaluation performed on the analogue signal using visual inspection and manual segmentation of the signal captured on the lvn. Essentially, the triphasic pyloric cycle was carefully studied, with the goal to identify the PD-

timed, LP-timed and PY-timed pyloric activities displayed in an approximately 24 (manually counted) pyloric cycles over the complete course of the recording that lasted 32.76 seconds (or, equivalently, 21,840 samples). This is illustrated in the example MATLAB code snippet shown below:

```
fSam = 1/(1.5e-3);   % sampling frequency = 1/sampling period
SeqLen = 21840;      % length/total number of samples in each
                     recording
EstNCY = 24;         % by manual counting the number of pyloric
                     cycles in recording
EstFreq = 1/(SeqLen/EstNCY * (1/fSam));       % = 0.7362Hz
```

Here, it should be noted that the sampling frequency, `fSam`, was calculated using a sampling rate of 1.5ms, giving a sequence length (`SeqLen`) that represents the total number of sample frames per recording (lasting 32.67 seconds). The estimated number of cycles (`EstNCY`) is the completed cycles that can be observed (by visual inspection) on the analogue (lvn) signal and, therefore, the resulting estimated frequency (`EstFreq`) for the analogue recording calculated at approximately 0.7362Hz; see the last statement of the MATLAB code extract above.

The two-stage s-SSA procedure was tested using the aforementioned dataset as follows. Sixteen ROIs corresponding to cells 1 to cells 16 were identified in the field-of-view, in addition to the neuropil which was labelled as ROI/cell 17. Table 3 summarises the results obtained, with the relevant characteristics computed included. The decision (Y/N) of a simple classification based on the presence (Y=yes) or absence (N=no) of pyloric rhythm for the individual ROI is also displayed, with highlighted (grey) rows where the pyloric rhythm was identified.

As described, the pyloric frequency, estimated from the power spectrum for the neuropil as 0.7324Hz, was used as the reference against which the resulting power spectra, obtained following the application of the two-stage s-SSA algorithm to the individual cells/ROIs, were compared. This enabled the identification of five potential pyloric cells (5, 6, 10, 13 & 14) – each has the pyloric frequency shown as its first dominant frequency in the computed spectrum. The cells 2, 3, 7 & 15 also showed to contain a dominant frequency of 0.7528Hz, which is in close proximity of the pyloric frequency at 0.7324Hz. In fact, a closer examination of the corresponding spectra for some of these

cells also revealed that the pyloric frequency was also present, though as the second dominant frequency. This is illustrated in cell/ROI 3, in particular, the pyloric frequency was also present as the second dominant frequency in Figure 28(A), where the raw spectra are displayed. The resulting spectra obtained following the successive application of the two-stage s-SSA algorithm are also depicted respectively in Figure 28(B) and Figure 28(C), where the presence of the pyloric frequency in each case is clearly demonstrated. For this reason, it was concluded that cells 2, 3, 7 & 15 were also potential pyloric neurons.

Table 3 – Test of 2-stage s-SSA method results. Fq – highest frequency peak, SNR – signal-to-noise ratio and PR – pyloric rhythm. Cell 17 corresponds to a region of interest for the neuropil.

CELL number	Original		s-SSA separation		% Separation	SNR (dB)	PR (Y/N)
	Fq (Hz)	Amplitude	Fq (Hz)	Amplitude			
1	0.8748	0.001298	0.8748	0.000273	21	-22	N
2	0.7528	0.002280	0.7528	0.002386	85	-17	Y
3	0.7528	0.002280	0.7528	0.001996	88	-19	Y
4	0.8748	0.000724	1.6070	0.000327	45	-23	N
5	0.7324	0.009484	0.7324	0.009219	97	-12	Y
6	0.7324	0.000716	0.7324	0.000660	92	-22	Y
7	0.7528	0.001771	0.7528	0.001701	96	-20	Y
8	2.7060	0.001231	1.6680	0.000425	34	-22	N
9	0.8952	0.000806	0.8952	0.000601	75	-22	N
10	0.7324	0.02247	0.7324	0.019510	87	-14	Y
11	0.8952	0.001380	0.8952	0.001050	76	-22	N
12	0.8952	0.002250	0.8952	0.001470	65	-20	N
13	0.7324	0.006267	0.7324	0.006103	97	-15	Y
14	0.7324	0.001472	0.7324	0.001356	92	-19	Y
15	0.7528	0.007351	0.7528	0.007045	96	-12	Y
16	1.0580	0.001790	0.8952	0.001561	87	-21	N
17	0.7324	0.000758	0.7324	0.007446	91	-10	Y

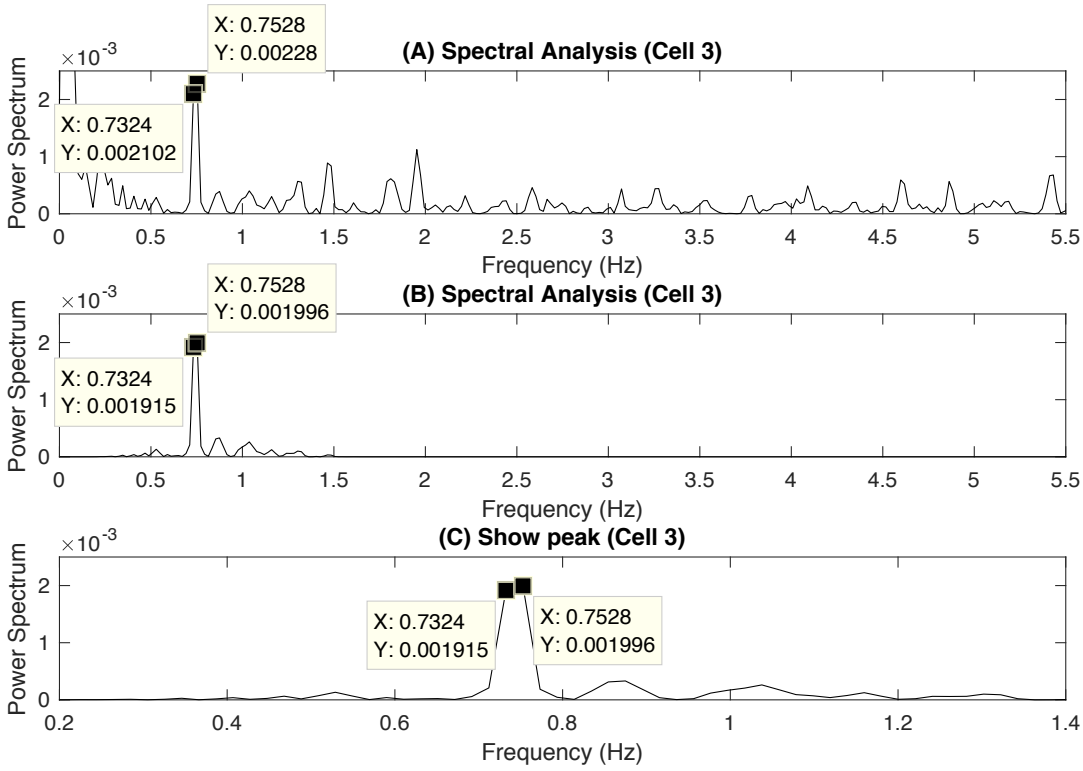

Figure 28 – Spectral analysis of cell number 3, (A) in raw data, (B) after applying s-SSA. (C) shows the close relationship between 0.7324Hz (pyloric frequency) and 0.7528Hz.

As highlighted in Table 3, the total number of the nine cells (labelled as ROIs 2, 3, 5-7, 10, 13-15), which were identified as potential pyloric neurons appeared to be reasonable. This is due to the fact that the total number of neurons known to be responsible for the pyloric rhythm is 11; namely, 1 AB, 1 LP, 1 VD, 1 IC, 5 PY and 2 PD neurons (see section 2.1.4), among the total of 26 neurons in the STG sample (Nusbaum and Beenhakker, 2002; Marder and Bucher, 2007; Derby and Thiel, 2014). In addition, it should also be noted that the percentage of separation (column 6), which represents the proportion of the signal energy separated by the s-SSA from the original time sequence, demonstrates the effectiveness of the s-SSA procedure in terms of the pyloric rhythm extraction. Indeed, in most cases where the pyloric rhythm is detected, the percentage is over 85%.

Finally, the measured signal SNR (column 7) afforded by the s-SSA in extracting the pyloric rhythm was relatively and consistently low, at approximately -20dB (10% of the total signal energy). This is in agreement with the published specifications (2-10% change per 100 mV) for the di-4-ANEPPS dye adopted.

3.5. Summary

Voltage-sensitive dye imaging (VSDI) in a dye bath setting can provide in a single experiment a large-scale view of network activities at single cell resolution. Until now, this was not possible by means of the traditional method of intracellular recording using sharp glass electrodes due to the physical constraint of space, or, in the case of an injected dye, the long execution time with the resulting risk of damaging the sample.

Previous studies using VSDI in the STG have used the simple method of *event-triggered time averaging* to study the data in an attempt to model the pyloric neurons for each recording. The work presented here, however, entailed the first-ever development of robust signal processing procedures, constructed using the SSA technique, to extract the pyloric rhythm generated by the respective neurons, with demonstrable accuracy and consistent results. The SSA based signal decomposition procedure separates the original signal into two subspaces: (i) a signal consisting of the mixture of a small number of independent and interpretable components, and (ii) a random or structureless noise. As such, the sequential SSA (s-SSA) algorithm so developed uses a variation of the basic SSA technique to offer a multiresolution approach of signal analysis. Essentially, the algorithm works by applying the basic SSA repeatedly with different parameters (window length) to the residuals generated from the preceding analysis.

Two key advantages of the multiresolution s-SSA procedure (s-SSA) are noted:

1 – It obviates the previously adopted *event-triggered averaging* procedure that manipulates data over fixed cycles or windows, which is simplistic, laborious and (thus) error-prone, as it requires manual, cycle-by-cycle estimations.

2 – By selectively removing unwanted noise components, particularly around the desired pyloric frequency, the multiresolution approach offers a signal extraction procedure with demonstrably superior performance in terms of frequency resolution and signal selectivity.

4. Pyloric Neurons Identification

The data and analysis presented in this chapter are published by dos Santos, Andras and Lam (2017b), and form the second of the three tests of concept. In addition, some of the results obtained were also presented in dos Santos, Lam and Andras (2017a). Previous work as presented in the preceding chapter demonstrates the development of a computationally robust methodology that is capable of extracting the pyloric rhythm directly from the optical recordings of bath dyed live cells. In addition to the use of intracellular recordings of the participating neurons (three PY neurons), to elicit the ultimate ground truth, the work presented in this chapter describes the continued effort in developing computationally tractable and biologically meaningful metrics, which can identify from these recordings the neurons responsible for generating the extracted pyloric rhythm. Specifically, the duty cycle (DC), which specifies the percentage time of an active signal of a spiking neuron has been studied with reference to the three phases of the triphasic pyloric rhythm as recorded on the lvn. The latter provides both a collaborative and discerning reference with which the pyloric rhythm obtained from the individual ROIs of the dye-bathed STG sample can be compared and, importantly, mapped to the individual pyloric activities (PD, LP and PY) monitored on the lvn. To our knowledge, the work presented here represents the first ever-successful identification of individual neurons from the dye bath directly using VSDI, also validating the multiresolution s-SSA technique described in the previous chapter.

Figure 29 depicts a summary of the work presented in this chapter. An introduction in section 4.1 to the chapter is followed by the use of DC, measured in terms of the ratio of harmonics obtained in the frequency domain, as a biometric to distinguish the individual pyloric phases, demonstrated in section 4.2. After a brief description of the experimental methods (section 4.3) including the intracellular and extracellular signal extraction, the next two sections (4.4 and 4.5) explain the signal processing analysis performed, in addition to the alternative approaches. The results and discussions

in section 4.6 are included before the presentation of a summary in section 4.7 that concludes this chapter.

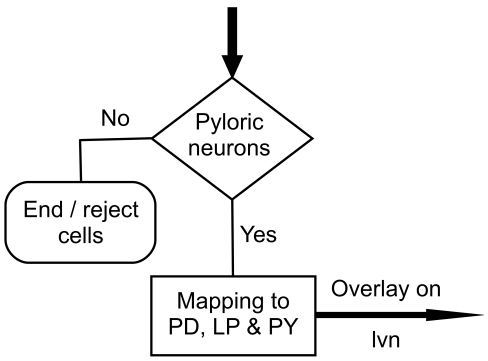

Figure 29 – *In summary, optical VSDI data obtained for the bath dyed STG sample are studied in conjunction with recordings of the pyloric activities monitored on the lvn. Signals containing the pyloric rhythm as detected in both sources are analysed and compared with the goal to identify the pyloric neurons in the STG sample.*

4.1. Introduction

The use of the VSDI allows multiple point recording, where intracellular recordings only allow up to eight cells recording (Miller, 1987; Faumont *et al.*, 2005; Selverston and Rabinovich, 2009). With an objective of 20x, however, the entire STG could remain in focus within the field of view, thus allowing all neurons (totalling 26) to be monitored and recorded simultaneously. In practice, however, only 16-20 cells can be identified with little difficulty in most cases, with a maximum of 22 cells identified over 40 experiments/studies that have been carried out to date. In other words, the use of VSDI using bath application allows at least twice the number of recorded cells when compared with the traditional electrophysiological methods such as intracellular recordings with sharp glass electrodes.

As explained previously (in section 2.1.4), the pyloric rhythm is a spontaneous rhythm in the STG regarded as a CPG that controls the muscles of the pylorus, the region where the food is filtered after the chewing process. This present chapter builds on the previous work (dos Santos, Andras and Lam,

2017a) where the pyloric rhythm was extracted accurately, using VSDI data from the STG of the crab *C. pagurus*. Specifically, the work reported in this chapter seeks to tackle challenges in identifying the neuronal types of the pyloric cells in the bath dyed STG sample, as follows:

(1) The relatively low yield of the potential-dependent fluorescence change (2-10%/100mV) achieved by the di-4-ANEPPS means that it only captures a small fraction of the voltage membrane changes.

(2) The inherently triphasic pyloric rhythm monitored on the lvn by the activity of three distinct types of neurons; namely, LP (one cell), the PY (5 cells) and the PD (two cells), that were recorded as extracellular neuronal potentials (spikes) corresponding to the highly coordinated oscillatory activities of the participating neurons. Like any other extracellular electrode recording of neuronal activity, such recordings are typically displayed in the form of a high-frequency sequence or train of spikes (bursts). In light of these complex recordings, there is a need to develop robust signal processing procedures that could identify the neuronal network activities, at a single-cell resolution. Additionally, from a signal processing perspective, the procedures developed should also facilitate analysing these spike trains of the pyloric rhythm in order to decode the three characterising phases of the pyloric rhythm.

(3) The time lag between the optical image (camera recording of the STG) and the analogue recording captured on the lvn due to the delay of the axonal transmission is unknown. Technically speaking, such a discrepancy in timing measured between the characteristic spikes/peaks of the individual neurons obtained from the optically recorded dye bath and the extracellular recording on the lvn is dependent upon a number of factors. The latter include the size of the animal and thus the STNS, the length of the lvn after the dissection and the location of the petroleum-jelly well in the lvn.

Briefly speaking, the techniques presented in this chapter rely on the development of biometrics based on the well-documented electrical properties and activities of individual pyloric neurons (described in section 4.2) measured on the lvn. The developed biometrics a then used to compare

with those measured with the VSDI data captured from the bath dyed STG sample. Specifically, three (out of five) PY neurons, which were identified previously by intracellular recording, were chosen to facilitate developing the procedures required. Here, multiple copies of these neurons are used to afford the study of corroborative empirical measurements of the STG sample as a group and, importantly, a statistically reliable set of data (ground truth) upon which these procedures were developed.

4.2. The Duty Cycle (DC) and Ratio of Harmonics (RH) as Biometrics Components

As explained in section 2.2.1, the DC can be an important biometric parameter as it maintains fixed phase relationships of the pyloric neurons that fire in a fixed synchronised pattern during a cycle, and repeat at a constant frequency. Thus if this cycle frequency/period is disturbed, the neurons firing pattern/DC will adapt to new conditions maintaining the phase relationship within each cycle. Computationally, in addition, it can also be used a descriptor for the 'shape' of a periodic waveform, which can be evaluated and defined by means of the classical (signal processing) theory of harmonic analysis.

From a biological viewpoint, the network (pyloric rhythm) is well coordinated between inhibition signals and release of neurotransmitters (mainly cholinergic and glutamatergic) to activate a cascade of successive neurons, where the strongly coupled pacemaker (AB-PD) neurons fire; it inhibits all the rest of the network as explained in section 2.1.2 (pyloric rhythm activity). The ability of the pacemaker to preserve a constant DC as the frequency varies is extremely important for the maintenance of a constant relative phase in the follower neurons. Recent studies (Tang *et al.*, 2010; Caplan, Williams and Marder, 2014; Soofi *et al.*, 2014; Marder, Goeritz and Otopalik, 2015; O'Leary and Marder, 2016) have shown how pyloric and gastric neurons maintain their phase relationships with dramatic changes in temperature, preserving a relatively constant DC in individual neurons. This

phase relationship is maintained despite variations in other factors (previously described in section 2.1.1) such as modulation or animal-to-animal variability.

These frequency changes in the rhythm directly affect the relative phase of each neuron and, therefore, the overall cycle at a given time, making the DC an exceptional characteristic that can be observed in the course of a recording.

Given the above, it was expected that the duty cycle and frequency of each neuron should remain constant during each recording (which lasted for 32.67 seconds) in the absence of any external factors such as temperature or modulation that might affect the recording. This was confirmed, as expected, following the deconstruction of regular phasing of the pyloric activities monitored and recorded on the lvn – see description in sections 4.4 and 4.6 later in the chapter.

The DC of a pyloric neuron enables the study of the waveform using the classical theory of Fourier or harmonics analysis as explained in section 2.2.1. In general, when a periodic signal is not a pure sinusoid it contains 'harmonics' or 'overtones' that are multiples of the fundamental frequency with various amplitudes and phases; this was illustrated in Figure 7, where the mathematical model was also explained in section 2.2.2.

A key aspect of the work presented in this study concerns the characterisation of the extracted pyloric rhythm using its first three harmonics. This would, in principle, provide a good practical approximation of the original signal or waveform, as they collectively account for most (>80%) of the signal power (Sayood, 2012) – see equation (7) in section 2.2.2. Indeed, this was also confirmed in the analysis of the resulting scree-plots described in section 3.4, where the first few components associated with the extracted pyloric rhythm account for a significant proportion of the total energy – over 70%.

In passing, it should be noted that, to facilitate calculating the DC in the frequency domain, the technique ratio of harmonics (RH), described in section 2.2.2, was used here – specifically, RH_{21} and RH_{31} defined respectively as the ratios between the second and the first harmonics, and the third and first harmonics.

4.3. Experimental Methods

The methodology used was the same as that described in detail in section 3.2.1 for this test of concept study. Briefly, live animals were obtained from Hodgkinson Fresh Fish, Manchester, UK, and kept in artificial seawater tanks. Dissection and electrophysiology recordings followed the protocol described in sections 3.2.2 and 3.2.3; the imaging followed the protocol described in section 3.2.4, and the data extraction was described in section 3.2.5. Similarly, the data extracted from the VSDI are from three PY neurons, which were identified using the intracellular technique described below. The intracellular recording method from which the ground truth (PY neuron) was obtained, completed with a brief description of the signal extraction process, are described in sections 4.3.1 and 4.3.2 that follow.

4.3.1. Intracellular Identification

Standard intracellular recording technique using glass microelectrodes was performed to identify the target neurons (PY) (Bartos and Nusbaum, 1997; Blitz and Nusbaum, 1997; Stein *et al.*, 2006). The sharp glass electrode was freshly pulled using a P-97 Flaming/Brown Micropipette Puller (Sutter Instruments, Novato, CA, USA), using a standard borosilicate glass capillary with filament (World Precision Instruments, Sarasota, FL, USA). To cook the electrodes for the right resistance, 10-20MΩ, taper and tip size (shape) the instructions were followed from Oesterle (2015); Table 4 shows the puller settings used to achieve this.

Table 4 – Micropipette puller settings.

Ramp	Heat	Pull	Velocity	Time/Delay
515	514	130	80	150

Then the electrode was filled with a microelectrode solution, 3M KCl (potassium chloride) using a MicroFill micropipette (World Precision Instruments, Sarasota, FL, USA).

A Scientifica PatchStar Micromanipulator (Scientifica, Uckfield, UK) was then used to place the glass electrode in the appropriate position to record from the cell body of the neuron. The recordings

were made using an amplifier, Intracellular Electrometer model IE-251A (Warner Instruments, Harvard Apparatus Company, Holliston, MA, USA), passed to a CED MICRO 1401 (Cambridge Electronic Design) data acquisition box and read using Spike2 v8.07 (Cambridge Electronic Design). Figure 30 shows one PY neuron identification in Spike2 with intracellular techniques and the synchronised pyloric rhythm from the lvn.

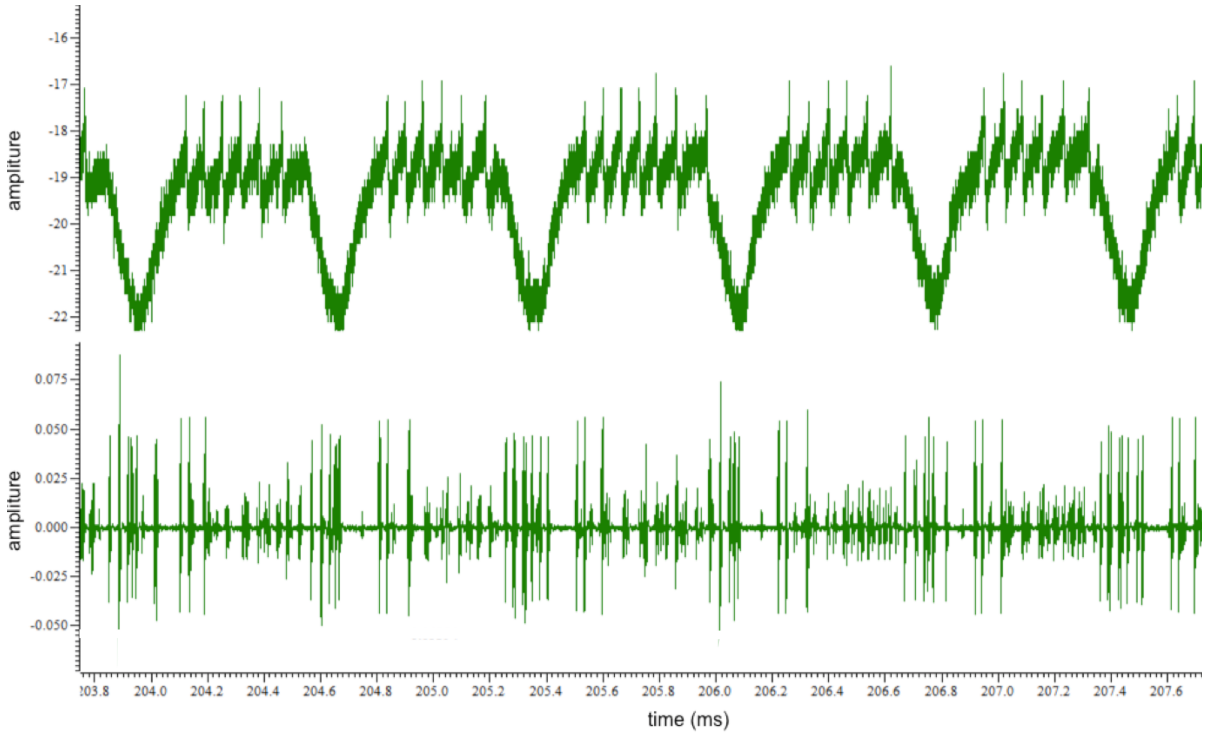

Figure 30 – An example of the intracellular recording from a PY cell in Spike 2. (Top) An example of the intracellular PY neuron recording obtained. (Bottom) The simultaneous recording of the electrophysiological analogue signal monitored on the lvn.

4.3.2. Analogue Signal Extraction

The extracellular recording data captured by the imaging software (BV-Ana) described in section 3.2.3 from the lvn during the recording (32.67s), are extracted onto a datasheet and analysed in MATLAB® (MathWorks, Natick, MA, USA).

4.4. Signal Processing Procedures

As discussed in section 4.2, the DC, (conventionally) measured in the time domain, and the equivalent representation in the frequency domain, RH, were used as biometrics to facilitate comparison and identification of the optical and electrophysiological data recordings captured in the dye bath and on the lvn respectively. As such, they are key to providing the discerning references to the analysis and decoding of the neuronal activities captured on the lvn in accordance with the neurons responsible for the triphasic pyloric rhythm (PD, LP and PY).

The deconstruction of the pyloric rhythm captured on the lvn involved was achieved in two key stages, described as follows.

- Firstly, the extracted data from the lvn was analysed with the SSA previously described by dos Santos, Andras and Lam (2017a) and continuous wavelet transform (CWT) which was obtained using analytic Morse wavelet-based time-frequency decomposition. Figure 31(A) and (B) shows the spectrograms of the CWT of the (raw) data before and after the application of the SSA procedure (see section 2.2.8). The improvement or clarity afforded to the frequency responses of the SSA processed lvn, particularly at the lower frequency bands (red rectangle), can be seen in the bottom spectrogram. Specifically, the contrast afforded by the bottom power spectrum was about three times the top one. This is illustrated in Figure 32, where the demarcated rectangular regions (red) as shown in Figure 31 were enlarged to help better appreciate the details containing the lower frequency band after the application of the SSA procedure.

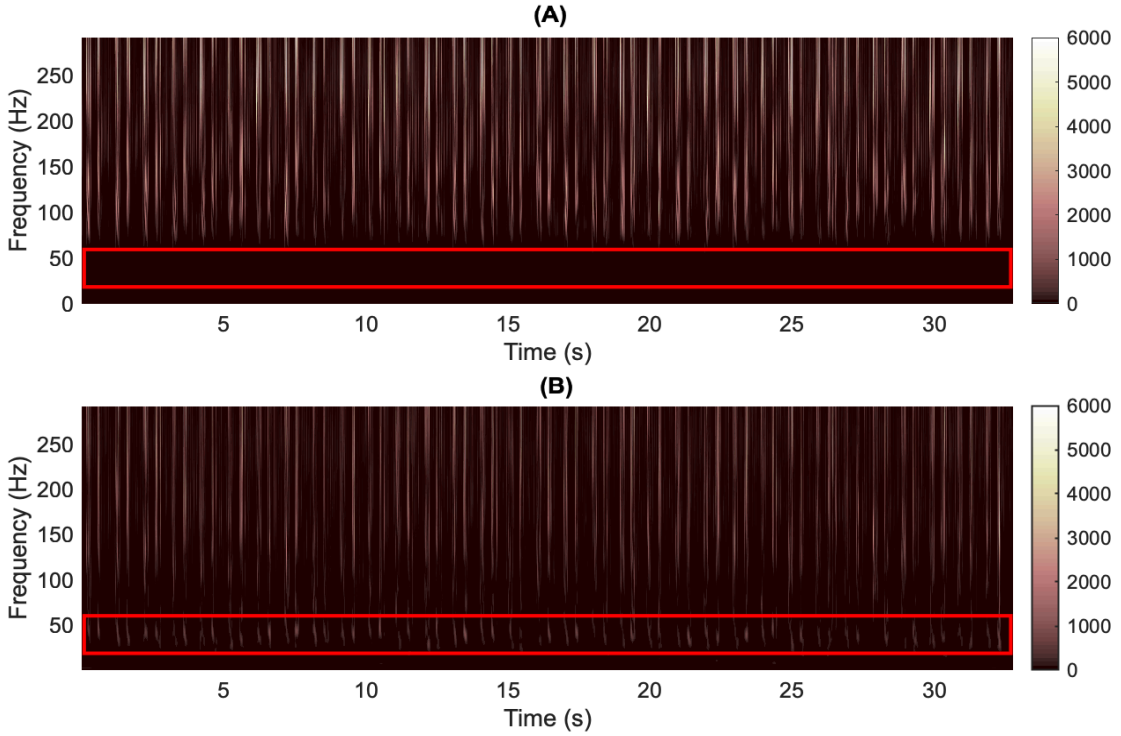

Figure 31 – Spectrograms generated with wavelet (Morse) based time-frequency decomposition from lvn data. (A) Before SSA analysis. (B) After the SSA analysis. The colour bar accompanying each figure represents the amplitude computed by CWT. NB. The content of the red boxes are expanded in figure 32.

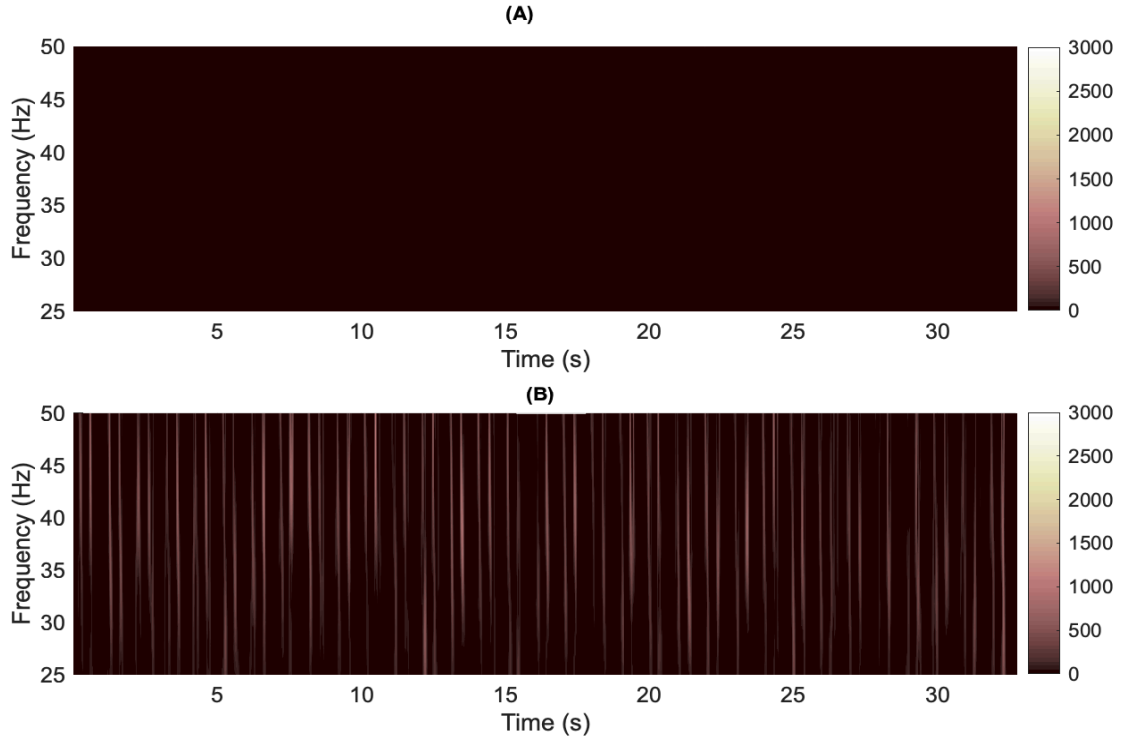

Figure 32 – Spectrograms of narrowband, (A) in raw data from lvn, and (B) the data after SSA analysis. NB. The expansion of the red boxes in figure 31.

- Secondly, analytic Morlet wavelet was applied to the lvn data after the application of SSA. As discussed in section 2.2.5, this wavelet is known for its superior time localisation property. As such, it was used here to better localise the transitions between individual phases of the pyloric rhythm from the relatively noise-free recording on the lvn. Specifically, the deconstruction of the triphasic pattern was achieved by selecting a frequency band in the spectrogram displayed in Figure 32(B), where the amplitude response to the PY neurons would be considerably reduced or suppressed, enabling the responses present in the PD and LP neurons to be clearly seen.

Figure 33 depicts the results in the time domain, where the responses obtained in the three frequency bands are shown (34.6Hz, 37.1Hz and 39.7Hz) alongside the relatively noise-free lvn signal (magenta) and the end-of-cycle marker (*). Here, it is apparent that the PY neurons are effectively silenced in the selected frequency bands. Accordingly, the lvn was partitioned or segmented by means of the start and stop locations for the 'silenced' periods where the Morlet-based CWT response (at 37.1Hz) is minimal, with added markers that include: PY*start* and PY*end* (local peaks of the CWT response), PD*end* (also end-of-cycle markers), and, finally, LP*start* (end of the silenced period following PD*end*).

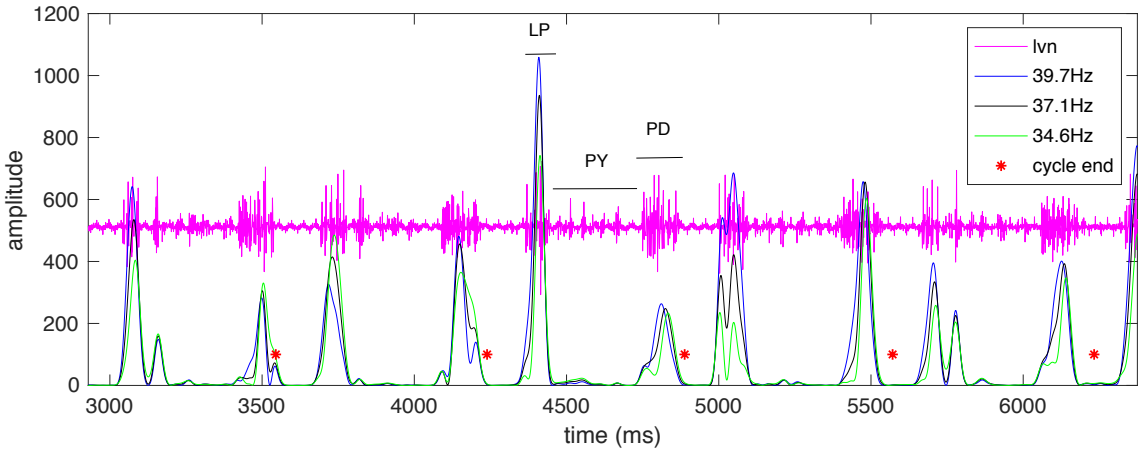

Figure 33 – Responses of the analytic Morlet wavelet in different frequency bands where the PY cells are "silenced". The noise-free lvn overlaid to demonstrate the accurate time localisation of the transitions between LP®PY and PY®PD cycles.

In summary, the combination of the SSA (previously developed) and CWT (Morse and Morlet wavelets) provides a practical solution for the second problem identified at the beginning of this chapter (section 4.1). Specifically, the procedure described here successfully addressed the challenge posed by the high-frequency spike/sequence observed on the lvn, making it possible to decode the three respective pyloric phases (LP, PY and PD), each of which was modelled as a rectangular pulse train corresponding to that generated by the respective pyloric neurons. This also enables, importantly, the DC to be computed directly on the lvn; that is, in the time domain as described at the start of this section.

4.5. Spike Sorting as an Alternative Approach

To facilitate analysis and identification of the pyloric rhythm extracted from the optical recording/data of the STG sample with reference to triphasic pyloric rhythm observed on the lvn, the individual phases of the triphasic pyloric rhythm recorded on the lvn must be determined. Here, so-called spike sorting techniques that had been developed to analyse the individual shape of spikes/waveforms recorded extracellularly as 'action potentials' of different neurons by one or more electrodes could be used (Gibson, Judy and Marković, 2010).

Broadly speaking, such techniques often measure similarities in spike pattern, including particularly shape and size, to help classify or identify the cluster of functionally related neurons (Lewicki, 1998). While a detailed discussion or review on this approach is outside the scope of this thesis, it should be noted that, given the task at hand, it is most difficult to identify the best algorithm with sufficient generality. Equally, it is also a non-trivial task to define which spike sorter is the most appropriate in terms of the requirement for minimal manual curation in order to accurately classify an unknown spike/waveform (Gibson, Judy and Marković, 2010); see also the most results reported in Chung et al. (2017). More specifically, the features-based approach that is primarily based on PCA and ICA to group spikes into clusters both rely on the orthogonality of components in a

mixture and are unlikely to perform well, as the triphasic pyloric waveforms generated by the participating neurons are necessarily non-orthogonal (dos Santos, Andras and Lam, 2017a). Specifically, the orthogonal requirement between components means that PCA is only solvable with linear algebraic decomposition techniques and mean-removal process before construction of the relevant covariance matrix (Shlens, 2014). However, the triphasic pyloric rhythm of the STG as led by the respective neurons (PD, LP & PY) is not orthogonal, and thus not separable, as these neurons generate the same (pyloric) frequency but with different phases. Further, PCA depends on the scaling of the variable and is extremely sensitive to noise (or outliers); as such, it critically depends on the SNR of the data at hand. In a similar vein, the ICA-based techniques, described in section 2.2.10, were unlikely to work well when applied to the STG data. This is due to the fact that the triphasic rhythm is far from independent; quite the reverse, the triphasic rhythms individually led by the PD, LP and PY neurons are mutually exclusive and, thus, not independent. In other words, the presence of the PD-led rhythm is dependent on the absence of that led by the LP and PY neurons; the same applies to either the LP or PY.

On a related application reported in Städele et al. (2012), both ICA and PCA techniques were adopted to improve the SNR of the optically recorded data for the STG, and neither were found to offer better results with statistical significance. Likewise, the template-based approach was unlikely to work well, as both the spatial and temporal variations displayed on the lvn would require access to an unrealistically large number of test/samples, probably coupled with the inherently error-prone requirement for manual curation, to be compared with the very noisy data obtained by VSDI (Swaroop and Sharma, 2016).

4.6. Results and Discussions

The validation process uses three known PY neurons as ground truth with the associated VDSI data to facilitate comparison of the pyloric rhythm (where present) extracted from the optical data

collated for the STG sample. As in chapter 3, the pyloric rhythm was identified using the multiresolution s-SSA procedure previously developed and described in section 3.3.

As described in section 4.4, the lvn data were segmented into individual phases led by the individual neurons. This has permitted the separation of the individual neurons responsible for the triphasic pattern. Individual neuron segregation has allowed the reconstruction of the rhythm of the PY phase neurons; the total wave energy of each cycle was also computed to approximate the average amplitude for the reconstructed pulse train (as described in section 2.2.1).

In this study, it was found that there were approximately 32 pyloric cycles (manually counted in the lvn) present over the 32.67s of the recording. This corroborates the extracted pyloric frequency of 1.017Hz (≈32/32.67) from the optical recordings of the STG sample.

An example illustrating the method described in section 4.4, which explained how the triphasic pyloric rhythm was decoded here, is shown in Figure 34 and Figure 35. Specifically in, Figure 34 the PY phase/cycles were overlaid on the top of the lvn recording. Here, the descriptive statistics of the DC of each PY neuron were calculated for the complete recording (32 pyloric cycles) and noted as follows: DC_{mean} = 40%, $DC_{s.t.d.}$ = 7%, DC_{min} = 26% and DC_{max} = 50%. This has allowed concluding that PY neuron was active 40% of the cycle, with a standard deviation of 7%, the cycle where the PY neurons smallest activity in a cycle was 26% of a cycle, and the maximum activity was 50% of a pyloric cycle.

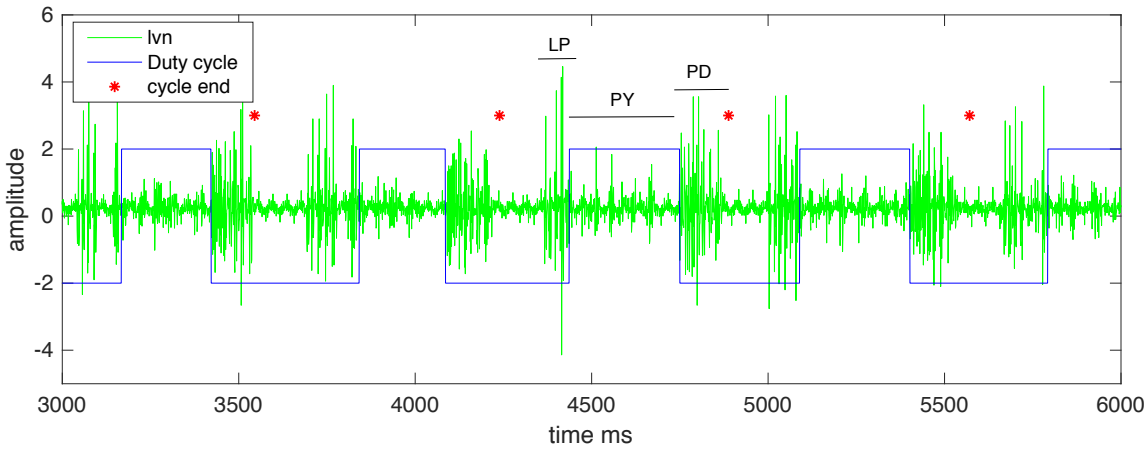

Figure 34 – Reconstruction of the PY burst train using the duty cycle on the lvn recording (green background). The red asterisks are included to mark the end of the PD/burst, to aid visual examination.

The above deconstruction is further illustrated in Figure 35, where the combination of Figure 33 and Figure 34 are observed after the localisation of all start, stop and silence periods are demarcated on the lvn by each participating neuron. As shown in Figure 35, the result is a completely segmented lvn that has enabled the estimation of the respective DC of the PD, LP and PY phase neurons.

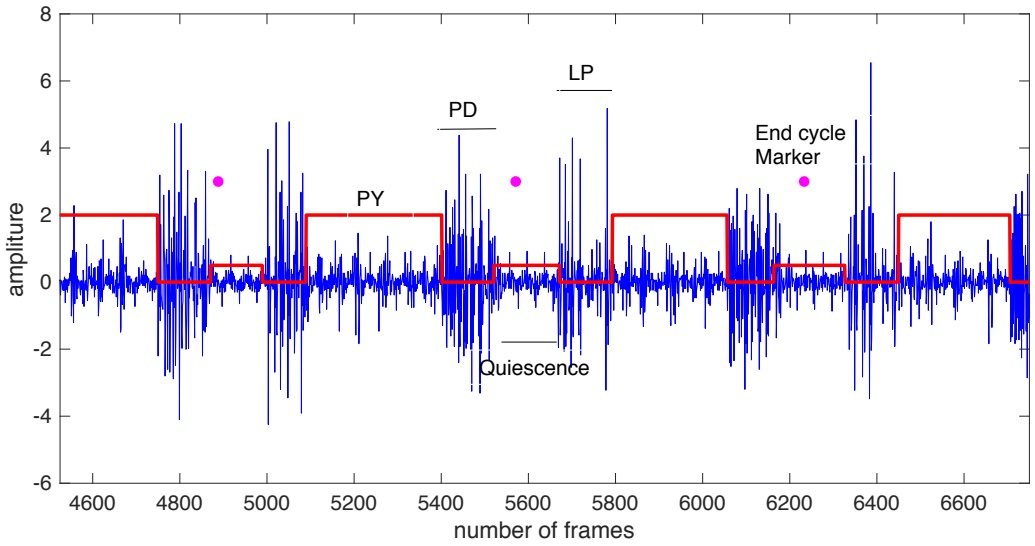

Figure 35 – Reconstruction of the neurons, burst train (red) with successive quiescent periods (red) on the lvn recording (blue).

As discussed in sections 2.2.1 and 2.2.2, the DC could be evaluated in the frequency domain using classical Fourier-based harmonic analysis – see equation (3) in section 2.2.2. To facilitate a like-for-like comparison, the spectral content of the reconstructed PY burst train on the lvn (Figure 34), shown in Figure 36(D), was examined in conjunction with the periodograms computed for the three PY neurons in respect of the pyloric rhythm extracted from optically recorded dye bath data. The pyloric frequency and its higher order harmonics of the pyloric rhythm extracted for each of the three PY neurons are also noted in Figure 36(A, B & C). As expected, the computed pyloric frequency (1.017Hz), as well as its harmonics (2.045Hz and 3.052Hz for the second and third harmonics) contained in the pyloric rhythm of each of the PY neurons are all shown to have an almost identical pattern. Further, the RHs and thus the corresponding DCs were also calculated and displayed in each of the four periodograms (Figure 36(A, B, C & D)) depicted in Figure 36 (as RH_{21} and RH_{31}). Expectedly, they are all in good agreement, with DCs calculated: DC_{cell_1} = 40%, DC_{cell_2} = 40%, DC_{cell_3}

= 38%, respectively for the three PY neurons, which compare well with the mean DC of 40% obtained directly from the PY pulse train separated/reconstructed on the lvn in the time domain as discussed above.

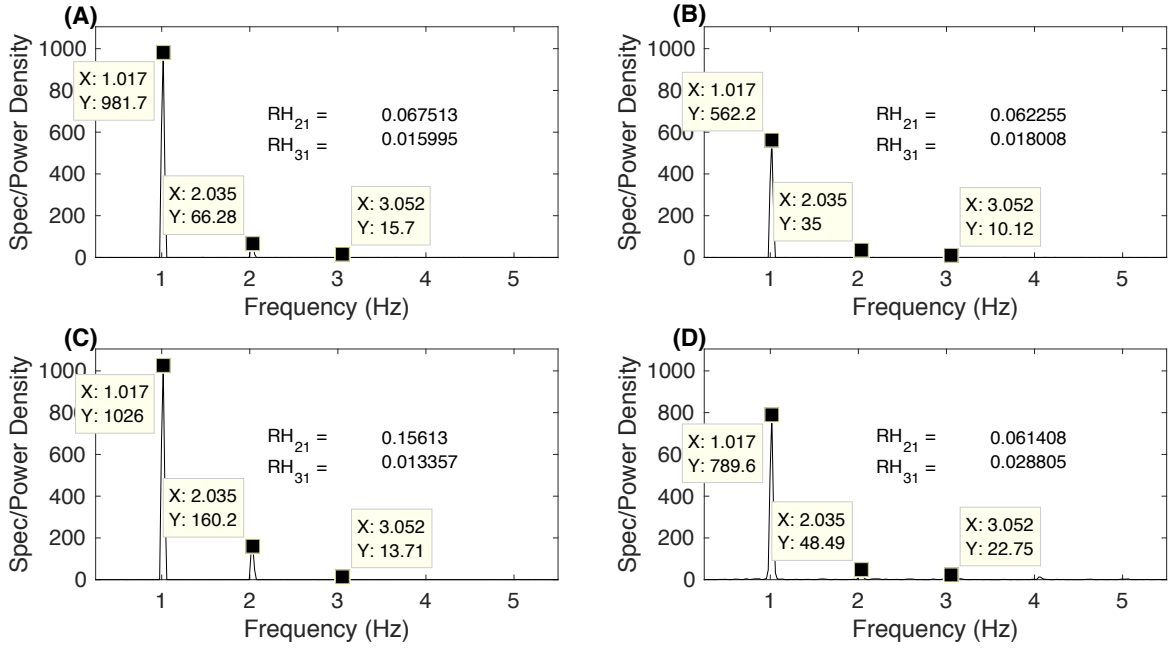

Figure 36 – Periodograms constructed for the individual PY cells (A, B & C – PY neurons 1, 2 and 3, respectively) and the reconstructed PY burst from the lvn (D), showing the pyloric frequency, 2nd and 3rd harmonics at 1.017Hz, 2.035Hz and 3.052Hz respectively.

To address the time lag between the optical and electrophysiological recordings, the Hilbert transform approach, discussed in section 2.2.6, was adopted to determine the timing delay from the optical recording of the dye bath to the electrophysiological recording on the lvn. As described in section 2.2.6, the instantaneous phase of each of the three PY neurons was computed from the respective Hilbert spectra (Hahn, 1996). Here, the effectiveness of the s-SSA in extracting the mono-frequency component of the pyloric rhythm extracted for each cell was evident. Specifically, the single-tone pyloric rhythm extracted from the dye bath for each of the three PY neurons was compared with that obtained from the pyloric phases re/constructed on the lvn, allowing the respective delay to be computed, with a high degree of accuracy. The results are summarised in Figure 37, where it is shown that the time lag between the individual PY cell and the lvn maintains,

on average, an expectedly constant and consistent phase shift of 3.43 radians (mean (3.568, 3.3394, 3.412)) with a standard deviation of 0.24 (mean (0.22492, 0.22535, 0.27981)) radians over the entire course of the recording.

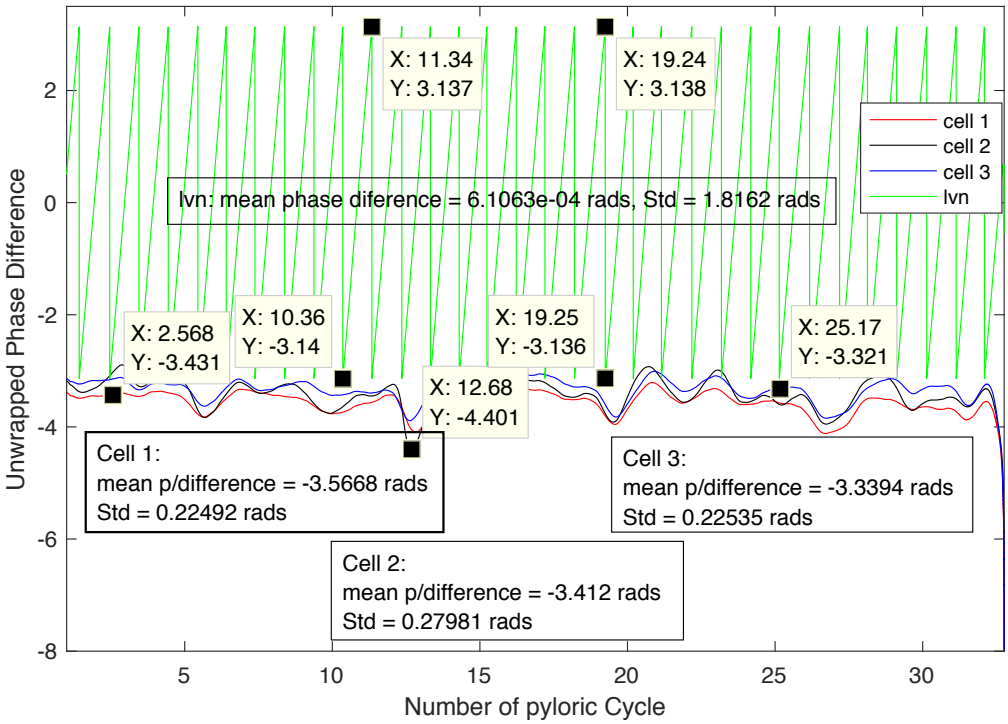

Figure 37 – The instantaneous phase shift between the optical and lvn recording obtained for the PY cells (cells 1, 2 &3). The instantaneous phase changes of the lvn recording over the ~33 pyloric cycles are also shown as a reference (green) in addition to the mean phase shift difference (mean p/difference) and standard deviation (Std) for each cell.

In passing, it is worth noting that the mean phase difference computed for each neuron/cell has an expectedly negative value, given the fact that the pyloric rhythm present in the dye bath data (recorded optically) using the VSDI needed to travel down to the lvn where the extracellular recording took place. In other words, the signal/rhythm emerged from each PY cell in the bath dyed STG sample is first captured by the camera and then by the extracellular recording after it had travelled through the axon connected to the lvn. This is illustrated in Figure 38, where the mono-component rhythm extracted from one of the PY neurons (cell 3) is realigned to the lvn using the computed phase shift of -3.3394 radians, or equivalently, a lead time of $1/(1.017) * 3.3394/(2\pi) = 0.5226$ seconds.

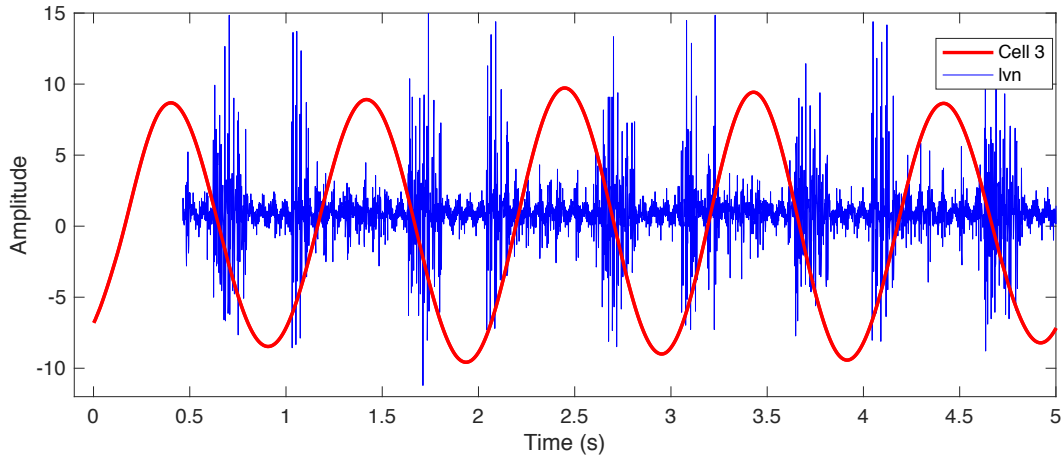

Figure 38 – The mono-component (first harmonic) signal extracted from the PY neuron (red), showing the time lag between the optical and extracellular recording (blue), with a mean shift of -3.3394 radians.

As a final note, the self-same approach discussed above was also applied to the results shown in Table 3 (in section 3.4), to facilitate estimating the time/phase shift between the optical and lvn recordings. Here, the pyloric rhythm extracted from three ROIs (corresponding to cells 5, 6, 13) where the pyloric frequency was detected was overlaid on top of the lvn, without any adjustment of the phase shift. This is shown in Figure 39 (see dos Santos, Lam and Andras (2017a)).

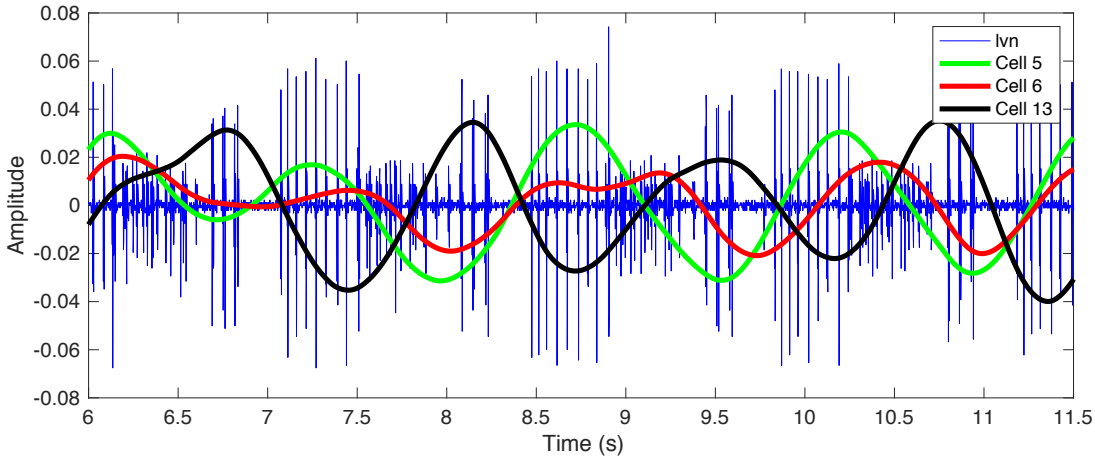

Figure 39 – Three cells from Table 3 before the time shift (5, 6 & 13) overlaid on the lvn (blue).

In terms of the computed DCs, it can be observed that the pyloric rhythm computed for each of the three cells aligns reasonably well with of the pyloric phases observed on the lvn. Based on Figure 39, here, one could suggest that cell 5 (green) is an LP-time neuron, cell 6 (red) a PY-timed neuron, and cell 13 (black) a PD-timed neuron. However, further analysis of the respective timing delays

determined by the Hilbert Transformation approach has revealed that the pyloric rhythm extracted for cell 13 should be realigned to correspond to a PY-timed neuron and not to a PD. As depicted in Figure 40, similarly, cell 5 should correspond to a PD-time neuron (instead of an LP cell), while cell 6 should be mapped to an LP-timed (instead of PY-timed) cell. A couple of notes are in order. First, as presented in Table 5 (see section 5.5), the SNRs estimated for cells 5 and 13 are significantly better (> 5dB) than that achievable for cell 6, whose estimated spectrum shows two closely spaced responses (only 0.03Hz apart) at the pyloric frequency of 0.7324Hz. Second, cell 13 could be indeed identified as a PY neuron in light of the computed DCs (0.39 and 0.41) that are both in good agreement with that estimated on the lvn for the PY cell (0.384).

Indeed, as the optical recording is, by necessity, ahead of the lvn, the pyloric rhythm/signals extracted for all the neuronal cells in the STG sample should be shifted to the left of Figure 39.

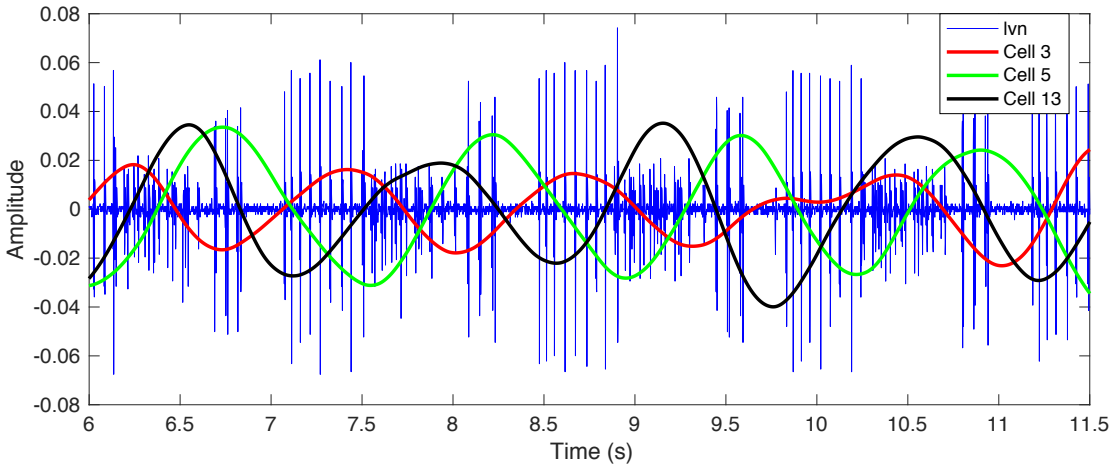

Figure 40 – Three cells from Table 3 (cell 5, 6 & 13) after time shift alignment overlaid on the lvn (blue).

The importance of synchronising both recordings as captured from the bath-dyed STG sample and on the lvn is evident in the example above. Specifically, the pyloric rhythm, if present, originated from the STG sample has a constant lead time (measured in phase differences/radians) over the (PY-timed) rhythm recorded on the lvn; see Figure 22(A). Here, the averaged phase shift/lead of -3.43 radians by the 3 PY cells, as shown in Figure 37, represents a little over half a cycle or π = 3.1416 radians, corresponding approximately to ½ of the period of a pyloric cycle; that is, ½* 1/1.017Hz ≈ 0.49 second. As discussed above, this computed time shift is essential to enable synchronisation of

the pyloric rhythms captured in the optical/VSDI and analogue/lvn recordings, as such recordings are taken simultaneously at two different but physically connected sites within the STNS.

4.7. Summary

The work presented in this chapter aimed to identify pyloric neurons in the STG using the image/data obtained from the optical recordings with the VSDI approach. It had three closely allied objectives (see section 4.1) that sought to:

(1) Validate the computational procedure developed previously for extracting the pyloric rhythm from such recordings, given the typically poor SNR achieved by the Di-4-ANEPPS dye used in the thesis.

(2) Analyse the pyloric rhythm obtained in (1) with reference to triphasic pyloric rhythm observed on the lateral ventricular nerve (lvn) that captures the activity of three distinct types of neurons, namely, PD (x2), LP (x1) and PY (x5).

(3) Compare the results obtained in (2) by integrating data obtained from optical/VSDI recordings and electrophysiological recording of the lvn.

For objective (1), the multiresolution procedure described in dos Santos, Andras and Lam (2017a) and in the preceding chapter was applied to the individually separated ROIs identified in the bath dyed STG sample to extract, if present, the relevant signal sub/components of the pyloric rhythm. To facilitate validation of the resulting pyloric rhythm, the computationally tractable and biologically meaningful biometrics of duty cycle (DC) and relatedly ratio of harmonics (RH) were developed and evaluated using three PY neurons, which were identified intracellularly (as ground truth). Here, the signal components bearing the first and second harmonics of the pyloric frequency were isolated, enabling estimation of the DC by means of RH and thus identification of the participating pyloric neurons (dos Santos, Andras and Lam, 2017b).

For objective (2), the primary task was to separate/decode the triphasic pattern of the pyloric rhythm captured on the lvn by virtue of the spiking characteristics of the respective participating neurons. Here, the spontaneous motor pattern generated by the highly synchronised activity of the PD-timed, LP-timed or PY-timed neurons monitored on the lvn were analysed and segmented using the widely studied multiresolution technique of time-frequency analysis (Akansu and Haddad, 2001; dos Santos, Andras and Lam, 2017b). The latter enables the highly structured and regular phasing of the pyloric rhythm captured on lvn to be deconstructed. Importantly, the task was assisted by the s-SSA procedure, which sought to remove noise from the lvn while selectively preserving the pyloric frequency and its higher order harmonics. Specifically, the analytic Morlet wavelet was used to localise the transients between individual phases of the pyloric rhythm from the relatively noise-free recording of the lvn. This was achieved by selecting a frequency band in the spectrogram where the amplitude response produced in the PY-timed pyloric cycles and the quiescent phase/period were significantly lower (~75%) than that in either of the LP-timed and PD-timed pyloric cycle. Using a simple threshold procedure the respective time periods of the PY phase were segmented from the single pyloric cycle recorded on the lvn and, subsequently, the corresponding duty cycle of the PY phase was computed.

Last but not least, to accomplish objective (3), the Hilbert transform approach (discussed in section 2.2.6) was adopted to facilitate computation of the instantaneous phase of each of the three PY neurons from the respective Hilbert spectra, thus allowing direct comparisons with that obtained from the reconstructed PY spike/pulse train on the lvn. Specifically, the mono-component rhythm extracted for each of the three PY cells has allowed their respective delays to be computed with a high degree of accuracy. As expected, it is shown that the time lag between the individual PY cell and the lvn maintains a constant mean phase shift/lead of -3.43 radians with a mean standard deviation of 0.24 radians over the entire course of the recording.

5. An Automated Pyloric Frequency Estimator

The present chapter is the last of the three tests of concept; it is based on the data published in dos Santos *et al*. (2017). In addition, some of the results presented in this chapter were also presented at the SfN (Society for Neuroscience) 2017 (dos Santos, Lam and Andras, 2017b).

The preceding chapter demonstrated the identification of pyloric neurons at single-cell resolution from optical recording/data of the bath dyed STG sample. By verifying with the external electrophysiological recordings of the lateral ventricular nerve (lvn), the pyloric rhythm extracted from the individual neurons in the dye bath was successfully mapped onto the respective phases of the pyloric rhythm by means of the instantaneous phases and duty cycles computed for each of the monitored cells in the sample. However, two challenges remain; first, the integration of data obtained from optical VSDI and electrophysiological recording of the lvn is a complex and exacting task that (often) require trials and errors and thus minor manual adjustments. Second, the determination of the window length *L* for which the multiresolution (s-SSA) procedure (described in section 2.2.8) and, in no smaller part, the number of relevant components to be selected from the scree plot (section 3.3), also required *a priori* knowledge acquired from the lvn by manually selecting the relevant parameters. To address these challenges, this chapter aims not only to refine the methods presented in the preceding chapters (3 and 4), but also describe the effort in developing computational procedures that can automate extraction of the pyloric rhythm from the bath dyed STG sample and, importantly, validate the results obtained in the previous chapters.

The chapter is organised as follows: it starts with an introduction (section 5.1), followed by a description of spectral analysis as classical techniques (section 5.2.1) and the modern spectral estimation methods (section 5.2.2), then it explains the eigenanalysis frequency estimation of the pyloric rhythm (section 5.3), as the basic principle for the automated process for frequency estimation. Section 5.4 initially contains a brief description of the biology experiment, followed by a description of the methods used in the frequency estimation process; this is followed by results and

discussion in section 5.5. The chapter finishes with a summary in section in 5.6.

5.1. Introduction

As discussed in chapter 3, the neuropil is the first part of the STG to be segmented and analysed, as a ground truth known to embody the strongest detectable signal containing the pyloric frequency. As such, it was used to compare with the extracted signal/components from each cell by means of the features obtained via the computed power spectrum. Importantly, the latter helps determine the parameters used with the multiresolution s-SSA procedure – namely, the choice of the initial window width (*L*) (dos Santos, Andras and Lam, 2017a). However, such a direct means to analyse the frequency content of signals using the classical approach of harmonic analysis has considerable limitations. In particular, estimating the pyloric frequency of the pyloric neurons in the STG, given their typically low signal-to-noise ratios (SNR) achievable in the dye bath, is likely to yield results with relatively large errors in calculating key signal parameters such as frequency, amplitude and, perhaps most significantly, phase.

To overcome these limitations, this chapter seeks to investigate and develop automated procedures based on modern spectral estimator methods. The latter will enable the pyloric rhythm to be detected directly from the noisy optical recordings of dyed neuronal cells, thus obviating the need for extracellular recording from which the initial manual enumeration of the pyloric cycles is obtained to facilitate determination of the window length parameter. In particular, the estimators so constructed must take into account the potential distortions resulting from the classical (Fourier-based) spectral analysis methods, given the demonstrably noisy signals captured in the optical recordings as described above.

Technically speaking, the determination of the frequency content of a waveform is termed *spectral analysis*. From a signal processing viewpoint, spectral analysis can be thought of as a 'computational prism' that decomposes a waveform into its constituent frequencies – just as a prism

separates light into its spectrum of constituent colours or specific frequencies of the electromagnetic spectrum – and the development of a useful approach for this frequency decomposition has a long and rich history. As such, a variety of techniques exist to perform spectral analysis, each with different strengths and weaknesses. Broadly speaking, these techniques can be divided into two categories: classical methods based on the Fourier transform and modern methods such as those based on the estimation of model parameters. In most cases, the accurate determination of the spectrum of a waveform requires that the signal be periodic, or of infinite length, and/or noise free. In most practical/biological applications, the signal of interest is neither infinite nor of sufficient length so that only a portion of it is available for analysis. More relevantly, these signals are often corrupted by substantial amounts of noise and artefact, as is evident in the studies so far (dos Santos, Andras and Lam, 2017a). More specifically, if only a portion of the actual signal can be analysed, and/or a considerable amount of noise is embedded in it, then any spectral analysis procedures must necessarily be approximate – that is, they are estimates of the true spectrum. The formulation of the spectral analysis procedure is the focus of the work described in section 5.2 below, which seeks to provide a practical means to improve the estimation accuracy of the pyloric frequency from the optically recorded data of the bath dyed STG sample.

5.2. Spectral Analysis

As discussed in section 2.2.3, the frequency domain provides a different yet (often) insightful perspective through which one may view a discrete-time signal and/or random process. Mathematically, the power spectrum is defined as the Fourier transform of the autocorrelation sequence of a stationary process. In a number of applications, it is necessary that the power spectrum of a process be known – for example, digital filter design. Without prior knowledge of these power spectra, or power spectral densities (PSD), it becomes necessary to estimate them from observations of the processes and/or measurements of their resulting signals. More relevantly, as

discussed below, the power spectrum also plays an important role in the detection and classification of periodic or narrowband processes immersed in noise.

In developing techniques for estimating the power spectrum of a discrete-time signal (or random process), one will generally require an understanding of what spectral features are likely to be of interest and which methods provide the most accurate determination of those features. Two spectral features of particular interest are the shape of the spectrum, commonly termed spectral estimate, and local features of the spectrum, often known as the *parametric estimate*. As an example, the detection of a signal usually involves localising a narrowband signal/process in broadband noise, requiring a good estimate of local features. This is illustrated in Figure 41 below.

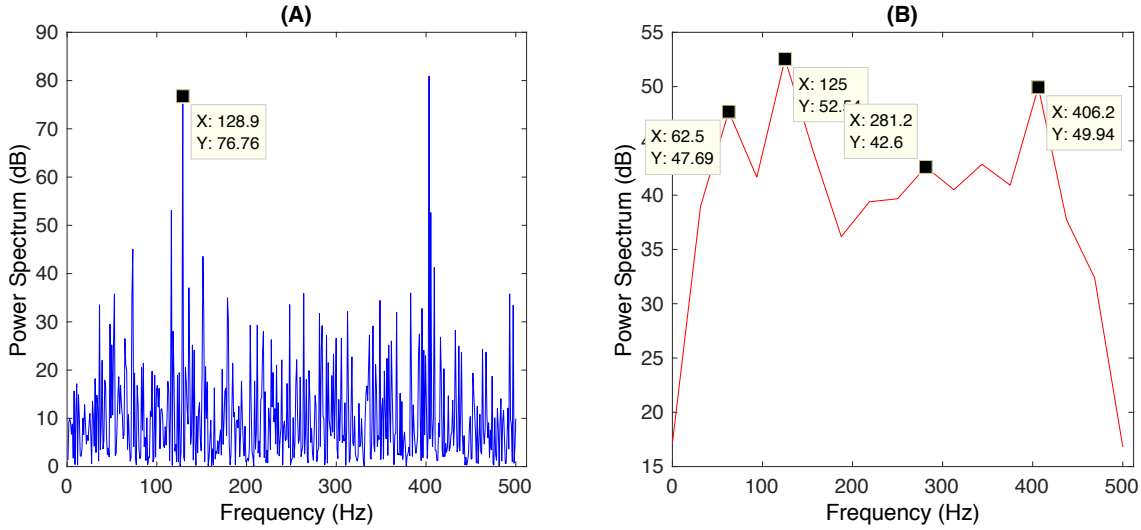

Figure 41 – Spectra obtained for a 128Hz sine wave with white noise added (SNR = -20dB) using two different methods. (A) Standard Fourier Transform from a single sine wave (128Hz) in -20dB white noise, was applied and the peak at close to 128Hz is noted, but the white noise (a broadband feature) is poorly displayed. (B) A Welch spectrum was generated with in-built averaging (smoothing – 50% overlapping Hamming Windows) producing a better estimate of the white noise (relatively small variances over the complete frequency range).

Figure 41 shows, on the left (A), the spectral estimate obtained by applying classical Fourier Transform to a 128Hz sine wave immersed in white noise, at a signal-to-noise (SNR) ratio of -20dB; that is, the signal amplitude is one-tenth of the noise. The embedded sine wave is (almost) accurately identifiable as a spike in the spectrum, while the noise, which should be (relatively) constant across

all frequencies, varies considerably (noting also the false peaks estimated around 412Hz that are not present in the original/input signal). On the right (B) of the figure is the spectral estimate obtained by a smoothing/averaging process applied to the same signal by means of the Welch's spectral estimator, which was constructed by default in thirty-two equally divided and windowed (Hamming) segments, each having a 50% overlap with the adjacent window/segments. The Fourier transform was then applied to each of these windowed segments, and the results were averaged where the adjacent segments overlap. The Welch spectrum will be described as an exemplar of classical Fourier transform based spectral estimation technique in the next section (5.2.1).

The above example serves to illustrate an important point in the development and application of spectral analysis techniques in general – namely, methods that provide good spectral estimation are poor local estimators, and vice versa. Specifically, it should be apparent in the analysis above that the resulting Welch spectrum (Figure 41(B)) provides a more accurate representation of the overall spectral features, predominantly those of the white noise, whilst the 128Hz sine signal/waveform is completely obviated. In other words, the in-built smoothing capability of the Welch estimator is a good spectral estimator in the sense that it provides a better estimate of the dominant noise component (with negative SNR), but it is a somewhat poor signal detector. Conversely, the classical Fourier Transform accurately locates the narrowband sine-based signal at 128Hz, although the dominantly white noise that has a relatively flat signal spectrum across all frequencies is somewhat obscured.

5.2.1. Classical Spectral Estimation Techniques

Classical spectral estimators are nonparametric methods that are based on the idea of estimating the autocorrelation sequence of a random process (or, simply, a signal) from a set of observed data, which is followed by applying the classical Fourier transform to obtain an estimate of the power spectrum. These nonparametric methods do not assume any model, statistical or deterministic, for the data, except that it is zero or periodic outside the observation interval. Originally published by Sir

Arthur Schuster in 1898, the so-called *periodogram* is a well known and one of the first nonparametric methods which can be directly computed via the Fast Fourier Transform (FFT) algorithm. As such, many of today's digital/signal processing practitioners consider the FFT-based periodogram to be the most 'natural' spectral power estimator, with commercially available hardware and software spectrum analysers based almost exclusively on the FFT (Stein, 2000).

Computationally, the direct approach to evaluating the power spectrum of a signal *x(t)* is motivated by the fact that the energy *E* contained in *x(t)* is related to the magnitude of the signal squared and integrated over time:

$$E = \int_{-\infty}^{\infty} |x(t)|^2 \, dt \tag{27}$$

By extension of Parseval's theorem, it can be shown that (by virtue of energy preservation),

$$\int_{-\infty}^{\infty} |x(t)|^2 \, dt = \int_{-\infty}^{\infty} |X(f)|^2 \, df \tag{28}$$

and, hence, $|X(f)|^2$ equals the energy density function over frequency *f*, also referred to as the energy spectral density, the power spectral density (PSD) or, simply, the power spectrum. Here, the power spectrum, $Ps(f)$, is computed as the magnitude squared of the Fourier transform of the waveform of interest: that is, $Ps(f) = |X(f)|^2$. It should be noted that, as the power spectrum $Ps(f)$ does not contain phase information, it is not a bilateral transform and thus cannot be used to reconstruct the original time domain signal. Further, when *x(t)* is a relatively long sample of the ensemble, averaging can be used to evaluate $Ps(f)$ to help improve the statistical properties, notably the variances, of the resulting estimation. Indeed, when the power spectrum is based on a direct application of Fourier transform over individual segments of *x(t)* and followed by averaging in the frequency domain, it is commonly known as an *average periodogram*.

One of the most widely known procedures to evaluate the average periodogram described above is attributed to Welch (Welch, 1967), who further modified the procedure in two major ways: (i) the (adjacent) segments that divide *x(t)* are allowed to overlap, and (ii) a window function *w(SL)* can be applied to each segment. This enables the production of a set of *M* modified periodograms, which

are to be averaged. A few notes are in order here. First, as with any averaging procedures, choosing a short segment length (S*L*) will provide more segments for averaging and thus improve the reliability or, more specifically, the statistical variance ($\propto \frac{1}{M}$) of the resulting spectral estimate. However, the improvement is achieved at the expense of a reduced frequency resolution ($\propto SL$), noting that $M * SL$ is a constant that represents the total length of *x(t)*. Second, by allowing overlapping segments, more segments can be averaged for a given data sample length $M * SL$. With noisy data, in practice, averaged periodograms are computed with average spectra from half-overlapping segments – that is, adjacent segments that overlap by 50%. Higher amounts of overlap can be used in other applications where the SNR is poor and, when computing time is not an issue, maximum overlap whereby adjacent segments are separated by just one sample has been recommended. Third, the use of data windowing for sidelobe[7] control is relatively less important, especially when (i) the estimated spectra are expected to be flat and/or (ii) the length of the signal/data *x(t)*, numerically calculated as $M * SL$, is long. In fact, some studies have reported that, as data windows lend some data samples more importance than others, its uses serve only to further reduce frequency resolution without a significant improvement in estimation accuracy.

The discussion above was presented in the earlier example in Figure 41 (in section 5.2). In summary, the periodogram displayed on the left was evaluated using the Fourier Transform of the entire waveform, while the periodogram shown on the right used the Welch procedure which divided the waveform into thirty-two overlapping segments with Fourier transform applied to each before the resulting spectra were combined by averaging. As discussed earlier, the periodogram produced from the segmented and averaged data is much smoother, giving a significantly better estimate of the broadband feature of the (noise) spectrum, but the loss in the frequency resolution is clear, as the 128Hz sine wave is barely visible.

[7] Sidelobe related to the spread of energy at frequencies that are not present in the original/input signal due to the data truncation outside the window.

5.2.2. Modern Spectral Estimation Methods

As described in the preceding section, classical techniques to compute the power spectra are all based on the Fourier transform and require few assumptions on the origin or nature of the data. In particular, nonparametric power spectrum estimation methods as exemplified by the `pwelch` routine in Matlab (MathWorks, 2016) are often adopted, where some knowledge of the data could be useful for window selection and (importantly) averaging strategies. In particular, since the signal outside the data window is implicitly assumed to be zero, this can often lead to distortion in the resulting estimate (Marple, 1987). Additionally, there are also distortions due to the various data windowing functions designed for truncated Fourier analysis, (for example rectangle, Hamming, Blackman-Harris), each of which inevitably produces its own unique artefact.

Modern spectral estimation methods are designed to overcome some of the above shortcomings and are particularly effective when the data segments to be analysed are relatively short. Broadly, these methods fall into two classes: parametric and nonparametric, described as follows.

Parametric or model-based techniques are commonly used when something is known or can be assumed about the original signal data/source. They are constructed to eliminate the need for windowing and thus can improve spectral fidelity and/or resolution, particularly when the data contain a considerable amount of noise. Specifically, to overcome the resolution problem (described in section 5.2.1) common to most nonparametric methods, parametric methods are devised with a statistical model that operates on some unknown parameters, with the goal to increase resolution by estimating the parameters from the data at the cost of higher computational cost or complexity. Technically, these models are formulated using an autoregressive (AR) approach, which assumes the signal can be modelled as the output of an autoregressive filter (Hayes, 1996), such as an IIR (Infinite Impulse Response) filter, driven by a white noise sequence. By solving for the filter/IIR coefficients, the resulting power spectrum can easily be determined. However, the model order, or a number of taps, must first be determined. Generally, if the model order is too small, the spectrum will be highly smoothed, and thus lack resolution. If the model order is too high, false peaks from a large number

of poles begin to appear. Moreover, since most AR techniques are based on linear prediction, which is what has been used to extrapolate the signal outside of its known values, they do not suffer from sidelobe problems due to the choice of a window function as required by the Welch method discussed earlier in section 5.2.1. As a result, parametric methods such as the *Yule-Walker* model (described later) are good estimators for narrowband signals with moderate-to-high SNR (Hayes, 1996).

In general, any improvement in resolution and fidelity will depend strongly on the appropriateness of the model selected. This could be a major strength as such approaches afford increased flexibility in design, especially when either the shape of the estimated spectra and/or the some knowledge of the process generating the data are known *a priori*. However, as there are many metrics developed for model order selection, the choice of an appropriate model could be a challenging task that might depend on subjective judgement. More importantly, a major criticism of parametric spectral estimation methods is that they make use of a linear process, commonly referred to a model, to estimate the power spectrum (Marple, 1987).

Non parametric spectral analysis methods as exemplified by *Pisarenko Harmonic Decomposition* (PHD) (Pisarenko, 1973; Kay, 1999), and Multiple Signal Classification (MUSIC) procedures (Schmidt, 1986) are based on the so-called *subspace decomposition* technique, which separates the data into signal and noise subspace by exploiting the orthogonality between the noise subspace and the signal subspace eigenvectors to produce a *pseudospectrum*. As the latter suggests, these procedures may not yield a true PSD estimate, in that (i) the power is most likely not conserved and, likewise, (ii) the computed amplitudes between spectral components are relative. Using the eigenanalysis based frequency estimation technique (described in section 5.3) these procedures are commonly known to offer a better resolution (also known as 'super-resolution' in some literature) and frequency estimation characteristics, especially at high noise levels (Stein, 2000; Marvasti *et al.*, 2012). By applying principal component analysis on the autocorrelation sequence (R_{xx}) computed for the concerned signal (whose PSD is to be determined) the basic idea is to separate correlated and

uncorrelated signal components using an algebraic decomposition method termed eigenvalue decomposition. As with the SSA procedure discussed in chapter 3, such a decomposition technique is particularly effective in separating highly correlated signal components such as sinusoidal, exponential, or other narrowband processes from uncorrelated white noise. Thus, when highly correlated signal components are involved, the method can eliminate much of the uncorrelated noise contribution.

From a signal processing viewpoint, it should be noted that a direct approach to estimate the signal subspace (as complex exponentials mixture) is of limited value in terms of frequency/PSD estimation, as it requires that the autocorrelation matrix is known exactly. Instead, practical methods including the PHD and MUSIC procedures make use of the noise subspace whereby the smallest eigenvalue (σ^2) of R_{xx} and the corresponding eigenvector (ν) are computed. As such, these procedures may not be very good at separating noise from broadband processes, as signal/components generated by these processes are somewhat uncorrelated. Furthermore, as with the parametric or model-based methods (described above), neither of the two procedures offers a true PSD estimate of the signals of interest, since they may not conserve the power/energy between spectral components.

5.3. Eigenanalysis Frequency Estimation of the Pyloric Rhythm

To facilitate determination of the pyloric rhythm directly from the noisy optical recordings of bath dyed neuronal cells in the STG, the power spectrum is estimated for the signals ensemble collated at the neuropil as in the previous studies. Here, the eigenanalysis frequency estimation approach is adopted to afford the estimator constructed the best resolution, taking into account the potential distortions by the classical (Fourier-based) spectral analysis methods in light of the demonstrably low SNR of the data/signals captured by the optical recordings (dos Santos *et al.*, 2017). As discussed in section 5.2.2, the principal goal of the eigenanalysis approaches seeks to divide the information

contained in a recording into two subspaces: namely, a (correlated) signal subspace and (uncorrelated) noise subspace. The inherent eigendecomposition procedure transforms the original signal/data where its components, termed eigenvectors, are ordered in descending order of their energy. Here, as with the SSA discussed previously (in section 2.2.8), a decomposition procedure computes the energy of each component in terms of its variance, or the component's eigenvalue as described in the literature (see JOC/EFR ©, 2001). Importantly, as these transformed components are orthonormal and (thus) scaled to a variance of one, the technique is known to produce only a so-called *pseudospectrum* estimate because the resulting (PSD) estimate does not preserve signal power and, instead, determines spectra in relative units. As such, it is not considered to be a true spectral estimator and, hence, commonly known as a frequency estimator (Stein, 2000). Using the eigendecomposition based frequency estimation procedure, it should be apparent that the influence of noise could be completely removed, provided that the (uncorrelated) noise subspace components are not included in estimating the signal spectrum, (thus) allowing the remaining components in the signal subspace to be evaluated by means of the classical theory of Fourier analysis. Importantly, this noise removal approach is completely at one with the previously developed SSA procedure for signal extraction, whereby the pyloric rhythm and its harmonics are computed accurately, allowing the estimation for the duty cycle of the relevant spike/waveform.

The adopted pseudospectrum estimator is constructed with the MUSIC (Multiple Signal Classification) algorithm which was originally designed for high-resolution source direction estimation in the context of array processing (Schmidt, 1986; Marvasti *et al.*, 2012). The algorithm subsequently extended the well-known Pisarenko Harmonic Decomposition (PHD) method specifically developed for pseudospectrum estimation in the presence of additive white noises (Pisarenko, 1973; Stein, 2000). As such, both methods compute the noise subspace, with the assumption that the signal and noise subspaces are orthogonal in the decomposed form; in other words, in principle, the estimate of the noise subspace will be zero wherever a signal is present. However, the two methods differ in the way of how the noise subspace is determined.

Computationally, the PHD constructs the autocorrelation matrix (R_{xx}) of dimension p + 1, with p specifying expected number of sinusoids (or subspace dimension), under the simple assumption that its smallest eigenvalue (σ^2) belongs to the noise subspace. On the other hand, the MUSIC algorithm generalises such an assumption by using a noise subspace of dimension greater than one to achieve an improved and (statistically) more reliable signal/estimator. Mathematically, the method evaluates the noise subspace by locating the 'zeros' in the estimator equation (29):

$$P_{MUSIC}(f) = \frac{1}{\sum_{k=p+1}^{N} \left| v_k^H e(f) \right|^2} \tag{29}$$

where *N* is the dimension of the eigenvectors and v_k^H is the k-th Hermitian transpose of the eigenvector of the correlation matrix. The integer *p* is the dimension of the signal subspace (as described above), so the eigenvectors v_k used in the sum correspond to the smallest eigenvalues that span the noise subspace. The vector $e(f)$ consists of complex exponentials at frequency f, so the inner product $v_k^H e(f)$ amounts to a Fourier transform that is computed for each v_k and then the squared magnitudes are summed (MathWorks 2018). A detailed mathematical treatment, in addition to the description of a pseudo code for the MUSIC algorithms can be found in Marvasti *et al.* (2012).

To illustrate the above, a MATLAB implementation of the MUSIC algorithm, the `pmusic` function (MathWorks, 2016), is used to determine the pyloric frequency for one of the optical recording datasets published in dos Santos, Andras and Lam, (2017a). The results are presented in Figure 42.

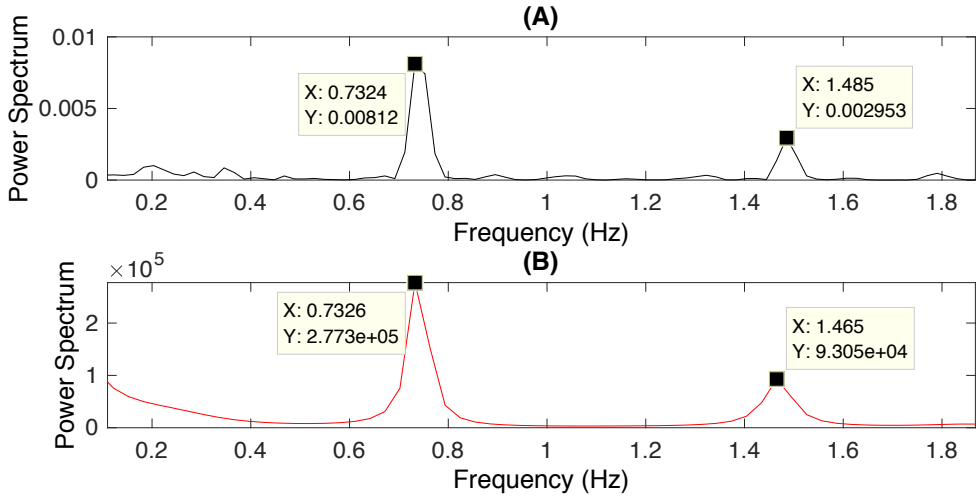

Figure 42 – Spectra obtained for the neuropil (cell 17) identified in an earlier study published in dos Santos, Andras and Lam (2017a). (A) The raw frequency spectrum displayed in a (Welch) periodogram obtained with no windowing and non-overlapping segments, SNR -10.444dB. (B) The pseudo spectrum produced by the MUSIC estimator, where the pyloric frequency (0.7326 Hz), alongside the 2nd harmonic, is shown; (p=896) SNR -11.0136 dB. Note: The SNR computed in (B) is indicative only.

It should be noted in Figure 42(B) that the parameter *p*, denoted as the signal subspace dimension as described earlier, was chosen empirically. In practice, it can be determined from the data using, for example, one of the most well-known model/order selection techniques of the Minimum Description Length (MDL), which has been reported to provide both consistent and reliable results (Wax and Kailath, 1985; Marvasti *et al.*, 2012).

5.4. Experiments and Methods

The experimental procedures used for dissection, imaging and data collection were the same as already described in sections 3.2.2, 3.2.4 and 3.2.5 respectively. The objectives, alongside their reasoning of the data analysis method, were described in section 5.1 and explained in sections 5.2 and 5.3 above. Essentially, the principal task is to investigate an automated procedure, which will facilitate a reliable determination of the pyloric frequency from the VSDI/optical data recorded for the bath dyed STG sample. As such, the algorithm constructed is based on modern spectral

estimation methods, which analyse the frequency content of the data/signals captured from the dye bath. This facilitates determining the operating parameters of the previously developed s-SSA procedure as discussed in chapter 3, with little or no manual adjustments and thus without further recourse to analysing the activities monitored on the lvn.

Three datasets including both optical (dye bath) and electrophysiological (lvn) recordings of the respective STG samples were selected from experiments developed in previous studies, to enable further examinations of the techniques presented in section 5.3. These datasets were chosen specifically with reference to the SNR achieved for each experiment, facilitating informative performance evaluation of the spectral estimation techniques described so far. In particular, the techniques evaluated include the classical approach of Welch's modified periodogram and the autocorrelation (AR) model based Yule-Walker Equation (Hayes, 1996; Stein, 2000). In addition to providing comparative benchmarks for the MUSIC algorithm, the former is known to improve upon the classical periodogram approach at relatively low computational complexity, by addressing the lack of the ensemble averaging that is present in the 'true' PSD formula. The latter, also known as the autocorrelation method, represents a special case of the least squares method where the complete error residuals can be efficiently utilised. As in the preceding section (5.3), the raw power spectrum is also computed to provide a reference benchmark in each test/study. The results are summarised and presented in Figure 43 to Figure 45 below.

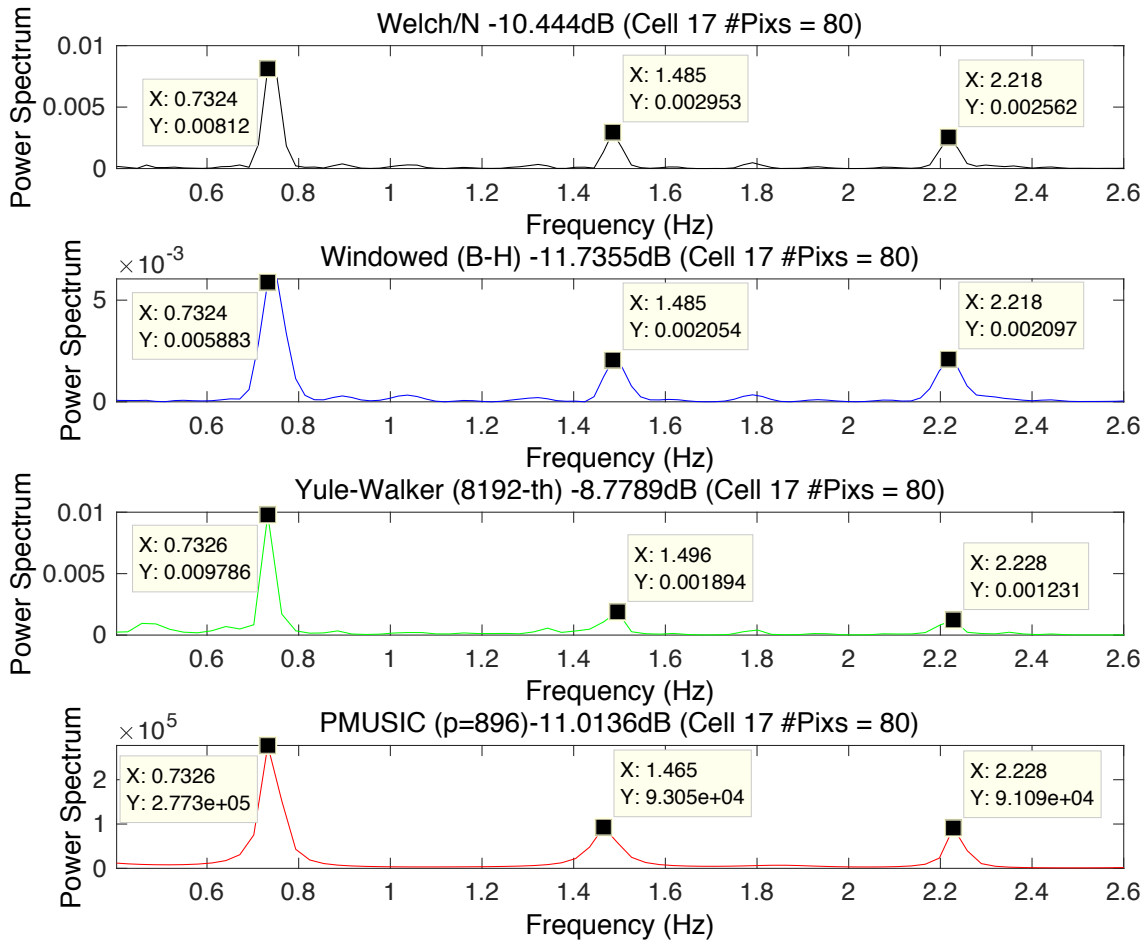

Figure 43 – Spectra obtained using various spectral estimators for the neuropil (cell 17) identified in the optical recording of the STG sample. From top to bottom: The raw frequency spectrum displayed in a (Welch) periodogram obtained with no windowing and non-overlapping segment, Modified periodogram (Welch) with Blackman-Harris windowing (better background noise estimation), AR/model based estimator with Yule-Walker Equation (model order = 8192), and pseudospectrum estimated using the MUSIC algorithm, where the pyloric frequency (0.7326Hz), alongside the 2nd harmonic, is shown. For the MUSIC algorithm, the computed SNR is indicative only.

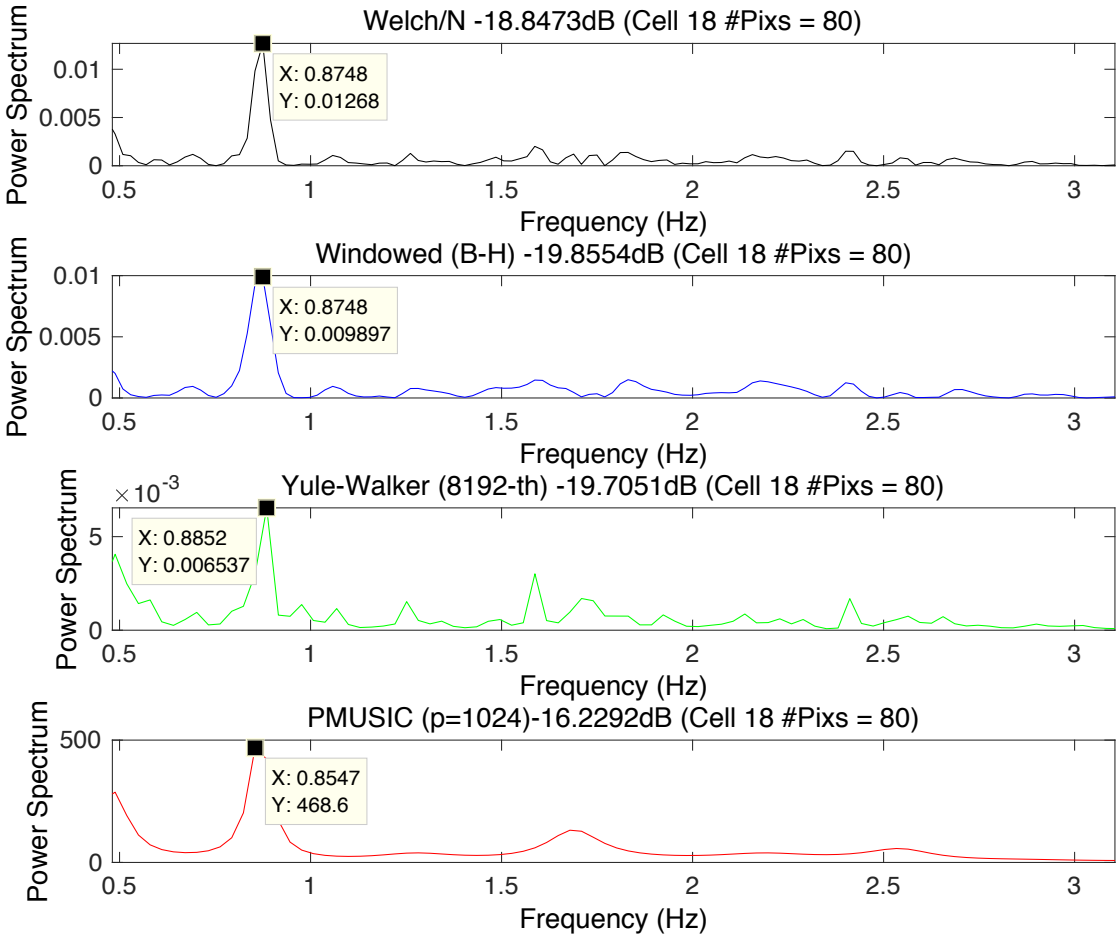

Figure 44 – Spectra obtained using various spectral estimators for the neuropil (cell 18) identified in the optical recording of the STG sample. From top to bottom: The raw frequency spectrum displayed in a (Welch) periodogram obtained with no windowing and non-overlapping segment, Modified periodogram (Welch) with Blackman-Harris windowing (better background noise estimation), AR/model based estimator with Yule-Walker Equation (model order = 8192), and pseudospectrum estimated using the MUSIC algorithm, where the pyloric frequency was estimated at 0.8547Hz and appeared to be different from that obtained by the classical periodogram approaches and the Yule-Walker AR model. In all cases, the absence of the 2nd harmonic is also apparent given the demonstrably poor/low SNR, except the MUSIC algorithm.

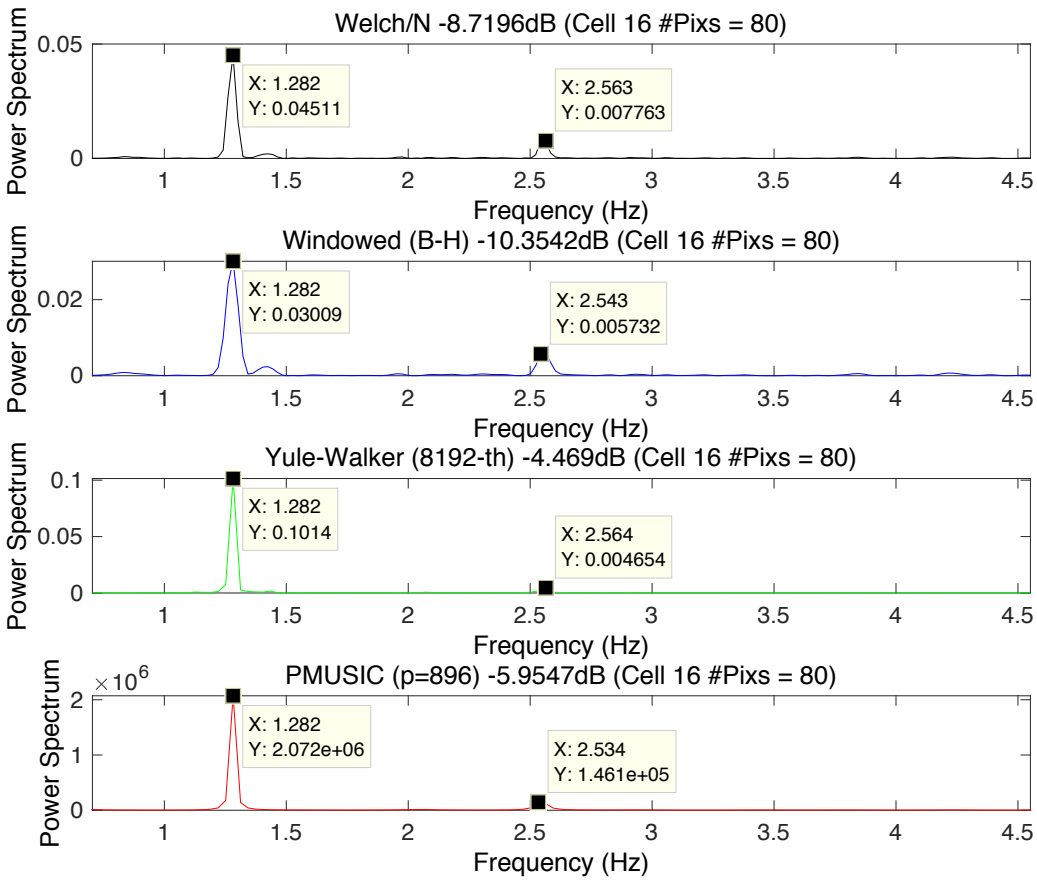

Figure 45 – Spectra obtained using various spectral estimators for the neuropil (cell 16) identified in the optical recording of the STG sample. From top to bottom: The raw frequency spectrum displayed in a (Welch) periodogram obtained with no windowing and non-overlapping segment, Modified periodogram (Welch) with Blackman-Harris windowing (better background noise estimation), AR/model based estimator with Yule-Walker Equation (model order = 8192), and pseudospectrum estimated using the MUSIC algorithm, where the pyloric frequency (1.282Hz), alongside the 2nd harmonic, is shown. For the MUSIC algorithm, the computed SNR is indicative only.

The results shown in Figure 43 to Figure 45 highlight the following points. First, the MUSIC algorithm worked well in determining the pyloric frequency over a considerable range of low SNRs that varied between -20dB to -9dB. In each case, the pyloric frequency was shown as the dominant peak in the estimated PSD within the documented range of 0.5Hz – 2Hz for the pyloric rhythm (see section 2.1.4). As such, the peak can be determined easily from the estimated PSD using, for example, the readily available MATLAB® functions such as `findpeaks` and `localmax` (MathWorks 2016). Additionally, this process could further be aided by the Statistics and Machine

Learning Toolbox (MathWorks 2018). The latter supports well documented statistical tests for signal/distributions including, for example, `kstest`, `lillietest` and `jbtest`, *etc*., enabling hypothesis tests to be constructed to determine whether a signal/distribution is just white/noise (or otherwise) in accordance with a user-defined confidence level.

Lastly, as noted in Figure 44, the estimated frequency of 0.8547Hz by the MUSIC algorithm appeared to be different from that obtained by the other methods, particularly the reference benchmark which was calculated as 0.8748Hz. However, a detailed analysis of these results revealed that, as the frequency 'bin' sizes used by the two methods is different (namely, 0.0203Hz and 0.0305Hz for the reference benchmark and MUSIC algorithm respectively), the two estimates would fall into the same bin following a simple realignment/calculation. Second, the operating parameter *p*, specified as the signal subspace dimension of the MUSIC algorithm, should be revised (upward) in accordance with the (decreased) SNR of the data set. This is as expected given the inherent MUSIC data model does allow noise to appear in the signal subspace (although the reverse is not true). In fact, to ensure orthogonality between the signal and noise subspaces, the MUSIC algorithm estimates the spectral content of the signal at frequency ω, by projecting the normalised vector, $\mathbf{e}(\omega) = |1, e^{j\omega}, \dots, e^{j(m-1)\omega}|$, where m is the dimension of the autocovariance matrix, into the noise subspace that exists primarily but not exclusively in the lower dimension corresponding to smaller σ^2 – see equations 55 to 57 in Marvasti *et al.* (2012). Third, the PSD estimates obtained by the Yule-Walker model worked well with moderately low SNRs (~-10dB) but, expectedly, the model broke down when the noise level was high as is evident by the very low SNR (~-20B) shown in Figure 44.

5.5. Results and Discussion

As described in the preceding section, three datasets were selected from over 40 experimental studies. These were chosen to cover a wide range of pyloric frequencies and, crucially, a spread of

SNR obtained within the dataset. The results are displayed in Table 5 to Table 7. In all tables, the columns are as follows: ROI = Cell/region of interest identified, #NP = Number of pixels in the ROI, f1 = Main/peak frequency detected (Hz), f2 = Second main/peak frequency (Hz), SNR = Signal-to-Noise Ratio (dB), R_{21} and R_{31} = Ratios of the second harmonic to the first, and third harmonic to the first, respectively, and DC_{21} and DC_{31} = The corresponding duty cycle (x/100).

As discussed, the basis for determining the pyloric frequency was described in detail in the earlier sections of this chapter – particularly in sections 5.2 and 5.3, where the foundation was discussed for developing a PSD estimator that would lead to an automated determination of the pyloric frequency as demonstrated in section 5.4. Here, it should be noted that the raw power spectrum was also used in conjune with the MUSIC algorithm, to facilitate determining the exact value of the pyloric frequency. The reasons are twofold: first, the MUSIC method is a pseudospectrum estimator that calculates spectra in relative units; second, and relatedly, the frequency resolution of resulting spectra may not be translated easily to that adopted by other PSD estimators, as is evident by the different frequency bin sizes allocated for the periodogram as described in section 5.4. In light of this, the traditional periodogram, which generates the raw PSD, was used to help determine the exact pyloric frequency, with the added advantage that the results generated would be directly comparable to that produced and/or published previously thus far. In other words, the results presented below in Table 5 to Table 7 have the pyloric frequencies estimated as 0.7324Hz, 0.8748Hz and 1.282Hz respectively. See also Figure 43 to Figure 45 depicted in the previous section.

Following the automated estimation of the pyloric frequency, as described above, the optically recorded data from the bath dyed STG sample were processed separately from the extracellular recording of triphasic pyloric activity/pattern monitored on the lvn. This entails the following tasks:

i) The multiresolution procedure described in dos Santos, Andras and Lam (2017a) was applied to the individually demarcated ROIs in order for the relevant signal sub/components of the pyloric rhythm, if present, to be accurately extracted. Further, the signal components bearing the first and second harmonics of the pyloric frequency must also be isolated, to enable

estimation of the duty cycle and thus identification of the participating pyloric neurons (dos Santos, Andras and Lam, 2017b).

ii) For the extracellularly captured data on the lvn, the primary task is to separate the individual phase of the pyloric rhythm from each computed pyloric cycle, in accordance with the spiking/activity pattern characteristic of the respective participating neuron. Here, the spontaneous and characteristic motor pattern consisting of the highly synchronised activity of the PD-timed, LP-timed or PY-timed neurons were analysed and segmented using a conventional wavelet-based multiresolution procedure which enables the deconstruction of regular and predictable phasing of the pyloric activities.

iii) To expand the work previously described in dos Santos, Andras and Lam (2017b) this study incorporates the duty cycles of the PD and LP phases of the pyloric rhythm, as well as the PY neurons. This was achieved by the use of segmentation of the highly structured phasing of the pyloric rhythm. The segmentation was using the PY neurons, and quiescent phases of the pyloric rhythm monitored on the lvn – the start and end point of the triphasic patterns – see description in dos Santos *et al.* (2017).

To facilitate studying the results in Table 5 to Table 7 below, grey highlighting was used in each table to indicate the ROIs that display the pyloric frequency as either the first or second major frequency noted in the power spectrum. Further, as mentioned at the beginning of this section, the last two columns of each table were also supplied with the ratio of harmonics, denoted as RH_{21} and RH_{31} as in earlier work (dos Santos, Andras and Lam, 2017b) and, correspondingly, the computed % duty cycle/100 (DC) (included in brackets) which was explained earlier in section 2.2.2. The latter, alongside the estimated pyloric frequency from the neuropil of the STG sample, were calculated using individual participating neurons modelled on the lvn and are given as DC(PD), DC(LP) and DC(PY) respectively in the table header/title for easy reference.

For comparison, the results incorporated in Table 5 below were obtained using the same data set analysed previously in chapter 3 (Table 3 in section 3.4).

Table 5 – Known set. PR= 0.7324HZ: DC(PD) = 0.123, DC(LP) = 0.328, DC(PY) = 0.384.

ROI	#NP	Feq_1 (Hz)	Feq_2 (Hz)	SNR (dB)	RH_{21} (DC_{21})	RH_{31} (DC_{31})
1	18	0.8748	0.7324	-31.01	1.9100 (0.10)	4.3400 (0.10)
2	44	0.7528	0.7324	-18.19	0.4600 (0.26)	0.0080 (0.36)
3	14	0.7528	0.7324	-19.14	0.4200 (0.28)	0.0620 (0.42)
4	16	0.8748	n/a	-27.78	0.0014 (0.49)	0.9900 (0.10)
5	37	0.7324	n/a	-12.29	0.0540 (0.43)	0.1400 (0.24)
6	29	0.7324	0.7000	-22.05	0.0190 (0.46)	0.6200 (0.13)
7	33	0.7528	0.7324	-20.03	0.1400 (0.38)	0.1960 (0.22)
8	16	0.7324	0.8748	-22.87	0.1140 (0.39)	0.4200 (0.17)
9	20	0.8952	0.7324	-24.97	0.3850 (0.29)	0.2400 (0.21)
10	17	0.7324	n/a	-9.410	0.0190 (0.46)	0.0400 (0.40)
11	23	0.8956	n/a	-26.35	1.0700 (0.10)	0.6000 (0.14)
12	33	0.8956	n/a	-29.70	1.7500 (0.10)	2.1200 (0.10)
13	19	0.7324	n/a	-14.73	0.1100 (0.39)	0.0560 (0.41)
14	24	0.7324	n/a	-18.99	0.0540 (0.43)	0.1470 (0.24)
15	32	0.7528	0.7324	-12.24	0.1870 (0.36)	0.1500 (0.24)
16	12	0.8952	n/a	-24.08	0.0670 (0.42)	0.1600 (0.23)

As discussed earlier, the pyloric frequency for this dataset was estimated as 0.7324Hz. Additionally, the DCs for the PD, LP and PY neurons are also given as 0.123, 0.328 and 0.384, respectively. The following points are noted: first, the most apparent observation is that the pyloric frequency was noted in cell 8 (ROI 8), which was omitted in the earlier work presented in chapter 3. A further investigation of this 'anomaly' has revealed that, however, the results presented here included only dominant frequencies that lay in the range between 0.5 and 2.0Hz that are typical of the pyloric neurons and hence the 2.7060Hz reported previously in dos Santos, Andras and Lam (2017a) was omitted there. Furthermore, the relatively poor SNR achievable for this cell (-22.87 dB) has resulted in the different estimates for the DCs in light of the computed RHs obtained from the computed periodogram/PSD for this cell. Second, where the pyloric frequency was detected from the individual cells in this study, the differences in SNR achieved were practically the same as previously obtained – for example cells 2, 5, 10, 13 and 15 (five out of the eight cells with cell/ROI 8 included). The reverse is true for cell/ROIs where the pyloric frequency is absent, as the computed SNR for the individual cell is much lower in this study than that obtained previously. This is perfectly understandable as the lower than average SNRs (<-5dB below the ~-22dB average) obtained in this

study are indicative of the rather 'noisy' PSD directly estimated from the raw spectrum from which the power at the pyloric frequency was calculated. Further, as with cell 8 described above, the DC calculated for these cells/ROIs are inconsistent (for example cell 9) and, in some cases, 'unrealistic' (for example 10% or 0.1 for cell 1). Third, where the SNR is high (better than -20dB) further investigation of the concerned PSD estimates has revealed that, in general, the pyloric frequency is readily detectable as a sharp peak by the MUSIC PSD estimator and, likewise, observable in the reference periodogram. Conversely, when SNR is low or poor, the peak detection is also poor and often erroneous.

A further analysis similar to the above was performed with two blind data sets (Blind-set 1 and 2). The results are collated and summarised in Table 6 and Table 7 respectively.

Table 6 – Blind data set 1. PR= 0.8748HZ: DC(PD) = 0.128, DC(LP) = 0.156, DC(PY) = 0.347.

ROI	#NP	Feq_1 (Hz)	Feq_2 (Hz)	SNR (dB)	RH_{21} (DC_{21})	RH_{31} (DC_{31})
1	16	0.8748	0.6917	-28.99	0.0377 (0.44)	0.0700 (0.43)
2	12	0.7121	n/a	-37.61	1.2500 (0.10)	0.1700 (0.23)
3	12	0.8454	n/a	-32.95	0.0320 (0.44)	0.3000 (0.20)
4	18	0.8748	n/a	-34.32	0.4500 (0.27)	0.3000 (0.20)
5	16	0.9359	n/a	-43.61	1.0600 (0.10)	1.6600 (0.10)
6	32	0.6917	n/a	-36.08	0.7310 (0.17)	0.2500 (0.21)
7	19	0.6714	n/a	-37.04	0.0440 (0.43)	0.0980 (0.46)
8	20	0.7121	n/a	-35.65	0.3900 (0.28)	0.7300 (0.11)
9	22	0.8545	n/a	-31.57	0.0350 (0.44)	0.1800 (0.23)
10	19	0.6917	n/a	-35.97	0.0090 (0.47)	0.0660 (0.42)
11	20	0.6917	0.8748	-32.37	0.3890 (0.29)	0.2400 (0.21)
12	16	0.6917	n/a	-37.03	0.5990 (0.21)	0.6900 (0.12)
13	24	0.8545	n/a	-32.16	0.3460 (0.30)	0.0450 (0.40)
14	21	0.7121	n/a	-43.32	4.3100 (0.10)	0.4110 (0.17)
15	26	0.8545	n/a	-39.17	2.1100 (0.10)	0.5500 (0.14)
16	15	0.6914	n/a	-37.40	1.6200 (0.10)	0.0078 (0.31)
17	17	0.7121	n/a	-51.14	4.8400 (0.10)	9.1600 (0.10)

As demonstrated in Figure 44 (section 5.4), Table 6 represents one of the noisiest datasets, with SNR calculated at ~-20dB for the neuropil. Indeed, the pyloric rhythm (estimated at 0.8748Hz) was found in only two cells/ROIs (1 & 4) as the dominant frequency in the estimated PSD, with consistently low SNRs, while the same frequency was also detected in cell/ROI 11 as the second

largest peak appearing in the corresponding PSD. Further, it is also noted that considerable variability in the SNR existed across the individual ROIs, spread between -51dB to -29dB, with a noticeably low average SNR of -36dB. Closer examination of the power spectra obtained across the dataset reveals that much of noise/power was localised in the very low end of the frequency spectrum, (well) below the computed pyloric rhythm (which is also validated by the accompanying lvn recording). However, this could have a range of explanations, which needed to be understood with a view to obtaining greater consistency, and hence improved performance.

Table 7 – Blind data set 2. PR= 1.282HZ: DC(PD)=0.182, DC(LP)=0.188, DC(PY)=0.268.

ROI	#NP	Feq_1 (Hz)	Feq_2 (Hz)	SNR (dB)	RH_{21} (DC_{21})	RH_{31} (DC_{31})
1	15	1.404	1.282	-23.25	0.0560 (0.42)	0.0200 (0.30)
2	14	1.282	1.424	-19.97	0.3500 (0.30)	0.0600 (0.27)
3	14	1.404	n/a	-31.79	3.7000 (0.10)	1.8600 (0.10)
4	11	1.404	n/a	-28.83	0.8220 (0.14)	0.1900 (0.23)
5	14	1.282	n/a	-11.44	0.1280 (0.38)	0.0500 (0.40)
6	14	1.282	1.404	-19.68	0.1260 (0.39)	0.1500 (0.24)
7	16	1.424	1.282	-24.52	0.0780 (0.41)	0.0700 (0.42)
8	23	1.404	n/a	-32.14	0.4560 (0.26)	1.6100 (0.10)
9	20	1.404	n/a	-34.43	0.5700 (0.23)	0.6500 (0.13)
10	9	1.424	n/a	-35.83	0.6800 (0.19)	0.2000 (0.23)
11	13	1.282	n/a	-16.24	0.1200 (0.39)	0.0100 (0.32)
12	13	1.282	n/a	-12.18	0.2500 (0.33)	0.0100 (0.31)
13	13	1.282	n/a	-12.08	0.1200 (0.38)	0.0100 (0.29)
14	15	1.404	n/a	-31.42	0.2100 (0.35)	0.5000 (0.16)
15	16	1.383	n/a	-24.89	0.1000 (0.40)	0.2100 (0.22)

In contrast to the results presented in Table 6, in Table 7 the pyloric frequency estimated for the neuropil has a relatively high SNR (at ~-9dB) – see Figure 45 in section 5.4. Here, it is noted that the pyloric frequency (estimated at 1.282Hz) was present in just under half (= 7 in total) of the identified cells/ROIs as either the dominant/first peak (a majority of 6 cells) or the second largest peak in the estimated PSD. For cells 5 and 12, for example, the corresponding SNRs are relatively high, with closely agreed estimates of the corresponding DCs achieved by the two RHs – DC_{21} and DC_{31}. On the contrary, the DCs estimated by the computed RHs for the other cells are disparate, particularly where the SNR achieved is comparatively lower – for example cells 6 and 11. Contrastingly, for cells 1

and 7, the SNRs achieved are significantly poorer and stood at or below -23dB. For cell 1, the disparity shown by the two estimated DCs based on the respective RHs is evident, while the two DCs estimated for cell 7 were surprisingly consistent. Coupled with the demonstrable variability in the SNR shown across these cells/ROIs, this makes it difficult, if not impossible, to map these cells onto the individual pyloric neurons. In this respect, the work presented in dos Santos, Andras and Lam (2017b) could be used to achieve such mapping (see example below).

Lastly, it should be noted that the PY neuron has the longest duty cycle and is, therefore, the easiest to distinguish by means of the ratio. This is not evident in this case, however, as the DC for the PY neuron as shown in Table 7 was significantly smaller (27%) when compared with that shown in Table 5 and Table 6 (> 35%). Interestingly, moreover, and counter to general belief[8], it was noted that the relationship between the LP and PD duty cycles could be variable as is evidenced between the results obtained here and those shown earlier in Table 5 and Table 6.

From the results presented in the above tables, the following points are noted:

1. In most cases, the SNR obtained for the neuropil initially played an important part in the accurate determination of the pyloric frequency; if present, the pyloric frequency was readily observable as a peak shown within the power spectrum generated by the MUSIC algorithm, where the SNR computed in the reference periodogram is better than ~-20dB. When SNR is low (<-20dB), the peak detection is poor in both PSD estimates and often erroneous, especially where there might be other neighbouring peaks, which could be attributed to noise and/or other narrowband processes. The latter appeared to be true in general; that is when the SNR is poor – under ≈-20dB – the number of cells/ROIs where the pyloric rhythm could be detected reliably (in statistical terms) was also low.
2. The effect of the computed SNR on the respective DCs estimated by computing RH_{21} and RH_{31} in the reference periodogram was also apparent. In particular, the two estimated DCs, DC_{21}

[8] Generally, PD neurons have a larger DC than LP neurons in control studies (Rabbah and Nadim, 2005).

and DC_{31} were generally in good agreement (or consistent) when the SNR was relatively good/higher. For similar reasons, moreover, RH_{21} was generally considered to be a more reliable ratio, as the second harmonic for most of the periodic waveforms was generally (much) larger in amplitude than the third harmonic in the spectra obtained and, therefore, less prone to noise.

3. The DCs computed for the respective pyloric neurons by modelling the triphasic pyloric rhythm captured on the lvn should only be used as a guide. The reasons are two-fold. Firstly, the deconstruction or separation of triphasic pyloric rhythm as a monitor on the lvn is a computationally exacting task that often requires minor manual adjustments and sometimes trials and errors (dos Santos, Andras and Lam, 2017b). Secondly, the quality of the electrophysiological recordings of the lvn can also vary – see Figure 46 below for an example. This would inevitably impact adversely on the accuracy of the deconstruction-reconstruction of the triphasic pyloric rhythm on the lvn and, similarly, the quality of the resulting mappings of the pyloric rhythm extracted from the bath dyed STG sample onto the respective phases/activities monitored by the lvn**.**

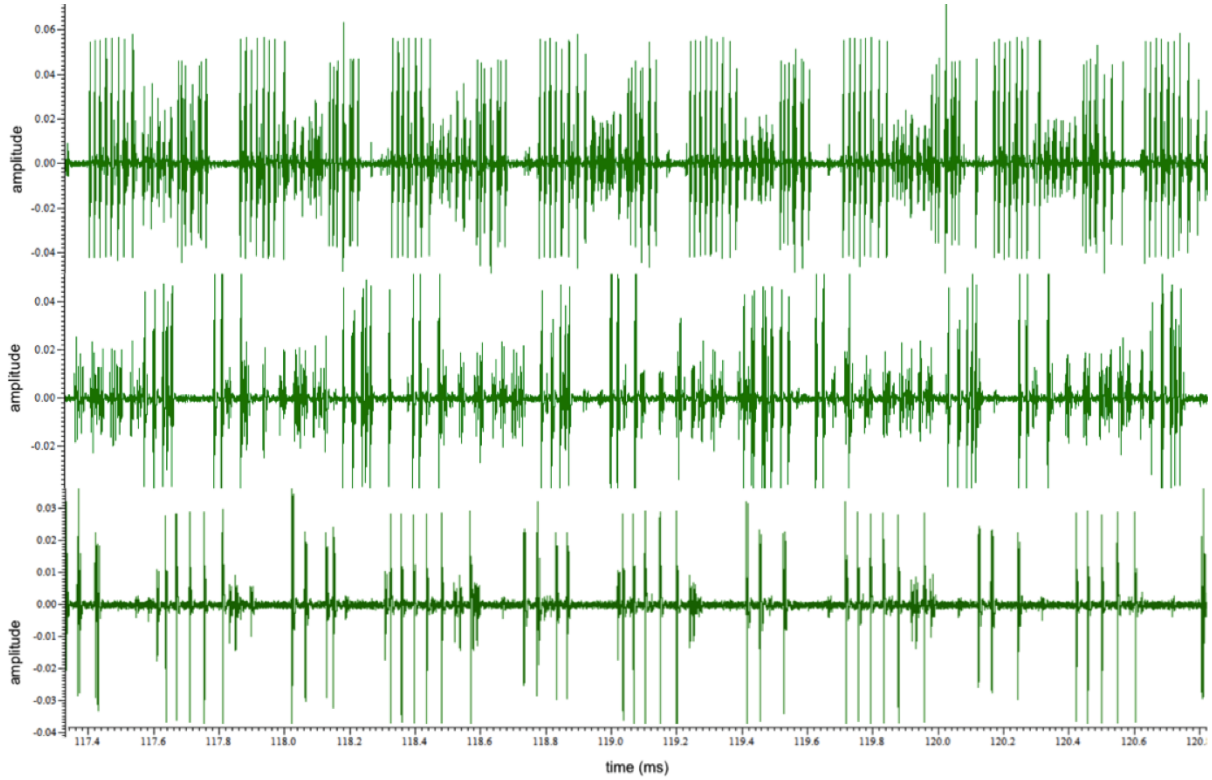

Figure 46 – Three lvn recordings in experiments, where it can be observed the different strength of the rhythms which might occur due to such external factors as the STG sample dissection and saline temperature, etc. Analytically, the variable quality of the recordings may affect the respective triphasic pyloric rhythms and relatedly, the duty cycles (DC) of the individual pyloric phase measured on the lvn in each experiment.

In passing, it was noted that, across the three datasets, the PY neuron had the longest estimated duty cycle amongst all the pyloric neurons and, therefore, was the easiest to distinguish by means of the ratio. This is in agreement with most of the literature reviews and other studies on the subject, for example (Zhu, Selverston and Ayers, 2016). Interestingly, and counter to general belief, it was noted that the relationship between the LP and PD duty cycles is DC(LP) ≈ DC(PD) between Table 5 and Table 7 and DC(LP) > DC(LP) evidenced in Table 6 and Table 7.

As a final note, it should be added that, in light of these results, the main limitation of the methodology described in this chapter is the fact that the duty cycle (DC) on its own is not, as yet, sufficiently discernible to automatically determine the neuronal type in the pyloric circuit. However, subject to the quality of the dataset measured in terms of the SNR, the pyloric frequency estimators studied here were able to detect and determine the pyloric frequency directly from the optical

recordings of bath dyed neuronal cells, with moderate to high noise levels. As a result, this obviates the need for extracellular recording from which the initial manual enumeration of the pyloric cycles is obtained, to facilitate determination of the window length parameter required by the SSA procedure (described in chapter 3). To determine the neuronal types of the individual cells/ROIs based on the optical recordings of the bath dyed STG sample, we implemented the methodology described in chapter 4. In essence, the highly synchronised activity of the PD-timed, LP-timed and PY-timed neurons monitored on the lvn were analysed and segmented to facilitate computation of their respective phase of each of these neurons, allowing the subsequent mapping of the individual neuron onto the STG sample based on the pyloric rhythm extract from the optical recordings. This is illustrated in the example below.

Figure 47 shows the instantaneous phase matching technique developed in dos Santos, Andras and Lam (2017b) to estimate from the respective Hilbert spectra the time delay between the optical and lvn recordings. Here, it can be shown that the time lag between cell 3 (Figure 38) and the lvn maintains a practically constant mean phase shift of -3.334 radians, with a standard deviation of 0.225 radians.

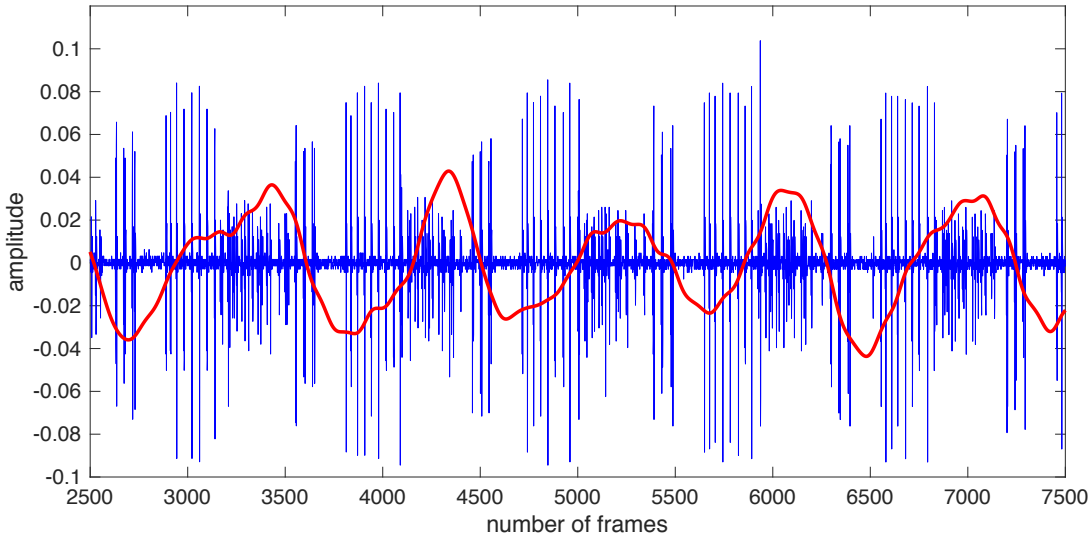

Figure 47 – The pyloric rhythm (red) extracted from cell 3 (Figure 38), time delayed to match with the identified PY neuron phase overlaid on the lvn (blue), using the combination of the first and second harmonics.

5.6. Summary

Integrating the data obtained from optical VSDI and electrophysiological recording of the lvn is a complex and exacting task that often requires trials and errors and thus minor manual adjustments. As discussed in earlier chapters, in particular the determination of the window length *L* for which the multiresolution (s-SSA) procedure and, in no smaller part, the number of relevant components to be selected from the scree plot, also required *a priori* knowledge acquired from the lvn and, therefore, manual selection of the relevant parameters. The work presented in this chapter sought to address these challenges, by developing computational procedures that can automate extraction of the pyloric rhythm from the bath dyed STG sample, further validating the methodology presented so far.

To overcome the limitations of classical approaches to the spectral analysis of the potentially noisy signals captured in the optical recordings, automated procedures based on modern spectral estimator methods that would enable the pyloric frequency to be determined directly from such recordings were developed. These methods include the parametric or model-based techniques such as the Yule-Walker Equation and, relevantly, non-parameter procedures as exemplified by the `pmusic` estimator. The latter, coupled with the use of the traditional periodogram technique, have provided a computationally tractable and statistically reliable spectral estimation procedure that allowed the pyloric frequency to be determined, enabling the potential mapping of the pyloric rhythm (if present) extracted from the optical recordings onto that electrophysiological data captured on the lvn. Importantly, this would allow identification of the respective pyloric neurons from the dye bathed STG sample as demonstrated previously in chapter 4.

The techniques studied were examined in detail by selecting from over forty experimental studies three datasets that covered a wide range of pyloric frequencies and a spread of SNRs. The results were analysed, discussed and presented with examples that demonstrate the potential use of the developed methodology in a practical setting.

6. Conclusions and Future Work

This chapter provides a summary of the research work presented and concludes the thesis. Recommendations for further work are also included.

6.1. Summary

The automated analyses of *in vitro* study of neuronal circuits in small systems have been an important growth area in neurosciences with advances in computing and live cell-imaging technologies over the past two decades. In particular, the ability to locate circuit neurons and simultaneously record from them at single-cell resolution in these systems is fundamental to understanding the full-scale network behaviour of neural systems. In the STG, traditional methods to identify pyloric neurons by intracellular recording can be challenging, and VSDI, an optical recording technique which simultaneously measures the membrane potential of multiple neurons, offers a promising solution. However, analysing features of VSDI data/recordings of these neurons in conjunction with the pyloric rhythm obtained on the lvn is an exacting task, requiring the development of sophisticated computational/signal processing techniques that sought to:

(a) extract the pyloric rhythm from the demonstrably noisy VSDI data;

(b) decode the intrinsically triphasic pattern of the rhythm with reference to the analogue signal recorded on the lvn; and,

(c) align the results obtained in (a) and (b) in order to identify the neuronal type of the cell in the pyloric circuit.

To facilitate the pyloric rhythm extraction from the VSDI recording, the work entailed developing a multiresolution signal processing algorithm, constructed with the SSA procedure, extracting the pyloric rhythm generated by the identified cell/ROIs from the bath dyed STG sample. The SSA based signal decomposition procedure separates the original signal into two subspaces, resulting in (i) a

mixture of a number of independent and interpretable signal components and (ii) a random or structureless noise. As such, the two-stage sequential SSA (s-SSA) procedure was developed to realise a multiresolution approach, which worked by applying the basic SSA repeatedly, with different parameters, to facilitate selective removal of unwanted/unrelated or noise components following the decomposition. This has enabled an effective and reliable extraction of the pyloric rhythm (if present) from the individual cell/ROIs, with demonstrable accuracy and high efficiency (>85%).

The constructed signal processing procedure to decode the triphasic pattern of the pyloric rhythm captured on the lvn is designed to facilitate mapping of the extracted pyloric rhythm as described above to the individual pyloric activities (PD, LP and PY) as recorded on the lvn. Here, the primary task entailed the deconstruction on the lvn of the individual phases of the pyloric rhythm by virtue of the spiking characteristics of the respective participating neurons as observed. Essentially, the spontaneous and highly synchronised activity of the PD-timed, LP-timed or PY-timed neurons were analysed using CWT, a classical time-frequency analytical method to facilitate segmenting the highly structured and regular phasing of the pyloric rhythm captured on the lvn. Importantly, the task was assisted by the s-SSA procedure, which sought to remove much of the high-frequency noise typically inherent in spike trains while selectively preserving the pyloric frequency and its higher order harmonics. The segmentation was obtained by means of a relatively simple thresholding procedure whereby the respective time periods of PY phase were separated from each pyloric cycle recorded on the lvn, thus allowing the corresponding duty cycle (DC) of the PY phase to be computed. The results were verified by comparison with the ground truth, which consists of three PY neurons identified previously with intracellular recording carried out on the STG sample.

To accomplish (c) above, the Hilbert transform approach was used to estimate the instantaneous phase of each of the three PY neurons, as the ground truth, from the respective Hilbert spectra, enabling them to be compared directly with that obtained from the reconstructed PY spike/pulse train on the lvn. As expected, the results demonstrated that the time lag between the individual PY

cell and the lvn consistently maintains a constant mean phase shift/lead of 3.43 radians, with an averaged standard deviation of 0.24 radians over the entire course of the recording.

Integrating data obtained from optical VSDI and electrophysiological recording of the lateral ventricular nerve (lvn) is a complex and exacting task. Therefore, the work presented in chapter 5 sought to refine the signal processing procedures developed thus far to enable, as proof of concept, automated extraction of the pyloric rhythm from the bath dyed STG sample, thus obviating the need for extracellular recording on the lvn. Here, a pyloric frequency estimator was developed to facilitate determining the pyloric frequency directly from the VSDI recording of the STG sample. Specifically, the estimator so constructed took advantage of the so-called super-resolution method of the MUSIC algorithm, to address the potential distortions that might be present in the results obtained by the classical approach to estimate power spectral densities (PSD) for the prospective pyloric cells. Three datasets, selected over a range of SNRs (-9dB to -20dB), were used to demonstrate identification of prospective pyloric neurons based on the resulting spectra from which the respective DCs and phase shifts, or time lags, could be determined and compared with those measured with the analogue signal recorded on the lvn. As with the procedures developed for task (c) above, the results were verified in the time domain, where successful re/alignments of the phase adjusted pyloric rhythm, extracted in the VSDI recording and the corresponding pyloric rhythm captured on the lvn were demonstrated.

6.2. Conclusions

The research described in this thesis demonstrates that advanced signal processing techniques have considerable potential for discerning the participating neurons in the pyloric circuit of *Cancer pagurus* using the optically recorded VSDI data. In particular, SSA has proved to be successful and a valuable signal-processing tool to study the typically noisy recordings of the bath applied STG sample. The analysis was significantly enhanced by the development of the sequential SSA (s-SSA) procedure,

a multi-resolution algorithm that has been shown to extract successfully the pyloric rhythm from the typically recorded VSDI data. As discussed in chapter 3, a principal challenge in analysing the VSDI data is the poor signal-to-noise ratio (SNR) achieved by the VSD, which is typically estimated at ~-20dB in the (>40) experiments and in good agreement with the approximately 10% signal (amplitude) responses noted in the published specifications. To this end, the selection of the window length (*L*) parameter is of particular importance for each of the two successive stages of the s-SSA algorithm, ensuring *L* is sufficiently large to embody the relevant features within the original and residual time series applicable in each SSA/stage, thus enabling the separation of additive components ('independent' and 'identifiable') by the respective SSA decompositions. The pyloric frequency, determined from the power spectrum for the neuropil, was used as the reference against which the resulting power spectra of the individual cells/ROIs were compared in order to identify potential pyloric cells in each bath-dyed STG sample where the pyloric rhythm, if present, was then separated from the noise by the two-stage s-SSA procedure. Here, the percentage of separation that represents the proportion of the signal energy separated by the two-stage s-SSA procedure from the original time sequence demonstrates the effectiveness of the multiresolution s-SSA procedure in terms of the pyloric rhythm extraction. Indeed, the percentage is over 85% in all cases when the pyloric frequency is the dominant component in the power spectrum between the frequency ranges of 0.5Hz to 2Hz where the pyloric rhythm is typically detected. From a methodological viewpoint, the s-SSA approach whereby the basic SSA procedure is applied in succession with different parameters (window length L) to the residuals from the preceding analysis is such a useful technique that often helps resolve the mixing problem of the time series components or formally, the problem of close singular values for weakly separable series components (Golyandina, Nekrutkin and Zhigljavsky, 2001). The principal disadvantages in the use of the SSA (and s-SSA), however, are (i) the high computational complexity, including space and time, for the calculation of the SVD, particularly when the size/dimensions of the matrix (X) is large; (ii) the signal spreads and variations over time, resulting in many elementary

matrices needed to reconstruct the signal. As such, they somewhat limit the applicability of SSA in a wider context, especially when real-time requirements might also be considered in practice.

To further distinguish the individual pyloric neurons in the STG sample, the duty cycle (DC) of each of the three pyloric phases (PD-led, LP-led and PY-led) of the pyloric rhythm cycle was selected as a computationally well-defined and biologically meaningful biometric to help identify these neurons – namely, PD-timed, LP-timed and PY-timed neuronal cells. By computing the ratio of harmonics (RH) measured from the spectrum computed for each cell, as 'signature' for the individual pyloric neuron, the DC determined for each potential pyloric cell was successfully matched with that measured for the individual pyloric phases as recorded on the lateral ventricular nerve (lvn). Indeed, this has led to the first-ever successful identification of one of the pyloric neurons (PY) from the optical recording of the STG sample as described in chapter 4 using signal processing techniques. The result was further confirmed by estimating the time lag between the optical/VSDI and analogue/lvn recordings, based on the well-established Hilbert Transform approach developed for time-frequency analysis. Here, the implementation of the phase tracking procedure determined the instantaneous phases of the detected pyloric rhythm from the optical recording, allowing them to be accurately mapped onto the triphasic pattern of the pyloric rhythm recorded on lvn.

To facilitate validating the computational procedures described above, chapter 5 describes the work on developing a pyloric frequency estimator that would enable determining the pyloric frequency directly from the VSDI data recorded for the STG sample. Given the demonstrably noisy VSDI data as described above, the estimator so constructed took into account potential distortions that might be present in the results obtained by the classical approach to estimate power spectral densities (PSD) for the prospective pyloric cells. To this end, three datasets, selected over a range of SNRs between -9dB to -20dB, were used to demonstrate, as previously described in chapter 4, identification of prospective pyloric neurons based on the estimated DCs and respective phase shifts (or time lags) measured against the analogue signal recorded on the lvn. Implementing the so-called MUSIC algorithm, the developed PSD estimator worked well in determining the pyloric frequency

over a selected range of low SNRs. In particular, the SNR obtained for the neuropil appeared to be a reliable indicator for the accurate determination of the pyloric frequency which, if present, was readily observable as a peak shown within the respective power spectra computed by the MUSIC algorithm for the individual cells, where the corresponding SNR computed in the reference periodogram is better than -20dB. The reverse is also true, that is, when SNR is lower than -20dB, the peak detection is poor in both PSD estimates (by the MUSIC-based and raw periodogram) and often erroneous, especially where there might be other neighbouring peaks, which could be attributed to noise and probably other narrowband processes. Furthermore, when the SNR is poor – under ≈-20dB in general – the number of cells/ROIs where the pyloric rhythm could be detected reliably (in statistical terms) was also low. Finally, as proof of concept, these results were verified in Figure 40 and Figure 47, where successful re/alignments in the time domain of the phase adjusted pyloric rhythm extracted in the VSDI recording and the corresponding pyloric rhythm captured on the lvn were demonstrated by means of the respective Hilbert spectra as previously described (in chapter 4).

Lastly, the contributions made in this research project are summarised as follows:

i. The pyloric rhythm was extracted reliably from the optical/VSDI recordings by means of the developed s-SSA procedure that provides the required multiresolution capability to separate the pyloric rhythm efficiently despite the low SNR typically achieved by the VSD.
ii. The use of the duty cycle (DC) and the ratio of harmonics (RH) as biometric features enabled the successful identification of the pyloric neuron (PY) from the optical recording of the STG sample, by integrating such recordings with the extracellular/electrophysiological recordings on the lvn.
iii. The pyloric frequency was accurately determined from the demonstrably noisy VSDI recording/data, obviating the need for an initial manual study of the electrophysiological recording on the lvn. This opens up the possibility of automated identification of pyloric neurons in real-time.

6.3. Further Work

Further improvements could be achieved in the following areas:

- Given the considerable variability in the signal-to-noise ratio (SNR) achieved across the experiments completed to date, it would be beneficial to re-examine the equipment deployed for future experiments. In particular, the problem with the perfusion (cooling saline flow) should be addressed, as should several improvements be made in the imaging equipment, including, especially, the light source and optical camera/recordings, identified (although not documented in this thesis) recently at the end of this research/project. This should facilitate obtaining greater consistency and, hence, improved identification performance. In addition, importantly, the resulting improvement in the achievable SNR of the optical data would help increase the accuracy and reliability of the automated procedure for determining the pyloric frequency from the optical/VSDI data (chapter 5). This would obviate the need for an initial manual study of the electrophysiological recording on the lvn.

  Equally, an investigation into the use of other dyes, particularly those that offer better yields and preferably without the technically demanding task to desheathed the STG sample is recommended.

- At present, the automated methodology presented in this thesis to identify the pyloric neurons has two limitations. First, the duty cycle (DC) on its own is not, as yet, sufficiently discernible to determine the neuronal type automatically in the pyloric circuit. This is mainly due to the inevitable estimation errors given the generally poor SNR achieved with the VSDI data and, relatedly, the relatively similar and comparatively narrow DC widths of the LP-led and PD-led phases of neurons that must be estimated from these (noisy) data. Additionally, processing the lvn recording and its subsequent integration with the VSDI recording could be very challenging, frequently requiring some minor manual adjustments over the full length of lvn recording because of naturally occurring variability in the bursting cycle of the participating neurons in the pyloric circuit. One possible solution concerns the development of further biometrics such

as neuronal 'signatures' for the individual pyloric neurons (PD, LP and PY) using, for example, the tried and tested spectral generator techniques as reported in earlier work (dos Santos, Andras and Lam, 2017b).

- While additional challenges remain, the successful development of the pyloric frequency estimator as demonstrated in chapter 5 has opened up the possibility of real-time monitoring using automated analysis of VSDI data streams without the need for the extracellular analysis. Specifically, the MUSIC-based spectral estimation method, designed to overcome the shortcoming of the classical Fourier-based approach, is particularly effective when the input/optical data segments to be analysed are relatively short. This would enable estimating the pyloric frequency more responsively and, hence, revising/tracking its changes more accurately over the course of an experiment with minimum lag time. This should mesh well with the additional construction of an image segmentation procedure that will facilitate automated demarcation of the individual cell/ROIs from the high-resolution image of the STG sample (as described in section 3.2.5), for example, coupled with the neuronal signature generator described above, should offer a realistic prospect for realising such a real-time platform.
- Lastly, the value of the identification methodology presented in this thesis will be greatly enhanced by extending the signal processing procedures developed to facilitate studying other organisms/living cells, with or without spontaneous activity. To this end, the closely allied study of the slow varying gastric rhythm (described in section 2.1.3), for example, would be a realistic first step to demonstrate this.

Finally, the signal-processing methodology that we described in this thesis has demonstrated its applicability to a broad spectrum of biological/cellular systems, where the VSDI technology can be used to characterise the electrical activity as measured by cell membrane potentials from which vital/functional information about such cells is obtained. In addition to other neurophysiological systems, for example, the heart, eyes, pancreas, muscles, *etc*., all are commonly known to have

measurable and meaningful membrane potentials whereby our ability to simultaneously record from them at single-cell resolution is fundamental to understanding the full-scale behaviours of such systems. To this end, work is currently underway to develop computationally tractable and biologically meaningful 'signatures' that will identify directly from the optical imaging data the neurons responsible for generating the extracted pyloric frequency, without the requirement for the challenging task of analysing the lvn recording (dos Santos and Lam 2019; Lam and dos Santos, in preparation).

References

Adamczak, S., Makieła, W. and Stępień, K. (2010) 'Investigating advantages and disadvantages of the analysis of a geometrical surface structure with the use of Fourier and wavelet transform', XVII(2), pp. 233–244. doi: 10.2478/v10178-010-0020-x.Brought.

Ahrens, M. B. and Engert, F. (2015) 'Large-scale imaging in small brains', *Current Opinion in Neurobiology*. Elsevier Ltd, 32, pp. 78–86. doi: 10.1016/j.conb.2015.01.007.

Akansu, A. N. and Haddad, R. A. (2001) *Multiresolution Signal Decomposition*. second edi. Academic Press. doi: 10.1016/B978-012047141-6/50007-0.

Arrillaga, J. *et al.* (2000) *Power System Harmonic Analysis*. John Wiley & Sons, Ltd. doi: 10.1002/9781118878316.

Atikur Rahman Khan, M. and Poskitt, D. S. (2013) 'A Note on window length selection in singular spectrum analysis', *Australian and New Zealand Journal of Statistics*, 55(2), pp. 87–108. doi: 10.1111/anzs.12027.

Ayali, A. (2009) 'The role of the arthropod stomatogastric nervous system in moulting behaviour and ecdysis', *The Journal of Experimental Biology*, 212, pp. 453–459. doi: 10.1242/jeb.023879.

Bai, D. *et al.* (2014) *Low molecular weight Neutral Boron Dipyrromethene (Bodipy) dyads for fluorescence-based neural imaging*, *Journal of Molecular Structure*. Available at: http://ac.els-cdn.com/S0022286014002002/1-s2.0-S0022286014002002-main.pdf?_tid=f5e6dde2-23ee-11e5-b8bf-00000aacb360&acdnat=1436194674_00a8db301b0861d81bf5e9f4ff602b5c (Accessed: 6 July 2015).

Baker, B. J. *et al.* (2005) 'Imaging Brain ActivityWith Voltage- and Calcium-SensitiveDyes', *Cellular and Molecular Neurobiology*, 25(2), pp. 245–282. doi: 10.1007/978-1-59745-543-5_3.

Baldwin, D. H. and Graubard, K. (1995) 'Distribution of fine neurites of stomatogastric neurons of the crab Cancer borealis: evidence for a structured neuropil', *The Journal of comparative neurology*, 356, pp. 355–367. doi: 10.1002/cne.903560304.

Balsera, M. A. *et al.* (1996) 'Principal component analysis and long time protein dynamics', *The Journal of Physical Chemistry*. American Chemical Society, 100(7), pp. 2567–2572. doi: 10.1021/jp9536920.

Barrett, S. F. and Pack, D. J. (2006) *Microcontrollers Fundamentals for Engineers and Scientists*. Morgan and Claypool. doi: 10.2200/S00025ED1V01Y200605DCS001.

Bartos, M. and Nusbaum, M. P. (1997) 'Intercircuit control of motor pattern modulation by presynaptic inhibition', *The Journal of Neuroscience*, 17(7), pp. 2247–2256.

Beauchemin, S., Hesterberg, D. and Beauchemin, M. (2002) 'Principal component analysis approach for modeling sulfur K-XANES spectra of humic acids', *Soil Science Society of America Journal*. Soil Science Society, 66, pp. 83–91. doi: 10.2136/sssaj2002.8300.

Belanger, J. H. (2005) 'Contrasting tactics in motor control by vertebrates and arthropods', *Integrative and Comparative Biology*, 45(4), pp. 672–678. doi: 10.1093/icb/45.4.672.

Bellanca, J. L. *et al.* (2013) 'Harmonic ratios: A quantification of step to step symmetry', *Journal of Biomechanics*. Elsevier, 46, pp. 828–831. doi: 10.1016/j.jbiomech.2012.12.008.

Benniston, A. C., Clift, S. and Harriman, A. (2011) 'Intramolecular charge-transfer interactions in a julolidine-Bodipy molecular assembly as revealed via 13C NMR chemical shifts', *Journal of Molecular Structure*. Elsevier B.V., 985, pp. 346–354. doi: 10.1016/j.molstruc.2010.11.018.

Berg, T. *et al.* (1995) 'Atmospheric trace element deposition: Principal component analysis of ICP-MS data from moss samples', *Environmental Pollution*. Elsevier, 88(1), pp. 67–77. doi: 10.1016/0269-7491(95)91049-Q.

BIOTIC - Biological Traits Information Catalogue (2018) *BIOTIC Species Information for Cancer pagers*, *BIOTIC Species Information for Cancer pagers*. Available at: http://www.marlin.ac.uk/biotic/browse.php?sp=4129 (Accessed: 25 May 2018).

Blitz, D. M. *et al.* (2008) 'A newly identified extrinsic input triggers a distinct gastric mill rhythm via activation of modulatory projection neurons', *The Journal of Experimental Biology*, 211, pp. 1000–1011. doi: 10.1242/jeb.015222.

Blitz, D. M. and Nusbaum, M. P. (1997) 'Motor pattern selection via inhibition of parallel

pathways', *The Journal of Neuroscience*, 17(13), pp. 4965–4975.

Böhm, H., Dybek, E. and Heinzel, H.-G. (2001) 'Anatomy and in vivo activity of neurons connecting the crustacean stomatogastric nervous system to the brain', *Journal of Comparative Physiology*, 187, pp. 393–403. doi: 10.1007/s003590100212.

Brette, R. and Destexhe, A. (2012) 'Intracellular recording', in Brette, R. and Destexhe, A. (eds) *Handbook of Neural Activity Measurement*. Cambridge University Press Cambridge University Press, pp. 44–91. Available at: http://cns.iaf.cnrs-gif.fr/files/ChapIntra2008.pdf (Accessed: 22 January 2018).

Briggman, K. L. and Kristan, W. B. (2006) 'Imaging dedicated and multifunctional neural circuits generating distinct behaviors', *Journal of Neuroscience*, 26(42), pp. 10925–10933. doi: 10.1523/JNEUROSCI.3265-06.2006.

Broomhead, D. S. and King, G. P. (1986) 'Extracting qualitative dynamics from experimental data', *Physica 20D*, 20(2–3), pp. 217–236. doi: 10.1016/0167-2789(86)90031-X.

Brown, G. D. *et al.* (2008) *Independent Component Analysis of Optical Recordings from Tritonia Swimming Neurons*, *UCSD INC Technical Report INC-08-001*. La Jolla. Available at: http://citeseerx.ist.psu.edu/viewdoc/summary?doi=10.1.1.91.1036.

Brown, G. D., Yamada, S. and Sejnowski, T. J. (2001) 'Independent component analysis at the neural cocktail party', *Trends in Neurosciences*, 24(1), pp. 54–63. doi: 10.1016/S0166-2236(00)01683-0.

Brunel, N., Sup, E. N. and Wang, X. (2001) 'Effects of neuromodulation in a cortical network model of object working memory dominated by recurrent inhibition', *Journal of Computational Neuroscience*, 11, pp. 63–85. doi: 10.1023/A:1011204814320.

Brunelli, R. (2009) *Template Matching Techniques in Computer Vision: Theory and Practice*. John Wiley & Sons, Ltd. doi: 10.1002/9780470744055.

Brunelli, R. and Poggio, T. (1993) 'Face recognition: features versus templates', *IEEE Transactions on Pattern Analysis and Machine Intelligence*, 15(10), pp. 1042–1052. doi: 10.1109/34.254061.

Bucher, D., Johnson, C. D. and Marder, E. (2007) 'Neuronal morphology and neuropil structure in the stomatogastric ganglion of the lobster, Homarus americanus', *The Journal of Comparative Neurology*, 501, pp. 185–205. doi: 10.1002/cne.

Bucher, D., Prinz, A. A. and Marder, E. (2005) 'Animal-to-animal variability in motor pattern production in adults and during growth', *The Journal of Neuroscience*, 25(7), pp. 1611–1619. doi: 10.1523/JNEUROSCI.3679-04.2005.

Bucher, D., Thirumalai, V. and Marder, E. (2003) 'Axonal dopamine receptors activate peripheral spike initiation in a stomatogastric motor neuron', *The Journal of Neuroscience*, 23(17), pp. 6866–6875.

Byrne, G. F., Crapper, P. F. and Mayo, K. K. (1980) 'Monitoring land-cover change by principal component analysis of multitemporal landsat data', *Remote Sensing of Environment*. Elsevier, 10(3), pp. 175–184. doi: 10.1016/0034-4257(80)90021-8.

Caplan, J. S., Williams, A. H. and Marder, E. (2014) 'Many parameter sets in a multicompartment model oscillator are robust to temperature perturbations', *The Journal of Neuroscience*, 34(14), pp. 4963–4975. doi: 10.1523/JNEUROSCI.0280-14.2014.

Carniel, R. *et al.* (2006) 'On the singular values decoupling in the Singular Spectrum Analysis of volcanic tremor at Stromboli', *Natural Hazards and Earth System Science*, 6, pp. 903–909. doi: 10.5194/nhess-6-903-2006.

Caspi, S., Helm, M. and Laslett, L. J. (1994) 'The use of harmonics in 3-D magnetic fields', *IEEE Transactions on Magnetics*, 30(4), pp. 2419–2422. doi: 10.1109/20.305765.

Chemla, S. and Chavane, F. (2010) 'Voltage-sensitive dye imaging: Technique review and models', *Journal of Physiology - Paris*. Elsevier Ltd, 104, pp. 40–50. doi: 10.1016/j.jphysparis.2009.11.009.

Chi, Z. *et al.* (2007) 'Template-based spike pattern identification with linear convolution and dynamic time warping', *Journal of Neurophysiology*. American Physiological Society, 97(2), pp. 1221–1235. doi: 10.1152/jn.00448.2006.

Chung, J. E. *et al.* (2017) 'A fully automated approach to spike sorting', *Neuron*. Elsevier Inc.,

95, pp. 1381–1394. doi: 10.1016/j.neuron.2017.08.030.

Clemens, S., Massabuau, J.-C., *et al.* (1998) 'In vivo modulation of interacting central pattern generators in lobster Stomatogastric Ganglion: Influence of feeding and partial pressure of oxygen', *The Journal of Neuroscience*, 18(7), pp. 2788–2799.

Clemens, S., Combes, D., *et al.* (1998) 'Long-term expression of two interacting motor pattern-generating networks in the stomatogastric system of freely behaving lobster', *Journal of Neurophysiology*, 79(3), pp. 1396–1408.

Clemens, S., Meyrand, P. and Simmers, J. (1998) 'Feeding-induced changes in temporal patterning of muscle activity in the lobster stomatogastric system', *Neuroscience Letters*, 254(2), pp. 65–68. doi: 10.1016/S0304-3940(98)00511-4.

Cohen, L. B. (2010) 'Historical Overview and General Methods of Membrane Potential Imaging', in Canepari, M. and Zecevic, D. (eds) *Membrane Potential Imaging in the Nervous System. Methods and Applications*. New York: Springer, pp. 1–11. doi: 10.1007/978-3-319-17641-3_1.

Cohen, L. B., Keynes, R. D. and Hille, B. (1968) 'Light scattering and birefringence changes during nerve activity', *Nature*. Nature Publishing Group, 218(5140), pp. 438–441. doi: 10.1038/218438a0.

Coleman, M. J. *et al.* (1992) 'Distribution of modulatory inputs to the stomatogastric ganglion of the crab, Cancer borealis', *The Journal of Comparative Neurology*. Wiley Subscription Services, Inc., A Wiley Company, 325(4), pp. 581–594. doi: 10.1002/cne.903250410.

Derby, C. and Thiel, M. (2014) *Nervous Systems and Control of Behavior (The Natural History of Crustacea)*. Volume 3. New York: Oxford University Press. Available at: https://books.google.com/books?hl=en&lr=&id=ekdYBAAAQBAJ&pgis=1 (Accessed: 12 July 2015).

Dickinson, P. S. (2006) 'Neuromodulation of central pattern generators in invertebrates and vertebrates', *Current Opinion in Neurobiology*. Elsevier Current Trends, 16(6), pp. 604–614. doi: 10.1016/J.CONB.2006.10.007.

Dombeck, D. A., Blanchard-Desce, M. and Webb, W. W. (2004) 'Optical recording of action potentials with second-harmonic generation microscopy', *The Journal of Neuroscience*. Society for Neuroscience, 24(4), pp. 999–1003. doi: 10.1523/JNEUROSCI.4840-03.2004.

Dougherty, E. R. *et al.* (2005) *Genomic Signal Processing and Statistics*, *EURASIP Book Series on Signal Processing and Communications*. New York: Hindawi Publishing Corporation. doi: 10.1155/9789775945075.

Elsner, J. B. and Tsonis, A. A. (1996) *Singular Spectrum Analysis: A New Tool in Time Series Analysis*. New York: Springer Science & Business Media. Available at: https://books.google.com.br/books/about/Singular_Spectrum_Analysis.html?id=pHsGF9WIBxkC&pgis=1.

Ermentrout, G. B. and Terman, D. H. (2010) *Mathematical Foundations of Neuroscience*. Edited by S. S. Antman et al. Springer Science & Business Media. Available at: https://books.google.com/books?hl=en&lr=&id=0fLdzaFgtjcC&pgis=1 (Accessed: 27 September 2015).

Faumont, S. *et al.* (2005) 'Reconfiguration of multiple motor networks by short- and long-term actions of an identified modulatory neuron', *European Journal of Neuroscience*, 22, pp. 2489–2502. doi: 10.1111/j.1460-9568.2005.04442.x.

Fénelon, V. *et al.* (2003) 'Maturation of rhythmic neural network: Role of central modulatory inputs', *Journal of Physiology*, 97, pp. 59–68. doi: 10.1016/j.jphysparis.2003.10.007.

Fenton, M. B. *et al.* (2011) 'Variation in the use of harmonics in the calls of laryngeally echolocating bats', *Acta Chiropterologica*, 13(1), pp. 169–178. doi: 10.3161/150811011X578714.

Fishell, G. and Heintz, N. (2013) 'The neuron identity problem: Form meets function', *Neuron*, 80, pp. 602–612. doi: 10.1016/j.neuron.2013.10.035.

Fisheries and Aquaculture Department (2018) *Species Distribution Map Viewer*, *Food and Agriculture Organisation of the United Nations*. Available at: http://www.fao.org/figis/geoserver/factsheets/species.html?species=CRE-m&prj=4326 (Accessed: 25 May 2018).

Fluhler, E., Burnham, V. G. and Loew, L. M. (1985) 'Spectra, membrane binding, and potentiometric responses of new charge shift probes.', *Biochemistry*, 24(21), pp. 5749–5755. doi: 10.1021/BI00342A010.

Follmann, R., Goldsmith, C. J. and Stein, W. (2017) 'Spatial distribution of intermingling pools of projection neurons with distinct targets: A 3D analysis of the commissural ganglia in Cancer borealis', *The Journal of Comparative Neurology*, 525(8), pp. 1827–1843. doi: 10.1002/cne.24161.

Fraedrich, K. (1986) 'Estimating the dimensions of weather and climate attractors', *Journal of the Atmospheric Sciences*, 43(5), pp. 419–432. doi: 10.1175/1520-0469(1986)043<0419:ETDOWA>2.0.CO;2.

Fromherz, P. and Lambacher, A. (1991) 'Spectra of voltage-sensitive fluorescence of styryl-dye in neuron membrane', *Biochimica et Biophysica Acta (BBA) - Biomembranes*. Elsevier, 1068(2), pp. 149–156. doi: 10.1016/0005-2736(91)90203-K.

Frost, W. N. *et al.* (2010) 'Use of Fast-Responding Voltage-Sensitive dyes for Large-Scale Recording og Neuronal Spiking Activity with Single-Cell Resolution', in Canepari, M. and Zecevic, D. (eds) *Membrane Potential Imaging in the Nervous System*. New York: Springer, pp. 53–60. doi: 10.1007/978-1-4419-6558-5.

Frost, W. N. and Wu, J. (2015) 'Voltage-sensitive dye imaging', in Covey, E. and Carter, M. (eds) *Basic Electrophysiological Methods*. New York: Oxford University Press. Available at: https://books.google.co.uk/books?hl=en&lr=&id=RObcBgAAQBAJ&oi=fnd&pg=PA169&dq=di-4+anepps+stomatogastric+ganglion&ots=d-LnDvmRDB&sig=2O3ICsCUoFucVih_zdE73_kUhgI#v=onepage&q&f=false (Accessed: 18 February 2017).

Gansert, J., Golowasch, J. and Nadim, F. (2007) 'Sustained Rhythmic Activity in Gap-Junctionally Coupled Networks of Model Neurons Depends on the Diameter of Coupled Dendrites', *Journal of Neurophysiology*, 98(6), pp. 3450–3460. doi: 10.1152/jn.00648.2007.

Ghaderi, F., Mohseni, H. R. and Sanei, S. (2011) 'Localizing heart sounds in respiratory signals

using singular spectrum analysis', *IEEE Transactions on Biomedical Engineering*, 58(12 PART 1), pp. 3360–3367. doi: 10.1109/TBME.2011.2162728.

Gibson, S., Judy, J. W. and Marković, D. (2010) 'Technology-aware algorithm design for neural spike detection, feature extraction, and dimensionality reduction', *IEEE transactions on neural systems and rehabilitation engineering*, 18(5), pp. 469–478. doi: 10.1109/TNSRE.2010.2051683.

Goaillard, J.-M. *et al.* (2009) 'Functional consequences of animal-to-animal variation in circuit parameters', *Nature Neuroscience*, 12, pp. 1420–1428. Available at: http://web.a.ebscohost.com/ehost/pdfviewer/pdfviewer?sid=d83c61ec-f5d0-4b06-97b9-59dfe0ea9afa%40sessionmgr4005&vid=1&hid=4107 (Accessed: 26 June 2015).

Goeritz, M. L. *et al.* (2013) 'Neuropilar projections of the anterior gastric receptor neuron in the Stomatogastric Ganglion of the Jonah crab, Cancer borealis', *PLoS ONE*, 8(12), pp. 1–15. doi: 10.1371/journal.pone.0079306.

Goldsmith, C. J., Städele, C. and Stein, W. (2014) 'Optical imaging of neuronal activity and visualization of fine neural structures in non-desheathed nervous systems', *PLoS ONE*, 9(7), pp. 1–15. Available at: file:///C:/Users/Filipa/Downloads/Goldsmith_et_al_2014_Plosone_published.pdf (Accessed: 6 July 2015).

Golowasch, J. *et al.* (1999) 'Network stability from activity-dependent regulation of neuronal conductances', *Neural computation*, 11, pp. 1079–1096. doi: 10.1162/089976699300016359.

Golowasch, J., Abbott, L. F. and Marder, E. (1999) 'Activity-dependent regulation of potassium currents in an identified neuron of the Stomatogastric Ganglion of the crab Cancer borealis', *The Journal of Neuroscience*, 19, pp. 1–5.

Golowasch, J., Manor, Y. and Nadim, F. (1999) 'Recognition of slow processes in rhythmic networks', *Trends in Neurosciences*, 22(9), pp. 375–377. doi: 10.1016/S0166-2236(99)01466-6.

Golyandina, N. (2010) 'On the choice of parameters in Singular Spectrum Analysis and related subspace-based methods', *Statistic Interface*, 3, pp. 259–279. doi: 10.4310/SII.2010.v3.n3.a2.

Golyandina, N., Nekrutkin, V. and Zhigljavsky, A. (2001) *Analysis of Time Series Structure - SSA*

and Related Techniques. Boca Raton: Chapman & Hall/CRC.

Golyandina, N. and Zhigljavsky, A. (2013) *Singular Spectrum Analysis for Time Series*. New York: Springer. doi: 10.1007/978-3-642-34913-3.

Grashow, R., Brookings, T. and Marder, E. (2009) 'Reliable neuromodulation from circuits with variable underlying structure', *Proceedings of the National Academy of Sciences - PNAS*, 106(28), pp. 11742–11746. doi: 10.1073/pnas.0905614106.

Grillner, S. (2006) 'Biological pattern generation: The cellular and computational logic of networks in motion', *Neuron*, 52, pp. 751–766. doi: 10.1016/j.neuron.2006.11.008.

Gutierrez, G. J. and Grashow, R. G. (2009) 'Cancer borealis Stomatogastric Nervous System dissection', *Journal of Visualized Experiments : JoVE*, pp. 1–5. doi: 10.3791/1207.

Gutierrez, G. J., O'Leary, T. and Marder, E. (2013) 'Multiple mechanisms switch an electrically coupled, synaptically inhibited neuron between competing rhythmic oscillators', *Neuron*. Elsevier Inc., 77, pp. 845–858. doi: 10.1016/j.neuron.2013.01.016.

Hahn, S. L. (1996) *Hilbert Transforms in Signal Processing*. Norwood, MA: Artech House, INC.

Harris-Warrick, R. M. *et al.* (1992) *Dynamic Biological Networks: The Stomatogastric Nervous System*, *Massachusetts Institute of Thechnology*. Available at: https://mitpress.mit.edu/books/dynamic-biological-networks (Accessed: 17 July 2015).

Harris-Warrick, R. M. *et al.* (1995) 'Dopamine modulation of transient potassium current evokes phase shifts in a central pattern generator network', *The Journal of Neuroscience*, 15(1), pp. 342–358.

Harris-Warrick, R. M. and Marder, E. (1991) 'Modulation of neural networks for behavior', *Annual Review of Neuroscience*, 14, pp. 39–57.

Hartenstein, V. (2006) 'The neuroendocrine system of invertebrates: A developmental and evolutionary perspective', *Journal of Endocrinology*, 190, pp. 555–570. doi: 10.1677/joe.1.06964.

Hartline, D. K. (1979) 'Pattern generation in the lobster (Panulirus) stomatogastric ganglion', *Biological Cybernetics*, 33(4), pp. 223–236. doi: 10.1007/BF00337411.

Hassani, H. (2007) 'Singular Spectrum Analysis: Methodology and Comparison', *Journal of*

Data Science, (5), pp. 239–257. doi: 10.1227/01.NEU.0000349921.14519.2A.

Hassani, H. (2010) 'A brief introduction to singular spectrum analysis'. Cardiff, pp. 1–11. Available at: https://www.researchgate.net/publication/267723014_A_Brief_Introduction_to_Singular_Spectrum_Analysis.

Hassani, H., Heravi, S. and Zhigljavsky, A. (2009) 'Forecasting European industrial production with singular spectrum analysis', *International Journal of Forecasting*. Elsevier, 25(1), pp. 103–118. doi: 10.1016/J.IJFORECAST.2008.09.007.

Hayes, M. H. (1996) *Statistical Digital Signal Processing and Modeling*. John Wiley & Sons, Inc.

Haykin, S. (2008) *Neural Networks and Learning Machines*. third edit, *Pearson Prentice Hall New Jersey USA 936 pLinks*. third edit. New Jersey: Prentice-Hall Inc. doi: 978-0131471399.

Hedrich, U. B. S., Diehl, F. and Stein, W. (2011) 'Gastric and pyloric motor pattern control by a modulatory projection neuron in the intact crab Cancer pagurus', *Journal of Neurophysiology*, 105, pp. 1671–1680. doi: 10.1152/jn.01105.2010.

Heinzel, H.-G., Weimann, J. M. and Marder, E. (1993) 'The behavioral repertoire of the Gastric Mill in the crab, Cancer pagurus: An insitu endoscopic and electrophysiological examination', *The Journal of Neuroscience*, 13(4), pp. 1793–1803. Available at: http://www.researchgate.net/publication/14735162_The_behavioral_repertoire_of_the_gastric_mill_in_the_crab_Cancer_pagurus_an_in_situ_endoscopic_and_electrophysiological_examination (Accessed: 28 June 2015).

Heinzel, H. G. and Selverston, A. I. (1988) 'Gastric mill activity in the lobster. III. Effects of proctolin on the isolated central pattern generator', *Journal of Neurophysiology*, 59(2), pp. 566–585. doi: 10.1152/jn.1988.59.2.566.

Heraghty, N. (2013) *Investigating the abundance, distribution and habitat use of juvenile Cancer pagurus (L.) of the intertidal zone around Anglesey and Llŷn Peninsula, North Wales (UK)*, *School of Ocean Sciences*.

Herrmann, C. S., Grigutsch, M. and Bush, N. A. (2005) 'EEG Oscillations and Wavelet Analysis',

in Handy, T. C. (ed.) *Event-related potentials : a methods handbook*. Cambridge, MA: MIT Press, p. 404. Available at: https://books.google.co.uk/books?hl=en&lr=&id=OQyZEfgEzRUC&oi=fnd&pg=PA229&dq=morlet+wavelet+neuroscience&ots=A8r_uumTxy&sig=NwnuttQE7WjC3Kuqkqj1kDUjXsE#v=onepage&q=morlet&f=false (Accessed: 21 February 2018).

Hill, E. S. *et al.* (2010) 'Validation of independent component analysis for rapid spike sorting of optical recording data', *Journal of Neurophysiology*, 104, pp. 3721–3731. doi: 10.1152/jn.00691.2010.

Hill, E. S., Bruno, A. M. and Frost, W. N. (2014) 'Recent developments in VSD imaging of small neuronal networks', *Learning & Memory*, 21, pp. 499–505. doi: 10.1101/lm.035964.114.

Hoebe, R. A. *et al.* (2007) 'Controlled light-exposure microscopy reduces photobleaching and phototoxicity in fluorescence live-cell imaging', *Nature Biotechnology*. Nature Publishing Group, 25, pp. 249–253. doi: 10.1038/nbt1278.

Hooper, S. L. (1998) 'Transduction of temporal patterns by single neurons', *Nature Neuroscience*, 1(8).

Hooper, S. L. and DiCaprio, R. A. (2004) 'Crustacean motor pattern generator networks', *NeuroSignals*, 13, pp. 50–69. doi: 10.1159/000076158.

Hooper, S. L. and Marder, E. (1987) 'Modulation of the lobster pyloric rhythm by the peptide proctolin', *The Journal of Neuroscience*, 7(7), pp. 2097–2112.

Hotelling, H. (1933) 'Analysis of a complex of statistical variables into principal components', *Journal of Educational Psychology*, 24(6), pp. 417–441. doi: 10.1037/h0071325.

Hramov, A. E. *et al.* (2015) *Wavelets in Neuroscience*. Springer-Verlag Berlin Heidelberg. doi: 10.1016/j.neuroimage.2015.05.057.

Hudson, A. E., Archila, S. and Prinz, A. A. (2010) 'Identifiable cells in the crustacean Stomatogastric Ganglion', *Physiology*, 25, pp. 311–318. doi: 10.1152/physiol.00019.2010.

Hulteen, J. C. and Martin, C. R. (1997) 'A general template-based method for the preparation of nanomaterials', *Journal of Materials Chemistry*. Royal Society of Chemistry, 7, pp. 1075–1087.

doi: 10.1039/a700027h.

Huxley, T. H. (1880) *The crayfish - an introduction to the study of zoology*. London: C. Kegan Paul & Co.

Hyvärinen, A., Karhunen, J. and Oja, E. (2001) *Independent component analysis*. John Wiley & Sons, Inc. doi: 10.1002/0471221317.

Ieracitano, C. *et al.* (2018) 'Investigating the Brain Connectivity Evolution in AD and MCI Patients Through the EEG Signals' Wavelet Coherence', in. Springer, Cham, pp. 259–269. doi: 10.1007/978-3-319-56904-8_25.

James, J. F. (2011) *A Student's Guide to Fourier Transforms with Applications in Physics and Engineering*. third edit, *Design*. third edit. Cambridge University Press. doi: 10.1017/CBO9780511762307.

Jobert, M. *et al.* (1994) 'Wavelets - a new tool in sleep biosignal analysis', *Journal of Sleep Research*. Blackwell Publishing Ltd, 3(4), pp. 223–232. doi: 10.1111/j.1365-2869.1994.tb00135.x.

JOC/EFR © (2001) *Parseval biography*. Available at: http://www-history.mcs.st-andrews.ac.uk/Biographies/Parseval.html (Accessed: 8 November 2018).

Jolliffe, I. T. (2002) *Principal Component Analysis, Second Edition*. second edi. New York: Springer-Verlag. doi: 10.2307/1270093.

Jolliffe, I. T. and Cadima, J. (2016) 'Principal component analysis: a review and recent developments', *Philosophical transactions. Series A, Mathematical, physical, and engineering sciences*. The Royal Society, 374(2065), p. 20150202. doi: 10.1098/rsta.2015.0202.

Kao, C. Y. (1960) 'Postsynaptic electrogenesis in sptate giant axons. II Comparision of medial and lateral giant axons of crayfish', *Journal of Neurophysiology*, 23, pp. 618–635. doi: 10.1152/jn.1960.23.6.618.

Katz, P. S. (1995) 'Neuromodulation and motor pattern generation in crustacean Stomatogastric Nervous System', *Neural Control of Movements*, pp. 277–283.

Kauer, J. S., Senseman, D. M. and Cohen, L. B. (1987) 'Odor-elicited activity monitored

simultaneously from 124 regions of the salamander olfactory bulb using a voltage-sensitive dye', *Brain Research*, 418(2), pp. 255–261. doi: 10.1016/0006-8993(87)90093-X.

Kay, S. M. (1999) *Modern spectral estimation: theory and application*. Prentice Hall. Available at: https://books.google.co.uk/books/about/Modern_Spectral_Estimation.html?id=4Ft_AAAACAAJ&redir_esc=y (Accessed: 8 November 2018).

Kilman, V. L. and Marder, E. (1996) 'Ultrastructure of the stomatogastric ganglion neuropil of the crab, Cancer borealis', *The Journal of Comparative Neurology*. John Wiley & Sons, Inc., 374, pp. 362–375. doi: 10.1002/(SICI)1096-9861(19961021)374:3<362::AID-CNE5>3.0.CO;2-#.

Kirby, M. S. and Nusbaum, M. P. (2007) 'Central nervous system projections to and from the commissural ganglion of the crab Cancer borealis.', *Cell and tissue research*, 328(3), pp. 625–37. doi: 10.1007/s00441-007-0398-2.

Konnerth, A. and Orkand, R. K. (1986) 'Voltage-sensitive dyes measure potential changes in axons and glia of the frog optic nerve', *Neuroscience Letters*. Elsevier, 66(1), pp. 49–54. doi: 10.1016/0304-3940(86)90164-3.

Kristan, W. B., Calabrese, R. L. and Friesen, W. O. (2005) 'Neuronal control of leech behavior', *Progress in Neurobiology*, 76, pp. 279–327. doi: 10.1016/j.pneurobio.2005.09.004.

Lam, K. P. *et al.* (2016) 'Monitoring stem cells in phase contrast imaging', in Farkas, D. L., Nicolau, D. V., and Leif, R. C. (eds). International Society for Optics and Photonics, p. 97110E. doi: 10.1117/12.2211017.

Lam, KP. and dos Santos, F. 'A robust signature generator for voltage sensitive dye imaging' (working title), in preparation.

Lewicki, M. S. (1998) 'A review of methods for spike sorting: the detection and classification of neural action potentials', *Network: Computation in Neural Systems*, 9(4), pp. R53–R78. doi: 10.1088/0954-898X_9_4_001.

Loew, L. M. *et al.* (1992) 'A naphthyl analog of the aminostyryl pyridinium class of potentiometric membrane dyes shows consistent sensitivity in a variety of tissue, cell, and

model membrane preparations', *The Journal of Membrane Biology*. Springer-Verlag, 130(1), pp. 1–10. doi: 10.1007/BF00233734.

Loew, L. M. (2010) 'Design and Use of Organic Voltage Sensitive Dyes', in Canepari, M. and Zecevic, D. (eds) *Membrane Potential Imaging in the Nervous System. Methods and Applications*. New York: Springer, pp. 13–23. doi: 10.1007/978-1-4419-6558-5.

Marder, E. *et al.* (1987) 'Distribution and partial characterization of FMRFamide-like peptides in the stomatogastric nervous systems of the rock crab, Cancer borealis, and the spiny lobster, Panulirus interruptus', *The Journal of Comparative Neurology*. Wiley Subscription Services, Inc., A Wiley Company, 259(1), pp. 150–163. doi: 10.1002/cne.902590111.

Marder, E. *et al.* (2005) 'Invertebrate central pattern generation moves along', *Current Biology*, 15(17), pp. 685–699. doi: 10.1016/j.cub.2005.08.022.

Marder, E. *et al.* (2015) 'How can motor systems retain performance over a wide temperature range? Lessons from the crustacean stomatogastric nervous system', *Journal of Comparative Physiology A*, 201(9), pp. 851–856. doi: 10.1007/s00359-014-0975-2.

Marder, E. and Bucher, D. (2001) 'Central pattern generators and the control of rythmic movements', *Current Biology*, 11(23), pp. R986–R996.

Marder, E. and Bucher, D. (2007) 'Understanding circuit dynamics using the stomatogastric nervous system of lobsters and crabs', *Annual Review of Physiology*, 69, pp. 13.1–12.26. doi: 10.1146/annurev.physiol.69.031905.161516.

Marder, E. and Calabrese, R. L. (1996) 'Principles of rhythmic motor pattern generation', *Physiological Reviews*, 76(3), pp. 687–717.

Marder, E., Goeritz, M. L. and Otopalik, A. G. (2015) 'Robust circuit rhythms in small circuits arise from variable circuit components and mechanisms', *Current Opinion in Neurobiology*. Elsevier Ltd, 31, pp. 156–163. doi: 10.1016/j.conb.2014.10.012.

Marder, E. and Weimann, J. M. (1992) 'Modulatory control of multiple task processing in the Stomatogastric Nervous System', *Neurobiology of Motor Programme Selection*, pp. 3–19.

Margarito, J. *et al.* (2016) 'User-independent recognition of sports activities from a single

wrist-worn accelerometer: A template-matching-based approach', *IEEE Transactions on Biomedical Engineering*, 63(4), pp. 788–796. doi: 10.1109/TBME.2015.2471094.

Marple, S. L. J. (1987) *Digital spectral analysis with applications*, *Englewood Cliffs*. New Jersey: Prentice-Hall, Inc. Available at: http://adsabs.harvard.edu/abs/1987ph...book.....M (Accessed: 8 August 2018).

Martinez, D., Matveev, V. and Nadim, F. (2016) 'Short-Term synaptic plasticity in central pattern generators', *Frontiers in Neural Circuits*. Berlin, 10, pp. 1–11. doi: doi.org/10.3389/fncir.2016.00004.

Marvasti, F. *et al.* (2012) 'A unified approach to sparse signal processing', *EURASIP Journal on Advances in Signal Processing*. Springer International Publishing, 44, pp. 1–45. doi: 10.1186/1687-6180-2012-44.

MathWorks (2016) *Signal Processing Toolbox™: User's Guide*. The MathWorks, Inc.

MathWorks (2018) 'Statistics and Machine Learning Toolbox™ User's Guide'. The MathWorks, Inc. Available at: www.mathworks.com (Accessed: 8 November 2018).

Maynard, D. M. (1955) 'Activity in a crustacean ganglion. II Pattern and interaction in burst formation', *The Biological Bulletin*, 109(3), pp. 420–436. doi: 10.2307/1539174.

Maynard, D. M. and Dando, M. R. (1974) 'The Structure of the Stomatogastric Neuromuscular System in Callinectes sapidus, Homarus americanus and Panulirus argus (Decapoda Crustacea)', *Philosophical Transactions of the Royal Society B: Biological Sciences*, 268(892), pp. 161–220. doi: 10.1098/rstb.1974.0024.

McClellan, J. H., Schafer, R. W. and Yoder, M. A. (2016) *DSP First*. second edi. Pearson.

McGaw, I. J. and Curtis, D. L. (2013a) 'A review of gastric processing in decapod crustaceans', *Journal of Comparative Physiology B*, 183, pp. 443–465. doi: 10.1007/s00360-012-0730-3.

McGaw, I. J. and Curtis, D. L. (2013b) 'Effect of meal size and body size on specific dynamic action and gastric processing in decapod crustaceans', *Journal of Comparative Physiology A*. Elsevier Inc., 166, pp. 414–425. doi: 10.1007/s00360-012-0730-3.

Miller, J. P. (1987) 'Pyloric Mechanisms', in Selverston, A. I. and Moulins, M. (eds) *The*

Crustacean Stomatogastric System: A Model for the Study of Central Nervous System. first edit. Munich: Springer-Verlag Berlin Heidelberg, pp. 1–2.

Minassian, K. *et al.* (2017) 'The human central pattern generator for locomotion: Does it exist and contribute to walking?', *The Neuroscientist*, 23(6), pp. 649–663. doi: 10.1177/1073858417699790.

Misiti, M. *et al.* (2018) *Wavelet Toolbox ™: User ' s Guide*. The MathWorks, Inc. Available at: http://www.mathworks.com/help/pdf_doc/wavelet/wavelet_ug.pdf.

Mizrahi, A. *et al.* (2001) 'Long-term maintenance of channel distribution in a central pattern generator neuron by neuromodulatory inputs revealed by decentralization in organ culture', *The Journal of neuroscience*, 21(18), pp. 7331–7339. doi: 21/18/7331 [pii].

Mohajerani, M. H. *et al.* (2010) 'Mirrored bilateral slow-wave cortical activity within local circuits revealed by fast bihemispheric voltage-sensitive dye imaging in anesthetized and awake mice', *Journal of Neuroscience*, 30(10), pp. 3745–3751. doi: 10.1523/JNEUROSCI.6437-09.2010.

Morlet, J., Arens, G., Fourgeau, E. and Giard, D. (1982) 'Wave propagation and sampling theory—Part II: Sampling theory and complex waves', *Geophysics*. Society of Exploration Geophysicists, 47(2), pp. 222–236. doi: 10.1190/1.1441329.

Morlet, J., Arens, G., Fourgeau, E. and Glard, D. (1982) 'Wave propagation and sampling theory - Part I: Complex signal and scattering in multilayered media', *Geophysics*. Society of Exploration Geophysicists, 47(2), pp. 203–221. doi: 10.1190/1.1441328.

Murillo-Escobar, M. A. *et al.* (2015) 'A robust embedded biometric authentication system based on fingerprint and chaotic encryption', *Expert Systems with Applications*. Pergamon, 42(21), pp. 8198–8211. doi: 10.1016/J.ESWA.2015.06.035.

Nagy, F. and Dickinson, P. S. (1983) 'Control of a central pattern generator by an identified modulatory interneurone in crustacea. I. Modulation of the pyloric motor output', *Journal of Experimental Biology*, 105, pp. 33–58.

Del Negro, C. A., Funk, G. D. and Feldman, J. L. (2018) 'Breathing matters', *Nature Reviews Neuroscience*. Nature Publishing Group, 19, pp. 351–367. doi: 10.1038/s41583-018-0003-6.

Neurotech (2018) *The Market for Neurotechnology: 2018-2022. A Market Research Report from Neurotech Reports*. Available at: http://www.neurotechreports.com/pages/execsum.html (Accessed: 25 May 2018).

Nogueira, J. and Caputi, A. A. (2013) 'From the intrinsic properties to the functional role of a neuron phenotype: an example from electric fish during signal trade-off', *Journal of Experimental Biology*, 216(13), pp. 2380–2392. doi: 10.1242/jeb.082651.

Norris, B. J., Coleman, M. J. and Nusbaum, M. P. (1996) 'Pyloric motor pattern modification by a newly identified projection neuron in the crab stomatogastric nervous system', *Journal of Neurophysiology*, 75(1), pp. 97–108. Available at: http://jn.physiology.org/content/75/1/97 (Accessed: 27 July 2015).

Norton, M. P. and Karczub, D. G. (2007) *Fundamentals of Noise and Vibration Analysis for Engineers*. 2nd editio, *Cambridge University Press*. 2nd editio. doi: 10.3397/1.2721371.

Nusbaum, M. P. and Beenhakker, M. P. (2002) 'A small-systems approach to motor pattern generation', *Nature*, 417, pp. 343–350. doi: 10.1038/417343a.

Nusbaum, M. P. and Marder, E. (1988) 'A neuronal role for a crustacean red pigment concentrating hormone-like peptide: Neuromodulation of the pyloric rhythm in the crab, Cancer borealis', *Journal of Experimental Biology*, 135, pp. 165–181.

Nuttall, A. H. and Carter, G. C. (1995) *Power spectra estimation*, *National Semiconductor Corporation*. doi: 10.1109/TASSP.1980.1163412.

Nyquist, H. (1928) 'Certain topics in telegraph transmission theory', *Transactions of the American Institute of Electrical Engineers*, 47, pp. 617–644. doi: 10.1109/T-AIEE.1928.5055024.

O'Leary, T. and Marder, E. (2014) 'Temperature-robust neural activity using feedback control of ion channel expression', *BMC Neuroscience*, 15(Suppl 1), p. 103. doi: 10.1186/1471-2202-15-S1-P103.

O'Leary, T. and Marder, E. (2016) 'Temperature-robust neural function from activity-dependent Ion channel regulation', *Current Biology*. Elsevier Ltd., 26, pp. 2935–2941. doi: 10.1016/j.cub.2016.08.061.

Obaid, A. L. *et al.* (2004) 'Novel naphthylstyryl-pyridinium potentiometric dyes offer advantages for neural network analysis', *Journal of Neuroscience Methods*, 134, pp. 179–190. doi: 10.1016/j.jneumeth.2003.11.011.

Ocean Biogeographic Information System (2018) *Cancer pagurus Linnaeus, 1758*, *Ocean Biogeographic Information System*. Available at: http://www.iobis.org/explore/#/taxon/416118 (Accessed: 25 May 2018).

Oesterle, A. (2015) *Pipette Cookbook 2015 - P-97 & P-1000 Micropipette Pullers*. Novato, CA: Sutter Instrument Company. doi: 10.1017/CBO9781107415324.004.

Olhede, S. C. and Walden, A. T. (2002) 'Generalized Morse wavelets', *IEEE Transactions on Signal Processing*, 50(11), pp. 2661–2670. doi: 10.1109/TSP.2002.804066.

Omidvarnia, A. *et al.* (2017) 'Dynamic coupling between fMRI local connectivity and interictal EEG in focal epilepsy: A wavelet analysis approach', *Human Brain Mapping*, 38(11), pp. 5356–5374. doi: 10.1002/hbm.23723.

Onat, S., König, P. and Jancke, D. (2011) 'Natural scene evoked population dynamics across cat primary visual cortex captured with voltage-sensitive dye imaging', *Cerebral Cortex*, 21(11), pp. 2542–2554. doi: 10.1093/cercor/bhr038.

Osmanski, M. S., Song, X. and Wang, X. (2013) 'The role of harmonic resolvability in pitch perception in a vocal nonhuman primate, the common marmoset (Callithrix jacchus)', *The Journal of Neuroscience*. Society for Neuroscience, 33(21), pp. 9161–9168. doi: 10.1523/JNEUROSCI.0066-13.2013.

Overland, J. E. *et al.* (1982) 'A Significance test for principal components applied to a cyclone climatology', *Monthly Weather Review*, 110(1), pp. 1–4. doi: 10.1175/1520-0493(1982)110<0001:ASTFPC>2.0.CO;2.

Pearson, K. (1901) 'On lines and planes of closest fit to systems of points in space', *The London, Edinburgh, and Dublin Philosophical Magazine and Journal of Science*, 2(11), pp. 559–572. doi: 10.1080/14786440109462720.

Pereira, W. C. *et al.* (2004) 'Singular spectrum analysis applied to backscattered ultrasound

signals from in vitro human cancellous bone specimens', *IEEE Transactions on Ultrasonics, Ferroelectrics and Frequency Control*, 51(3), pp. 302–312. doi: 10.1109/TUFFC.2004.1320786.

Peterka, D. S., Takahashi, H. and Yuste, R. (2011) 'Imaging voltage in neurons', *Neuron*. Elsevier Inc., 69, pp. 9–21. doi: 10.1016/j.neuron.2010.12.010.

Petersen, C. C. H., Grinvald, A. and Sakmann, B. (2003) 'Spatiotemporal dynamics of sensory responses in layer 2/3 of rat barrel cortex measured in vivo by voltage-sensitive dye imaging combined with whole-cell voltage recordings and neuron reconstructions', *The Journal of neuroscience : the official journal of the Society for Neuroscience*, 23(3), pp. 1298–1309. doi: 23/4/1298 [pii].

Pisarenko, V. F. (1973) 'The retrieval of harmonics from a covariance function', *Geophysical Journal International*. Oxford University Press, 33(3), pp. 347–366. doi: 10.1111/j.1365-246X.1973.tb03424.x.

Preuss, S. and Stein, W. (2013) 'Comparison of two voltage-sensitive dyes and their suitability for long-term imaging of neuronal activity', *PLoS ONE*, 8(10), pp. 1–13. doi: 10.1371/journal.pone.0075678.

Procyk, E. and Goldman-Rakic, P. S. (2006) 'Modulation of Dorsolateral Prefrontal Delay Activity during Self-Organized Behavior', *The Journal of Neuroscience*, 26(44), pp. 11313–11323. doi: 10.1523/JNEUROSCI.2157-06.2006.

Rabbah, P. and Nadim, F. (2005) 'Synaptic dynamics do not determine proper phase of activity in a Central Pattern Generator', *The Journal of Neuroscience*, 25(49), pp. 11269–11278. doi: 10.1523/JNEUROSCI.3284-05.2005.

Ramirez, J.-M., Tryba, A. K. and Peña, F. (2004) 'Pacemaker neurons and neuronal networks: An integrative view', *Current Opinion in Neurobiology*, 14, pp. 665–674. doi: 10.1016/j.conb.2004.10.011.

Rezer, E. and Moulins, M. (1983) 'Expression of the crustacean pyloric pattern generator in the intact animal', *Journal of Comparative Physiology*. Springer-Verlag, 153(1), pp. 17–28. doi: 10.1007/BF00610338.

Rocchi, L. *et al.* (2006) 'Identification of distinct characteristics of postural sway in Parkinson's disease: A feature selection procedure based on principal component analysis', *Neuroscience Letters*. Elsevier, 394(2), pp. 140–145. doi: 10.1016/J.NEULET.2005.10.020.

Rode, S. V and Ladhake, S. A. (2010) 'An adaptive filter for harmonic elimination', *IJCSNS International Journal of Computer Science and Network Security*, 10(10), pp. 154–157.

Sabnis, R. W. (2010) *Handbook of Biological Dyes and Stains: Synthesis and Industrial Applications*, *Handbook of Biological Dyes and Stains: Synthesisand Industrial Applications*. New Jersey: John Wiley & Sons, Inc. doi: 10.1002/9780470586242.

dos Santos, F. *et al.* (2017) 'A robust data-driven approach to the decoding of pyloric neuron activity', in *2017 IEEE Workshop on Signal Processing Systems, SiPS*. IEEE, pp. 1–6. doi: 10.1109/SiPS.2017.8110017.

dos Santos, F., Andras, P. and Lam, K. (2017a) 'A Multiresolution Approach to the Extraction of the Pyloric Rhythm', in *International Conference on Telecommunications and Signal Processing (TSP)*.

dos Santos, F., Andras, P. and Lam, K. (2017b) 'Towards an Accurate Identification of Pyloric Neuron Activity with VSDi', in *International Conference on Artificial Neural Networks (ICANN)*.

dos Santos, F. and Lam, KP. (2019) 'A practical approach to identify pyloric neurons with VSDi', submitted to *Journal of Computational Neurosciences*.

dos Santos, F., Lam, K. and Andras, P. (2017a) 'Neuron classification in the Stomatogastric ganglion using voltage-sensitive dye imaging and signal processing tools', in *26th Anual Computational Neuroscience Meeting (CNS 2017): Part2*. BMC Neuroscience, p. 2017. doi: 10.1186/s12868-017-0371-2.

dos Santos, F., Lam, K. and Andras, P. (2017b) 'Pyloric rhythm extraction using signal processing tools. Program No. 346.01', in *2017 Neuroscience Meeting Planner*. Washington, DC: Society for Neuroscience.

Sayood, K. (2012) *Introduction to Data Compression*. fourth edi, *Chemistry & biodiversity*. fourth edi. Edited by A. Dierna. Morgan Kaufmann, Elsevier. doi: 10.1109/MM.1996.526937.

Schaffer, P. *et al.* (1994) 'Di-4-ANEPPS causes photodynamic damage to isolated cardiomyocytes', *Pflügers Archiv European Journal of Physiology*, 426, pp. 548–551. doi: 10.1007/BF00378533.

Scheler, G. and Fellous, J. M. (2001) 'Dopamine modulation of prefrontal delay activity - Reverberatory activity and sharpness of tuning curves', *Neurocomputing*, 38–40, pp. 1549–1556. doi: 10.1016/S0925-2312(01)00559-8.

Schmidt, R. (1986) 'Multiple emitter location and signal parameter estimation', *IEEE Transactions on Antennas and Propagation*, 34(3), pp. 276–280. doi: 10.1109/TAP.1986.1143830.

Scientific, B. (2018) *Boston Scientific 2017 Annual Report*. Available at: http://thoughtleadership.aonbenfield.com/Documents/20180124-ab-if-annual-report-weather-climate-2017.pdf.

Seitola, T., Silén, J. and Järvinen, H. (2015) 'Randomised multichannel singular spectrum analysis of the 20th century climate data', *Tellus A: Dynamic Meteorology and Oceanography*, 67(1), p. 28876. doi: 10.3402/tellusa.v67.28876.

Selverston, A. *et al.* (1998) 'Basic principles for generating motor output in the Stomatogastric Ganglion', *Annals of the New York Academy of Sciences*, 860, pp. 35–50. doi: 10.1111/j.1749-6632.1998.tb09037.x.

Selverston, A. (2018) 'Rhythms and oscillations', in Prescott, T. J., Lepora, N., and Verschure, P. F. (eds) *Living machines: A handbook of research in biomimetics and biohybrid systems*. Oxford: Oxford University Press. Available at: https://books.google.co.uk/books?hl=en&lr=&id=xU5WDwAAQBAJ&oi=fnd&pg=PT297&dq=Understanding+rhythmic+motor+patterns+neurosciences&ots=r8v89VpEhC&sig=ClU8IT4koYI2dgFqsVbvVDxyAzc#v=onepage&q&f=false (Accessed: 25 May 2018).

Selverston, A. I. *et al.* (1976) 'The stomatogastric nervous system: Structure and function of a small neural network', *Progress in Neurobiology*, 7, pp. 215–289. doi: 10.1016/0301-0082(76)90008-3.

Selverston, A. I. (2005) 'A neural infrastructure for rhythmic motor patterns', *Cellular and Molecular Neurobiology*, 25(2), pp. 223–244. doi: 10.1007/s10571-005-3154-8.

Selverston, A. I. (2010) 'Invertebrate central pattern generator circuits', *Philosophical Transactions of the Royal Society B: Biological Sciences*, 365, pp. 2329–2345. doi: 10.1098/rstb.2009.0270.

Selverston, A. I. and Moulins, M. (1987) *The crustacean stomatogastric system - A model for the study of central nervous systems*. Berlin: Spinger - Verlag.

Selverston, A. I. and Rabinovich, M. I. (2009) 'Stomatogastric Ganglion Models', in Squire, L. R. (ed.) *Encyclopedia of Neuroscience*. La Jolla: Elsevier, pp. 425–435.

Shaharudin, S. M., Ahmad, N. and Yusof, F. (2015) 'Effect of window length with singular spectrum analysis in extracting the trend signal on rainfall data', in *AIP Conference Proceedings*. American Institute of Physics, pp. 321–326. doi: 10.1063/1.4907462.

Shlens, J. (2014) 'A Tutorial on Principal Component Analysis', *eprint arXiv:1404.1100*. doi: 10.1.1.115.3503.

Shuranova, Z. P. *et al.* (2006) 'Evidence for an autonomic nervous system in decapod crustacean', *International Journal of Zoological Research*, 3(2), pp. 242–283.

Sifuzzaman, M., Islam, M. R. and Ali, M. Z. (2009) 'Application of wavelet transform and its advantages compared to Fourier transform', *Journal of Physical Sciences*, 13, pp. 121–134. doi: 10.5194/hess-15-1835-2011.

Sirbu, D. *et al.* (2017) 'Locally Excited State–Charge Transfer State Coupled Dyes as Optically Responsive Neuron Firing Probes', *Chemistry - A European Journal*, 23, pp. 14639–14649. doi: 10.1002/chem.201703366.

Slovin, H. (2002) 'Long-term voltage-sensitive dye imaging reveals cortical dynamics in behaving monkeys', *Journal of Neurophysiology*, 88(6), pp. 3421–3438. doi: 10.1152/jn.00194.2002.

Smarandache, C. R. and Stein, W. (2007) 'Sensory-induced modification of two motor patterns in the crab, Cancer pagurus', *Journal of Experimental Biology*, 210(16), pp. 2912–2922. doi:

10.1242/jeb.006874.

Soofi, W. *et al.* (2014) 'Phase maintenance in a rhythmic motor pattern during temperature changes in vivo', *Journal of Neurophysiology*, 111, pp. 2603–2613. doi: 10.1152/jn.00906.2013.

Städele, C., Andras, P. and Stein, W. (2012) 'Simultaneous measurement of membrane potential changes in multiple pattern generating neurons using voltage sensitive dye imaging', *Journal of Neuroscience Methods*, 203, pp. 78–88. doi: 10.1016/j.jneumeth.2011.09.015.

Stein, J. (2000) *Digital Signal Processing - A Computer Science Perspective*, *Digital Signal Processing*. John Wiley & Sons, Inc. doi: 10.1002/047120059X.ch14.

Stein, W. *et al.* (2006) 'Functional consequences of activity-dependent synaptic enhancement at a crustacean neuromuscular junction', *The Journal of Experimental Biology*, 209, pp. 1285–1300. doi: 10.1242/jeb.02133.

Stein, W. (2009) 'Modulation of stomatogastric rhythms', *Journal of Comparative Physiology A*, 195, pp. 989–1009. doi: 10.1007/s00359-009-0483-y.

Stein, W. (2014) 'An in vivo assay for simultaneous monitoring of neuronal activity and behavioral output in the Stomatogastric Nervous System of decapod crustaceans', *Illinois State University - Biological Sciences*, pp. 1–9. Available at: http://ir.library.illinoisstate.edu/cgi/viewcontent.cgi?article=1027&context=fpbiosci (Accessed: 6 July 2015).

Stein, W. and Andras, P. (2010) 'Light-induced effects of a fluorescent voltage-sensitive dye on neuronal activity in the crab Stomatogastric Ganglion', *Journal of Neuroscience Methods*. Elsevier B.V., 188, pp. 290–294. doi: 10.1016/j.jneumeth.2010.03.003.

Stein, W., Eberle, C. C. and Hedrich, U. B. (2005) 'Motor pattern selection by nitric oxide in the stomatogastric nervous system of the crab', *European Journal of Neuroscience*, 21, pp. 2767–2781. doi: 10.1111/j.1460-9568.2005.04117.x.

Stein, W., Städele, C. and Andras, P. (2011) 'Single-sweep voltage-sensitive dye imaging of interacting identified neurons', *Journal of Neuroscience Methods*. Elsevier B.V., 194, pp. 224–234. doi: 10.1016/j.jneumeth.2010.10.007.

Steyn, J. S. and Andras, P. (2016) 'Analysis of the dynamics of temporal relationships of neural activities using optical imaging data', *Journal of Computational Neuroscience*. Journal of Computational Neuroscience, pp. 1–15. doi: 10.1007/s10827-016-0630-8.

Stoica, P. and Moses, R. (2005) *Spectral Analysis of Signals*. New Jersey: Prentice-Hall Inc. doi: 10.1002/9780470823767.ch2.

Stone, J. V (2004) *Independent Component Analysis: A Tutorial Introduction*. MIT Press. doi: 10.1007/978-3-642-81500-3_1.

Swaroop, P. and Sharma, N. (2016) 'An overview of various template matching methodologies in image processing', *International Journal of Computer Applications*, 153(10), pp. 975–8887.

Takekawa, T., Isomura, Y. and Fukai, T. (2012) 'Spike sorting of heterogeneous neuron types by multimodality-weighted PCA and explicit robust variational Bayes', *Frontiers in Neuroinformatics*, 6(March), pp. 1–13. doi: 10.3389/fninf.2012.00005.

Tang, L. S. *et al.* (2010) 'Precise temperature compensation of phase in a rhythmic motor pattern', *PLoS Biology*, 8(8), pp. 1–13. doi: 10.1371/journal.pbio.1000469.

Tang, L. S. *et al.* (2012) 'Robustness of a rhythmic circuit to short- and long-lerm temperature changes', *The Journal of Neuroscience*, 32(29), pp. 10075–10085. doi: 10.1523/JNEUROSCI.1443-12.2012.

Tasaki, I. *et al.* (1968) 'Changes in Fluorescence , Turbidity , and Birefringence Associated with Nerve', *National Academy of Sciences*, 61(3), pp. 883–888.

ThermoFisher (2018) *Fast-Response Probes—Section 22.2*, *ThermoFisher Scientific*. Available at: https://www.thermofisher.com/uk/en/home/references/molecular-probes-the-handbook/probes-for-membrane-potential/fast-response-probes.html (Accessed: 25 May 2018).

Thoby-Brisson, M. and Simmers, J. (1998) 'Neuromodulatory inputs maintain expression of a lobster motor pattern-generating network in a modulation-dependent state: evidence from long-term decentralization in vitro', *The Journal of Neuroscience*, 18(6), pp. 2212–2225. Available at: http://www.ncbi.nlm.nih.gov/pubmed/9482805.

Thuma, J. B. *et al.* (2003) 'Lobster (Panulirus interruptus) pyloric muscles express the motor neural networks, only one of which innervates the muscles', *The Journal of Neuroscience*. Society for Neuroscience, 23(26), pp. 8911–8920. Available at: http://www.ncbi.nlm.nih.gov/pubmed/9547250 (Accessed: 11 February 2018).

Tranquart, F. *et al.* (1999) 'Clinical use of ultrasound tissue harmonic imaging', *Ultrasound in Medicine & Biology*. Elsevier, 25(6), pp. 889–894. doi: 10.1016/S0301-5629(99)00060-5.

Tsemperouli, M. and Sugihara, K. (2018) 'Characterization of di-4-ANEPPS with nano-black lipid membranes', *Nanoscale*. Royal Society of Chemistry, 10, pp. 1090–1098. doi: 10.1039/C7NR05863B.

Tsytsarev, V. *et al.* (2014) 'Recent progress in voltage-sensitive dye imaging for neuroscience', *Journal of Nanoscience and Nanotechnology*, 14(7), pp. 4733–4744. doi: 10.1166/jnn.2014.9531.

Tufts, D. W. and Kumaresan, R. (1982) 'Singular value decomposition and improved frequency estimation using linear prediction', *IEEE Transactions on Acoustics, Speech, and Signal Processing*, 30(4), pp. 671–675. doi: 10.1109/TASSP.1982.1163927.

Wang, R. *et al.* (2015) 'Selection of window length for singular spectrum analysis', *Journal of the Franklin Institute*. Elsevier, 352, pp. 1541–1560. doi: 10.1016/j.jfranklin.2015.01.011.

Watling, L. and Thiel, M. (2012) *Functional Morphology and Diversity (The Natural History of Crustacea)*. Volume 1. New York: Oxford University Press. Available at: https://books.google.com/books?hl=en&lr=&id=HJ5pAgAAQBAJ&pgis=1 (Accessed: 17 July 2015).

Wax, M. and Kailath, T. (1985) 'Detection of signals by information theoretic criteria', *IEEE Transactions on Acoustics, Speech, and Signal Processing*, 33(2), pp. 387–392. doi: 10.1109/TASSP.1985.1164557.

Weimann, J. M. and Marder, E. (1994) 'Switching neurons are integral members of multiple oscillatory networks', *Current Biology*, 4(10), pp. 896–902. doi: 10.1016/S0960-9822(00)00199-8.

Weimann, J. M., Meyrand, P. and Marder, E. (1991) 'Neurons that form multiple pattern

generators: identification and multiple activity patterns of gastric/pyloric neurons in the crab stomatogastric system', *Journal of Neurophysiology*, 65(1), pp. 111–122. Available at: http://jn.physiology.org/content/65/1/111.short (Accessed: 25 July 2015).

Weisstein, E. W. (2018) *Eigen Decomposition*. MathWorld - A Wolfram Web Resource. Available at: http://mathworld.wolfram.com/EigenDecomposition.html (Accessed: 18 July 2018).

Welch, P. (1967) 'The use of fast Fourier transform for the estimation of power spectra: A method based on time averaging over short, modified periodograms', *IEEE Transactions on Audio and Electroacoustics*, 15(2), pp. 70–73. doi: 10.1109/TAU.1967.1161901.

Wiersma, C. A. (1953) 'Neural transmission in invertebrates', *Physiological Reviews*, 33(3), pp. 326–355. doi: 10.1152/physrev.1953.33.3.326.

Wiese, K. *et al.* (1990) *Frontiers in Crustacean Neurobiology - The Cooperation of Several Oscillators in the Stomatogastric System of the Crab Cancer Pagurus*. Edited by K. Wiese et al. Basel: Birkhäuser Basel. doi: 10.1007/978-3-0348-5689-8.

Williams, A. H. *et al.* (2013) 'Animal-to-animal variability in the phasing of the crustacean cardiac motor pattern: an experimental and computational analysis', *Journal of Neurophysiology*, 109, pp. 2451–65. doi: 10.1152/jn.01010.2012.

Williamson, R. and Chrachri, A. (2004) 'Cephalopod Neural Networks', *NeuroSignals*, 13, pp. 87–98. doi: 10.1159/000076160.

Zecevic, D. *et al.* (1989) 'Hundreds of neurons in the Aplysia abdominal ganglion are active during the gill-withdrawal reflex', *The Journal of Neuroscience*, 9(10), pp. 3681–3689. Available at: http://www.ncbi.nlm.nih.gov/pubmed/2795148.

Zerilli, F. J. (1970) 'Gravitational field of a particle falling in a Schwarzschild geometry analyzed in tensor harmonics', *Physical Review D*. American Physical Society, 2, pp. 2141–2160. doi: 10.1103/PhysRevD.2.2141.

Zhu, H. *et al.* (2017) 'Single-neuron identification of chemical constituents, physiological changes, and metabolism using mass spectrometry', *PNAS*, 14(10), pp. 2586–2591. doi:

10.1073/pnas.1615557114.

Zhu, L., Selverston, A. I. and Ayers, J. (2016) 'Role of Ih in differentiating the dynamics of the gastric and pyloric neurons in the stomatogastric ganglion of the lobster, Homarus americanus.', *Journal of Neurophysiology*. American Physiological Society, 115(5), pp. 2434–2445. doi: 10.1152/jn.00737.2015.

Appendices

Appendix 1

Standard operating procedure

Process: Chilling Crabs	
Dept: Central Animal Facility	**Location:** Room 8/9
Original Issue Date: 10.3.15	**Revision Date:** 10.03.16

Background Information:

Before beginning a crab dissection the crab must be sufficiently chilled in order to render it insensible.

Procedural methods:

- Fill a bucket with ice from the ice machine in the Haldane Lab (Huxley Building)
- Carefully remove the crab from the tank and place it in the ice bucket.
- Ensure the crab is sufficiently encapsulated by ice. (Note what time this took place)
- After 30 minutes check if the crab is insensible. The crab is assumed to be insensible if the abdomen or tail can be easily extended or manipulated and the outer mouthparts can be moved without resistance.
- Ensure there is no pincer reflex by putting pressure on the inner aspect of the claw and manually extend the mandible to assess for close reflex.
- If the crab shows resistance to manipulation or if reflexes persist, return it to the ice for a further 10 to 15 minutes and then recheck it.
- Once the crab is sufficiently chilled and is insensible the gross dissection can begin.

Appendix 2

Photographs and list of material used in the gross and fine dissection.

Figure 1 – The equipment used for gross dissection. From left to right: Kelly forceps, bone cutter, Blumenthal Rongeurs, spatula and dissection scissors.

Figure 2 – The equipment used for fine dissection. From left to right: Dumont tweezers #5, Dumont tweezers #55, Vannas scissors, straight, standard, and superfine Vannas scissors, straight, 3mm blades.